

Spatially Resolved Transport Studies and Microscopy of Ultrathin Metal-Oxide-Semiconductor Structures

Office of Naval Research, Contract NO. N00014-95-C-0087, Final Report

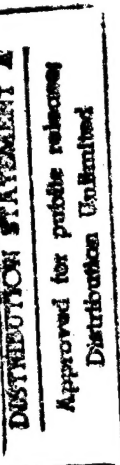
August 20, 1997

R. Ludeke, Principal Investigator

IBM T.J. Watson Research Center, P.O. Box 218 Yorktown Heights NY, 10598, USA

Abstract. The objective of the contract was the investigation of hot electron transport on a microscopic scale in metal-oxide-semiconductor (MOS) structures in order to assess intrinsic transport properties in SiO₂ and defect generation processes that lead to oxide failure. The technique used to achieve microscopic resolution was Ballistic Electron Emission Microscopy (BEEM), a variant of the Scanning Tunneling Microscope (STM). In BEEM, use is made of the nearly monochromatic and highly forward focused electron beam of the STM to inject hot electrons through the thin metal "gate" and into the conduction band of the SiO₂. The measured minimum electron energy required to achieve injection and subsequent detection in the Si defines the oxide barrier potential. A research highlight was the demonstration of image force effects in electron transport through MOS structures. The observation was made that the oxide barrier potential decreased with the application of an oxide field. This effect was attributed to screening by metal electrons and was described by classical image force lowering, an often-ignored concept by the MOS science and engineering community. The results led to a new "dynamic" value for the dielectric constant of SiO₂, which was confirmed by theoretical modeling of the MOS transport process. Monte Carlo simulations were made of the spreading of the beam as it traverses the oxide. The inclusion of image force effects was necessary for agreement with experiment.

The objectives of oxide degradation were realized through electron trapping studies and localized breakdown attempts. Two types of oxide traps were observed, pre-existing or process induced and hot-electron generated traps. The latter are generated by hot electrons with kinetic energy exceeding 2 eV and are associated with the breakage of



19971001
055

H-Si bonds in the oxide. Through field assisted barrier changes it was possible to determine the in-depth or profile of the trap distribution in the oxide. For a 7 nm oxide, their densities were in the low-to-mid $10^{13}/\text{cm}^2$ range, with the pre-existing traps located near the metal gate and the generated traps distributed over the half space of the oxide adjacent to the Si. Attempts to break down the oxide with hot electrons exceeding 15 eV proved very difficult. Breakdowns following local stressing with BEEM were seldom observed, and only when stressing conditions far exceeded those reported on macroscopic samples. It was concluded that even these cases were still dominated by low-density, randomly distributed defects in the oxide.

I. Research Proposal Summary and Objectives

The proposal was submitted to the Office of Naval Research in March of 1995. It was granted to commence on October 10, 1995 and terminate on May 27, 1997.

The objective of the proposal and its planned implementation were clearly stated in the proposal summary, which is reproduced below.

"This proposal seeks financial support for a research initiative in the spatially resolved transport properties of hot electrons injected into metal-oxide-semiconductor (MOS) structures. The financial support, in the form of a two-year, cost-share contract between the International Business Machines Corp. and the Office of Naval Research, is to cover the costs of a post-doctoral scientist over the period of the contract. The proposal is rooted in a need for understanding on a microscopic level the electron transport properties through ultrathin ($<100 \text{ \AA}$) oxides that are being considered for future generations of integrated circuits based on MOS technology. For this reason the proposal stresses the use of device-quality oxides thermally grown on Si at an IBM wafer processing facility. The technical program proposes that a scanning tunnel microscope (STM) be used to inject hot electrons into MOS structures. A special implementation of the STM, known as ballistic electron emission microscopy or BEEM, permits control of the kinetic energy of the injected electrons, which also exhibit quasi-monochromatic energy distributions. These properties of BEEM, combined with the inherent control over the electric field across the oxide, suggest a potentially unique tool to investigate transport properties through oxide layers, including the role of defects in the oxide, at spatial resolutions approaching atomic dimensions. The proposed work addresses three topics: 1) an investigation of the fundamental hot electron transport processes across MOS structures for electron injection with an STM tip, 2) the detection and imaging of individual electron trap states in the oxide, their generation characteristics through impact with energetic electrons, and the dynamics of electron trapping and detrapping, and 3) an evaluation of the BEEM technique as a new diagnostic tool to quantify process-dependent oxide properties and oxide quality."

The Research Objectives were stated as follows:

1) Intrinsic transport properties of SiO₂:

Investigations of the energy and field dependent processes underlying BEEM-mediated electron transport issues in MOS structures are proposed, with the purpose of enhancing the understanding of fundamental physical concepts from a new and often advantageous perspective.

2) Defect related phenomena in SiO₂:

Investigations of local distributions of charged defects are proposed. Defects inherent to the as-grown oxide and those induced through in-situ electrical stressing of the MOS structure will be studied, with the purpose of understanding the origin, densities and mode of generation of defects and traps in SiO₂.

3) SiO₂ process diagnostics

A study of process related defect generation will be undertaken with the purpose of determining the feasibility of using the technique as a viable tool to characterize oxides for technical purposes.

The objectives will be used as a guide to describe the progress achieved during the grant period.

Research Accomplishments during Grant Period

1) Intrinsic transport properties of SiO₂:

1a. Image Force Effects

(details in appendices 3 and 4)

As an electron passes from the metal gate of a Metal-Oxide-Semiconductor (MOS) structure into the oxide, its potential energy is modified by the charge imbalance it induces in the metal. This charge modification is positive (attractive), and represents a response by the metal to screen the electric field set up by the moving electron in the oxide. This screening is described well by the classical concept of an image charge placed in the metal at a distance equal to that of the electron on the oxide side of the interface. The effect of the attractive force is to lower the potential sensed by the electron. This so-called image force lowering was already observed in MOS structures over 30 years ago by internal photoemission spectroscopy.¹⁻³ Its presence, however, was generally ignored by almost all researchers in MOS transport studies. Consequently image force effects remains a controversial subject in oxide transport.

Since BEES measures directly the threshold energy between the Fermi level of the metal and the conduction band minimum of the SiO₂, it is thus an ideal tool to measure the Schottky effect, which is the combined effect of the image force of the electron in the vicinity of the metal-oxide interface and that of an applied oxide field V_{ox}. This effect was observed with BEES in one of the earlier studies supported by the ONR grant.⁴ Classical image force theory predicts that the lowering of the threshold δeV_0 is given by $[V_{ox}/4\pi\epsilon_0\epsilon_{ox}t_{ox}]^{1/2}$, where ϵ_0 and ϵ_{ox} are, respectively, the permittivity of vacuum and the effective dielectric constant of the oxide sensed by a moving charge. The latter has been assumed to be represented by the optic dielectric constant, given by $\epsilon_{op}=2.15$, that was measured using the indirect and model dependent internal photoemission method.² The value of ϵ_{ox} obtained with BEES is 2.74,⁵ and lies in-between the limits of $\epsilon_{op}=2.15$ and the static dielectric constant $\epsilon_s=3.9$. This conflicting result was the motivation for a theoretical investigation of the dynamic response of a dielectric to a moving charge in the vicinity of a metal interface, an issue of basic interest and practical

consequences. The BEES experiment was modeled within the framework of classical dielectric response theory, that included electron-phonon interactions.⁶ A value $\epsilon_{ox}=2.69$, close to the experimental value of 2.74 was calculated.⁵ It was concluded that the dynamic response is not determined by the transit time of the electron to reach the potential maximum, as previously suggested,⁷ but rather by the nearly field independent mean velocity of the electron between the metal interface and the potential maximum. Consequently phonon effects cannot be ignored and arguments for an optical dielectric value based solely on the short transit time to reach the potential maximum are too crude. The new value for ϵ_{ox} should have impact on transport modeling issues, for which the optic value was used up to the present.

The observed lowering of the BEEM threshold with increasing oxide field has been frequently criticized as due to tunneling. To dispel this possibility, WKB calculations of the tunneling probabilities were performed as a function of the oxide field. The results do not show the linear dependence of the threshold shifts on the square root of the oxide potential, from which it was concluded that direct tunneling effects are negligible in field assisted BEEM on MOS structures.

1b. Monte Carlo Simulations

(details in appendices 2 and 8)

Theoretical modeling of electron transport across MOS structures to simulate BEEM was accomplished by integrating the Boltzmann equation using Monte Carlo techniques that incorporate energy dependent effective masses and energy dependent electron-phonon scattering rates.⁸ In these studies the energy dependent transmission probability for an electron to traverse the SiO₂ layer and reach the Si was calculated and compared to BEEM-derived results. For agreement with experiment, the electrons' angle of injection in the Monte Carlo simulations needed to be distributed isotropically, that is, all angles were equally possible. This assumption appeared to be counter intuitive, as experimentally the electrons approached the interface at normal angles. The latter geometry requires an additional scattering channel in the oxide in order to make simulations and experiment agree. Such additional scattering channel was not envisioned until the importance of the image force induced band bending at the metal-oxide inter-

face was realized. An isotropic distribution did not arise from a lack of interfacial coherence, as previously speculated, but rather from additional electron-phonon scattering in the image force region of the oxide. In this region an electron injected with energy just sufficient to overcome the barrier will nevertheless experience large kinetic energies due to the rapidly downward-bending conduction band at the metal interface. Since the randomizing acoustic phonon scattering is strongly energy dependent, with a maximum scattering rate for electrons at kinetic energies near 2 eV,⁸ many electrons are scattered back into the metal, even though their energy relative to the barrier maximum is small. This added scattering channel strongly suppresses the transmission probabilities at low kinetic energies, a conclusion that is supported by the agreement between BEEM results and Monte Carlo simulations that included image force effects and injection normal to the interface.⁹ Our findings thus demonstrate the necessity of including image force effects in order to properly simulate electron transport across MOS structures.

With knowledge of the necessity for proper boundary conditions in Monte Carlo simulations, we proceeded to calculate the spread of the electron beam due to electron-phonon scattering as it reaches the oxide-silicon interface.¹⁰ The beam spread must be known to determine the lateral resolution of BEEM, as well as to assess the current density and injected charge density at the interface following electric stressing. The calculations were made for low energies typically encountered for threshold determinations and for energies typically used during electric stress measurements of oxide samples. For the low energies that correspond to tip biases in the 4-5 V range, the electrons traverse the oxide with little scattering (ballistic), so that even for a 7 nm oxides the BEEM spread, and hence resolution, is better than 1 nm. In contrast, for electrons with energies of 4 eV or larger (tip biases ~10 V), the spread for a 3.8 and a 7.6 nm oxide at the Si interface cover an area with diameters of ~6 and ~12 nm, respectively.¹⁰ These simulations demonstrate that threshold determinations, which are very sensitive to oxide charge, are achievable under optimal resolution conditions. As will be discussed in the next section, this attribute of BEEM will be used to estimate the local fluctuations in the density of trapped electrons in the oxide.

2) Defect related phenomena in SiO₂:

2a. Trap generation and trapped charge profiling (details in appendices 5,6 and 7)

Trap generation and measurements of the trapped charge density are routine procedures in oxide studies using standard capacitance-voltage and current-voltage methods. However, it has not been possible in the past to determine the in-depth distribution or charge density profile across the oxide. Using conventional techniques only the centroid of the charge distribution was obtained.¹¹ BEEM, however, measures directly the potential maximum of the trapped charge distribution. From the changes in the potential induced by varying the applied oxide bias we were able to determine the trapped charge distribution that modifies the oxide potential.^{12,13}

Capture of injected electrons at trap sites in the oxide was studied on a local scale as a function of both the energy of injected electrons and applied oxide bias. It was generally observed that the first measured BEEM spectrum on a virgin portion of the MOS surface exhibited the lowest threshold in an array of spectra taken over a 25×25 nm² area. This threshold, whose value is 4 eV, corresponds to the intrinsic barrier height between the Fermi level of the metal and the conduction band minimum of the SiO₂, and represents an essentially charge free region of the oxide. Once scanned, the thresholds in the scanned area increased, a clear indication that local electron trapping occurred as part of the measurement. The increases were observed at sampling locations as far as 5-10 nm away from the initial injection point, and are the consequence of trapped electrons scattered to distant sites as the beam spreads in its progress toward the Si substrate. This notion is supported by the Monte-Carlo calculations of the beam spread discussed in section 1.1b above. When the kinetic energy of the injected electrons in the oxide E_{kin} remained below 2 eV (this corresponds to a tip bias V_T<6 V and no applied oxide bias), the threshold shifts ceased after a few spectral scans, which indicates a saturation of the trap filling process. It was concluded that these trap states could not be generated by the injection process, and therefore their origin must have pre-existed the measurement. In contrast for hotter injected electrons, i.e. those with E_{kin}>2 eV, additional threshold shifts of several eV were observed. These shifts, which

also ceased to change after repeatedly scanning the sampling area, are attributed to the capture of additional electrons at newly created trap sites. The energy threshold of 2 eV required for their creation agrees with that associated with the breakage of Si-H bonds in the oxide,^{16,17} to which we tentatively assign the newly observed traps.

The distribution of the traps across the oxide has not been possible to obtain by conventional I-V or C-V techniques. With BEEM, however, it is possible to measure the potential maximum and its variation with applied oxide bias, from which the filled trap distribution can be obtained through modeling.¹² In the model the trapped charge is represented by a series of sheet charges parallel to the interfaces, whose influence on the potential must be considered through appropriate boundary conditions. The positions and strengths (charge densities) of the sheet charges are adjusted until the field dependence of the potential maximum arising from the combination of sheet charges, applied oxide bias and image force effects matches the field dependence of the observed threshold shifts. This modeling methodology revealed that for a 7 nm oxide the pre-existing defects were located within ~3 nm of the gate metal, and the generated defects were distributed predominantly within 4 nm of the oxide-Si interface. Their charge densities are in the range of $1-4 \times 10^{13}/\text{cm}^2$. An important conclusion was the realization that the distribution of the pre-existing defects was not affected by the generation of new defects. This observation is possible because the two types of traps are spatially separated, and indicates that the more energetic electrons do not create new defects in the vicinity of the metal gate.

2b. Oxide stressing and breakdown studies

(details in appendices 2 and 5)

The salient conclusion of our studies is that stressing an oxide layer locally by injecting hot electrons with an STM in a BEEM experiment seldom leads to a destructive breakdown of the oxide. In the few cases when a breakdown occurs, the net injected charge, commonly referred to as charge-to-breakdown or Q_{bd} , is orders of magnitude larger than the best values reported for macroscopic size MOS structures stressed through Fowler-Nordheim (F-N) injection.¹⁸ Most of the successful breakdown experiments were performed on 3.8 nm oxides. The electrical stressing experiments are per-

formed by placing the tip of the STM at a specific point on the surface, or by scanning a small area (typically $25 \times 25 \text{ nm}^2$) and interrupting the scans at points that are part of a pre-selected pattern. Once the tip is at the designated point, the tip bias V_T is set to a predetermined large value (in the range of 7-10 V) and the collector current is integrated to determine the charge injected locally into the oxide. The injection process is interrupted periodically to measure the threshold changes. These increase initially and reaches a plateau, a process that corresponds to a trap generation and filling process analogous to that discussed in section 2a. It was observed that if the stressing proceeds toward an eventual breakdown, the thresholds begin to decrease again, a process that is accompanied by an increase in the overall collector current. This second stage of stressing was referred to as the pre-breakdown stage.¹⁰ It was proposed that this stage consists of a gradual collapse of the oxide barrier. This process consists of the deterioration of the oxide that starts at the O-S interface and leads to the formation of regions of finite conductivity. Additional stressing quickly led to a threshold of only 1 eV, which was interpreted as due to a total collapse of the oxide barrier. This stage was termed the breakdown stage, with the net collector current integrated to a time just prior to the collapse defining Q_{bd} .

BEEM stressing results are compared to "best-of-breed" Q_{bd} 's obtained by F-N stressing in Fig. 1. The latter are depicted by open symbols and lines in Fig. 1.¹⁸ In order to compare the data, the energies of electrons in the BEEM Q_{bd} 's have to be converted to electric fields that in a F-N injection process would field-accelerate the electrons to energy values at the anode equivalent to those used in BEEM. This conversion assumes that the breakdown process depends predominantly on the energy of the electrons, and not on the field. The results of our breakdown studies are shown by the solid points on the right of Fig. 1. A stress experiment that led to no breakdown is shown by an open circle. In order to calculate the charge density, we used Monte-Carlo simulation to calculate the area (spread) of the electron beam at the O-S interface, as discussed in section 1b, above. It is obvious by looking at Fig. 1 that the BEEM initiated local breakdowns, when they occur, lie appreciably above an extrapolated curve of data obtained in a conventional, large area stressing experiment. The latter results were thought to be limited by "intrinsic" properties of the oxide.¹⁸ Our results clearly con-

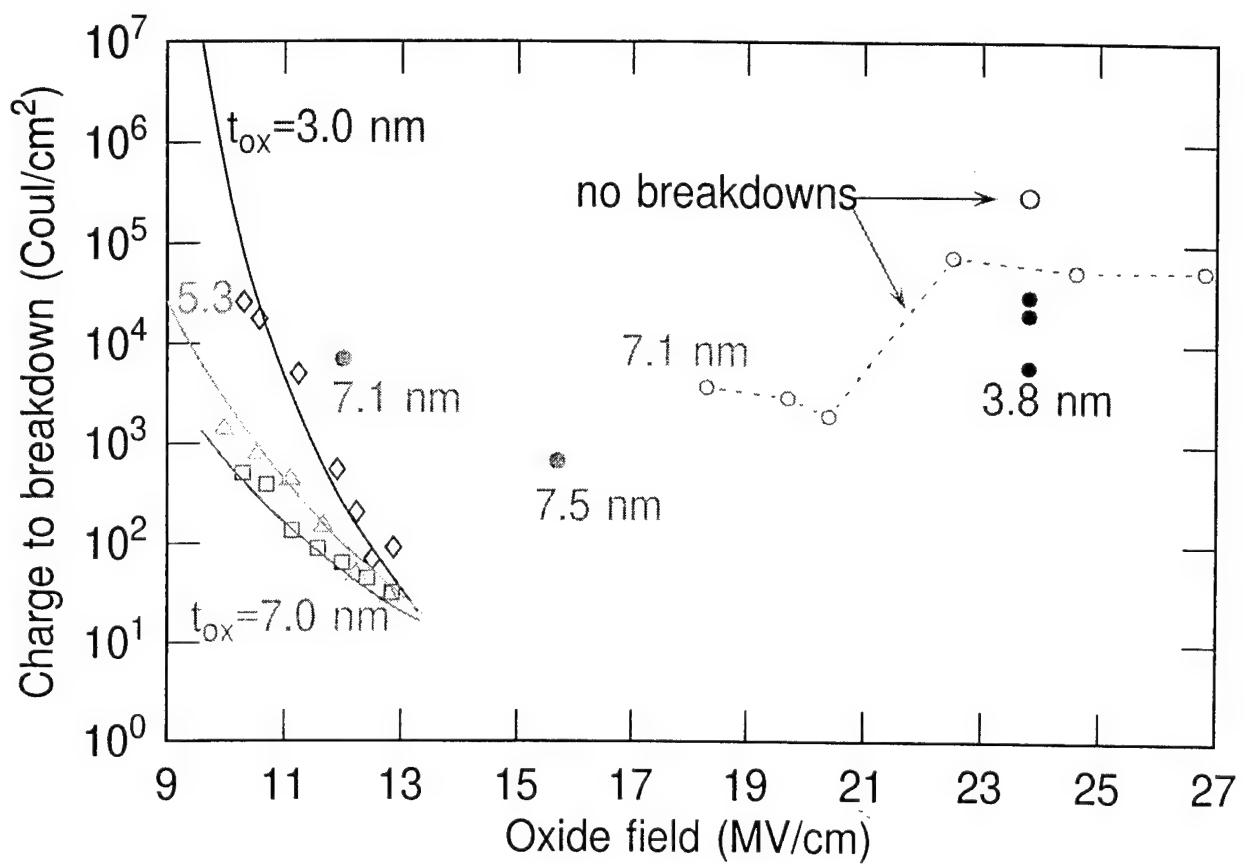


Fig. 1. Charge-to-breakdown comparisons between BEEM-stressed oxides and Fowler-Nordheim stressed MOS samples. The latter were obtained by Schuegraf and Hu, ref. 18, and are shown as solid curves through open symbols at the left. The filled circles represent BEEM breakdown results, whereas the open circles represent extreme BEEM stressing results without reaching breakdown. The electron energies used in BEEM were converted to an oxide field required to achieve equivalent energies at the cathode in a Fowler-Nordheim experiment.

tradict this view, indicating instead that an intrinsic limit has not yet been reached, and that even in our case breakdowns are still limited by randomly distributed defects/impurities of unknown origin.

In recent, yet to-be-published studies, we investigated the roles of both trap densities and electric fields on breakdown. The field dependent stressing was motivated by the difficulty of achieving breakdowns without the application of an oxide bias. Stressing in areas of known high densities of generated traps ($\sim 10^{13}/\text{cm}^2$) did not result in breakdowns. Similar results were obtained by extensive stressing with the combination of high oxide fields and energetic electrons at a point on the sample after tip drifts were nearly negligible. The injected charge densities as a function of the F-N equivalent oxide fields of this stressing sequence are shown by open circles in Fig. 1 for progressively higher stressing conditions at the same point. Because of some drift, the charge densities should not be added. We see no evidence that fields of up to 9 MV/cm influence breakdowns in our BEEM experiments. The failure to achieve breakdowns leads one to question much of the conventional wisdom of the roles of process induced and hydrogen-related defects in breakdown. Clearly the observed densities are insufficient to provide connectivity across the oxide, which, if necessary,¹⁹ suggests the presence of small, statistically distributed regions of very high trap densities. Alternatively, the observed defects may be necessary but not sufficient to cause breakdown, with as yet unidentified new defects activating the breakdown process.

3) SiO_2 process diagnostics

With the exception of the process induced trap formation attributed to metallization, which was discussed in Section 2 above, no additional studies in this topic were attempted.

References

1. C. A. Mead, E. H. Snow and B. E. Deal, *Appl. Phys. Lett.* **9**, 53 (1966).
2. R. J. Powell, *J. Appl. Phys.* **41**, 2424 (1970).
3. P. M. Solomon and D. J. DiMaria, *J. Appl. Phys.* **52**, 5867 (1981).
4. R. Ludeke, E. Cartier and H. J. Wen, *The Physics and Chemistry of SiO₂ and the Si-SiO₂ Interface -3*, H.Z. Massoud, E.H. Poindexter and C.R. Helms, Editors, Proc. Vol. 96-1, p. 580-591, *The Electro-Chemical Society*, Pennington, NJ, 1996. (Proceedings of the Third International Symposium on The Physics and Chemistry of SiO₂ and the Si-SiO₂ Interface, Los Angeles, CA May 6-10, 1996)
5. H. J. Wen, R. Ludeke, D. M. Newns and S. H. Lo, *J. Vac. Sci. Technol. A* **15**, 784 (1997).
6. H.J. Wen, D. M. Newns and R. Ludeke, submitted to *Phys. Rev. Lett.*
7. C. N. Berglund and R. J. Powell, *J. Appl. Phys.* **42**, 573 (1971).
8. R. Ludeke, A. Bauer and E. Cartier, *J. Vac. Sci. Technol. B* **13**, 784 (1995).
9. H.J. Wen, R. Ludeke and D. M. Newns, *Appl. Surface. Sci.* accepted.
10. R. Ludeke, H. J. Wen and E. Cartier, *J. Vac. Sci. Technol. B* **14**, 2855 (1996).
11. D. J. DiMaria, *J. Appl. Phys.* **47**, 4073 (1976).
12. H.J. Wen and R. Ludeke, *J. Vac. Sci. Technol. B* **15** in press.
13. R. Ludeke and H.J. Wen, submitted to *Appl. Phys. Lett.*

14. D. J. DiMaria and J. W. Stasiak, *J. Appl. Phys.* **65**, 2342 (1989).
15. D. J. DiMaria, E. Cartier and D. Arnold, *J. Appl. Phys.* **73**, 3367 (1993).
16. D. A. Buchanan, J. H. Stathis, E. Cartier and D. J. DiMaria, *Microelectronic Engineering*, **36**, 329 (1997).
17. D. J. DiMaria and E. Cartier, *J. Appl. Phys.* **78**, 3883 (1995).
18. K. F. Schuegraf, D. Park and C. Hu, *Proceedings of the IEEE International Electron Device Meeting*, 1994, p. 609.
19. J. H. Stathis, *Microelectronic Engineering* **36**, 325 (1997).

Publications based on grant-supported research

1. "Spatially and Energy Resolved Hot Electron Transport through Metal-Oxide-Silicon Structures", R. Ludeke, E. Cartier and H. J. Wen, The Physics and Chemistry of SiO_2 and the Si- SiO_2 Interface -3, H.Z. Massoud, E.H. Poindexter and C.R. Helms, Editors, Proc. Vol. 96-1, p. 580-591, The Electro-Chemical Society, Pennington, NJ, 1996. (Proceedings of the Third International Symposium on The Physics and Chemistry of SiO_2 and the Si- SiO_2 Interface, Los Angeles, CA May 6-10, 1996)
2. "Stressing and High Field Transport Studies on Device-grade SiO_2 by Ballistic Electron Emission Spectroscopy", R. Ludeke, H. J. Wen and E. Cartier, J. Vac. Sci. Technol. **B14**, 2855 (1996).
3. "Image Force Effects and the Dielectric Response of SiO_2 in Electron Transport across MOS Structures", H. J. Wen, R. Ludeke, D. M. Newns and S. H. Lo, J. Vac. Sci. Technol. **A 15**, 784 (1997).
4. "Dielectric Response in Electron Transport across Metal-Oxide-Semiconductor Structures", H.J. Wen, D. M. Newns and R. Ludeke, submitted to Phys. Rev. Lett.
5. "Gate Oxide Characterization with Ballistic Electron Emission Microscopy", R. Ludeke and H.J. Wen, Microelectronic Engineering, **36**, 255 (1997).
6. "Investigation of Existing Defects and Defect Generation in Device-grade SiO_2 by Ballistic Electron Emission Spectroscopy", H.J. Wen and R. Ludeke, J. Vac. Sci. Technol. **B 15** in press.
7. "Localized Electron Trapping and Trap Distributions in SiO_2 Gate Oxides", R. Ludeke and H.J. Wen, submitted to Appl. Phys. Lett.
8. "Atomic Scale Studies of Electron Transport through MOS Structures", H.J. Wen, R. Ludeke and D. M. Newns, 6th International Conference on the Formation of Semiconductor Interfaces (ICFSI), Cardiff, Wales, UK, June 26, 1997, Appl. Surface Science, accepted.

Conference talks based on grant-supported research

Invited Conference Talks

"Transport Issues of STM-Injected Hot Electrons in Metal-Oxide- Semiconductor Structures", R. Ludeke, E. Cartier and H.J. Wen, 26th IEEE Semiconductor Interface Specialist Conference, Charleston, SC, Dec.7-9, 1995.

"STM-Mediated Hot Electron Injection and Transport in MOS Structures", R. Ludeke, H.J. Wen and E. Cartier, 24th Annual Symposium on Applied Vacuum Science and Technology, Orlando, FL, March 11-14, 1996.

"Characterization of Hot Electron Transport and Breakdown in Ultrathin Gate Oxides using BEEM". R. Ludeke, H.J. Wen and E. Cartier, SRC Topical Research Conference on Ultrathin Gate Dielectrics, Raleigh, NC, March 21-22, 1996

"Spatially and Energy Resolved Hot Electron Transport through Metal-Oxide-Silicon Structures", R. Ludeke, H.J. Wen and E. Cartier, Third International Symposium on the Physics and Chemistry on SiO₂ and the Si-SiO₂ Interface, 189th Meeting of the Electrochemical Society, Los Angeles, CA, May 6-10, 1996.

"Spatially Resolved Vertical Transmission and Stressing Studies of Gate Oxides using BEEM", R. Ludeke, H. J. Wen, E. Cartier and D. M. Newns, 2nd International Symposium on Control of Semiconductor Interfaces, Karuizawa, Japan, Oct.31, 1996.

"The Elusive Flaw in the Oxide: a Microscopic Study of Transport in SiO₂", R. Ludeke, and H.J. Wen, AVS New England Chapter meeting, Burlington, MA, March 3, 1997

"Gate Oxide Characterization with Ballistic Electron Emission Microscopy", R. Ludeke, and H.J. Wen, INFOS (Insulating Films on Semiconductors) Conf. Stenungsund, Sweden, June 13, 1997.

"Atomic Scale Studies of Electron Transport through MOS Structures", H.J. Wen, R. Ludeke and D. M. Newns, 6th International Conference on the Formation of Semiconductor Interfaces (ICFSI), Cardiff, Wales, UK, June 26, 1997.

Contributed Conference Talks

"High Field Transport and Stressing Studies on Device-grade SiO₂ by Ballistic Electron Emission Spectroscopy", R. Ludeke, H. J. Wen and E. Cartier, Conf. on the Physics and Chemistry of Semiconductor Interfaces (PCSI 23), La Jolla, CA, Jan. 21-25, 1996.

"Image Force Effects and the Dielectric Response of SiO₂ in Electron Transport across MOS Structures, H.J. Wen R. Ludeke, D. M. Newns and S. H. Lo, National Symposium of the American Vavuum Society, Philadelphia, Oct. 14, 1996.

"Investigation of Existing Defects and Defect Generation in Device-grade SiO₂ by Ballistic Electron Emission Spectroscopy", H.J. Wen and R. Ludeke, Conf. on the Physics and Chemistry of Semiconductor Interfaces (PCSI 24), Research Triangle Park, NC, Jan. 12-15, 1997.

"Image Force Effects and the Dielectric Response of SiO₂ in MOS Structures", H.J. Wen, R. Ludeke, D. M. Newns and S.-H. Lo, INFOS (Insulating Films on Semiconductors) Conf. Stenungsund, Sweden. June 11, 1997.

"Hot Electron Initiated Local Defect Generation and Breakdown in Gate Oxides, R. Ludeke and H. J. Wen, 6th International Conference on the Formation of Semiconductor Interfaces (ICFSI), Cardiff, Wales, UK, June 26, 1997.

SPATIALLY AND ENERGY RESOLVED HOT ELECTRON TRANSPORT THROUGH METAL-OXIDE-SILICON STRUCTURES

R. Ludeke, E. Cartier and H.J. Wen
IBM T.J. Watson Research Center, P.O. Box 218, Yorktown Heights NY, 10598

The tip of a scanning tunneling microscope was used to inject hot electrons into thin Pd layers of Pd-SiO₂-Si structures incorporating 75-150 Å thermally grown oxides. The collector currents emanating from the n-type Si(100) substrates for tip biases $V_T \geq 4$ V were measured as a function of eV_T (electron energy) for different oxide biases V_{ox} applied independently across the oxide layers. Threshold shifts with increasing positive V_{ox} were observed for the first time and are attributed to image force lowering of the oxide potential near the metal-oxide interface. The shifts agree well with those predicted by classical image force theory. A zero field threshold energy of 3.99 ± 0.02 eV for the Pd-SiO₂ interface was deduced. Image force effects were also incorporated into Monte Carlo calculations of the energy dependent electron transmission probability T_{ox} across a 150 Å oxide. Favorable comparisons with experiment are observed.

INTRODUCTION

The performance and reliability of modern metal-oxide-semiconductor (MOS) devices are ultimately dependent on the electronic properties of the oxide, specifically SiO₂, and its interfaces with the Si and the gate metal. These properties may be loosely divided into intrinsic properties, such as electron-phonon scattering rates and impact ionization cross sections, and extrinsic properties, such as electric breakdown characteristics, that are determined by defects and impurities in the SiO₂ bulk or at its interfaces. The present understanding of the electronic properties of SiO₂, which have been the subject of intensive studies for well over two decades, are largely based on studies on MOS capacitor structures with techniques such as internal photoemission (1), avalanche injection (2), and photoemission into vacuum (3). These results represent properties, typically averaged over sampling areas 0.01 to 1 mm², that do not necessarily reflect sample variations on a microscopic scale. Further shortcomings of the standard electron injection techniques, including Fowler-Nordheim (F-N) tunneling, are the high oxide fields required to energize the injected electrons. The high fields results in a position dependent kinetic energy distribution of the electrons as they cross the SiO₂ layer, which complicates the determinations of energy dependent properties (4). The achievement of energetic electrons through field acceleration also

becomes increasingly difficult for oxide thicknesses $t_{ox} < 100 \text{ \AA}$, the thickness regime for future VLSI applications. Additional drawbacks of some injection techniques, such as photo-excitation and avalanche injection, is an unavoidable broad energy distribution of the electrons entering the oxide.

As device dimensions shrink, local fluctuations in material properties become increasingly influential, and measured properties averaged over macroscopic dimensions become less relevant at predicting device performance and reliability. Hence a need exists and a trend is emerging to investigate material issues of thin SiO_2/Si layers on a microscopic scale. The use of an atomic force microscope (AFM) to investigate "vertical" transport issues across thin SiO_2 layers has recently been reported (5-7), as well as transport studies using a scanning tunneling microscope (STM) (8,9), in a configuration called Ballistic Electron Emission Microscopy (BEEM) (10). Whereas the AFM studies were performed directly on the oxide using a conducting cantilever/stylus, BEEM requires the use of an MOS structure in order to vary the energy of the electrons injected by the STM tip. Investigations of MOS structures with BEEM have several inherent advantages:

- i) the energy of electrons injected into the SiO_2 conduction band can be arbitrarily selected and independently modified by adjusting the oxide bias, thereby increasing the accessible energy range and enhancing experimental flexibility;
- ii) transport studies are not limited by oxide thickness (150 \AA device-grade oxides have been investigated); and
- iii) the transport phenomena relevant to oxide physics and technology occur over a broad energy range ($\sim 0\text{-}20 \text{ V}$) that is readily accessible with BEEM.

We present here the results of a BEEM investigation of MOS structures composed of thin Pd layers deposited on 75-150 \AA thick device grade oxides thermally grown on Si(100) wafers. From the spectroscopic data, that is the collector current I_c emanating from the Si substrate as a function of tip bias V_T , we derive the energy dependent transmission probability of electrons through oxide layers, which we compare with the probabilities calculated by Monte Carlo methods. The results give unique insights into the role of the different electron-phonon scattering mechanisms. A novel aspect of the work reported here is the demonstration that the oxide field plays a dominant role in the injection process. The most striking observation is a lowering of the injection threshold with increasing oxide field, which is well accounted for by classical image force lowering of the potential step (barrier) between the Fermi level in the metal and bottom of the SiO_2 conduction band at the metal-oxide interface.

EXPERIMENTAL DETAILS

Ballistic Electron Emission Microscopy (BEEM)

BEEM is an STM-based microscopy/spectroscopy that differs from the conventional STM mode by the presence of a thin metal electrode overlying the semiconductor structure to be measured. The sole purpose of this electrode is to supply a conductive ground plane relative to which the STM tip is biased. The tip bias V_T thus determines the energy eV_T of the electrons injected into the metal surface by the STM tip. Provided that the metal film thickness is of the order of the electron scattering length in the metal, or preferably much less, most of the electrons will traverse the metal ballistically to reach the far interface. If a potential barrier exist at that interface, the electrons will backscatter unless their energy eV_T exceeds the barrier height. Traditionally that barrier was a Schottky contact, but may also be one arising from metal-dielectric contacts, such as Au-CaF₂ (11), or Pt-SiO₂ (8,9), overlying a Si substrate. A fraction of the electrons with sufficient energy will overcome the barrier and be collected in the semiconductor in the form of a collector current I_c . The STM is generally operated in the constant tunneling current mode. In addition to the conventional STM microscopy mode that provides the surface topography, the collector current I_c can also be used to simultaneously generate a second image (the BEEM image) that represents the local transmission characteristics of the semiconductor structure. In the spectroscopy mode of BEEM the rastering is stopped and I_c is measured as V_T is ramped over a range that includes the barrier potential. Thus initially I_c is zero until V_T exceeds a threshold value V_0 that represent the effective barrier potential of the device structure.

The energy diagram for a BEEM experiment on a MOS structure is schematically shown in Fig. 1. The condition for injection into the conduction band of the SiO₂ is shown ($V_T > V_0$). The threshold for injection V_0 is about 4 V. In our instrument a maximum value of $V_T = 13$ V can be achieved, which corresponds to a kinetic energy $E_{kin} \sim 9$ eV for the hottest injected carriers relative to the conduction band minimum of the SiO₂. To achieve similar energies by F-N injection into a 5 nm SiO₂ layer would require an electric field of 18 MV. Electric fields can also be applied in the BEEM experiments to further modify the electron energies. An accelerating field (Si substrate positive relative to the metal) supplied by the bias potential V_b is illustrated in Fig. 1. This potential is divided between band bending in the Si (shown here in the inversion conditions) and the potential V_{ox} across the oxide (9). Also shown is an exponential function f_T that represents the energy distribution of electrons injected by the STM tip. f_T becomes narrower with increasing tip bias V_T , exhibiting, for example, a theoretical full width at half maximum of ~ 0.150 eV at $V_T = 6$ V (12).

This energy spread is sufficiently monochromatic for characterizing most hot electron phenomena in oxides.

Sample Preparation

Device-grade SiO_2 layers were thermally grown near 800 °C in dry oxygen on 125 mm Si(100) wafers doped in the low 10^{17} cm^{-3} range. No additional treatments were performed after the oxidation. Oxide thicknesses for the studies reported here ranged from 75 to 150 Å. Approximately $8 \times 15 \text{ mm}^2$ samples were cleaved from the wafers and introduced into the metal deposition chamber of our ultra-high vacuum (UHV) BEEM/surface analysis system. Pd dots, 0.2 mm in diameter, were thermally evaporated onto the SiO_2 through a shadow mask. In order to smooth the surface morphology of the thin (~35 Å) shadow mask. In order to smooth the surface morphology of the thin (~35 Å) Pd films it was necessary to cool the substrate to near 30 K during deposition. This process produced films with a nodular structure typically 80 Å in diameter that protruded $\lesssim 10 \text{ \AA}$ above the valleys. A smooth surface morphology is needed to minimize BEEM image contrast arising from the surface topography of the metal (9). The finished sample was allowed to warm up to room temperature and was then transferred under UHV into the STM chamber. The grounding contact was carefully positioned onto a selected Pd dot by means of three orthogonally mounted Inchworms™. STM images and sets of BEEM spectra were then taken. For each V_b a set of typically 25-36 BEEM spectra were measured in a grid pattern covering a $250 \times 250 \text{ \AA}^2$ area. The results reported here are generally averages over 10 or more similar spectra. Acquisition times per spectra are typically in the 10-20 second range for a 1 to 10 V sweep.

BEEM SPECTROSCOPY RESULTS

BEEM Spectra for 75 Å SiO_2

Representative spectra for a 75 Å oxide MOS structure are shown in Fig. 2 for various positive oxide bias conditions. Both the applied bias V_b and the resulting oxide potential V_{ox} are indicated on the figure. The spectra were taken under a constant tunnel current of 2 nA, which is considerably less than the typical 10 nA currents reported previously on Pt contacts deposited at room temperature (8). The reason for the improved transmission can be partially attributed to an improved morphology of the Pd film and to lower scattering in the Pd films. The spectra are characterized by a rapid increase in I_T beyond the threshold near 4 V, followed by saturation, then a decrease, which in turn is followed by a second increase for $V_T > 8 \text{ V}$. The decrease in I_T at ~ 2

eV above threshold coincides with the onset of acoustic phonon scattering in the oxide and is a clear manifestation of the importance of this scattering mechanism in oxide transport (9,13). At these energies, the strong momentum randomizing phonon collisions cause the electrons to scatter back into the metal. The momentum relaxation rates level off at higher energies and the collector current again increases because the available phase space (density of states) is increasing. Optical phonon scattering is primarily important near threshold and is relevant in determining the transmission probabilities under bias conditions near 0 V (9). With increasing oxide bias V_b the spectra increase in absolute intensity and shift to lower energy. The increase in intensity, particularly for $V_b \lesssim 2$ V, is largely attributable to an increase in the transmission probability in the oxide (9). As will be discussed later, the increases in I_c for $V_b > 2$ V can be attributed to increases in available phase space due to the image force. This effect is also responsible for the observed threshold shifts brought about through the lowering of the effective interface potential, as illustrated by the dashed line in Fig. 1. This will be further discussed in the next section.

In a given set of spectra, variations in the threshold of up to several tenth of a volt were observed, particularly in sets taken with low oxide biases. These threshold shifts are attributed to negative charge residing at the SiO_2 -Si interface. The negative field counters that of the applied V_b and is felt strongest for low values of V_b . For these bias values, only $\sim 20\%$ of the spectra exhibited a common and low threshold value. This number drastically increased for the higher biases. In all cases, the spectra shown represent an average of those that exhibit a common, lowest threshold within a given set of spectra.

Image Force Effects in BEEM Spectra

The threshold values of spectra, such as those shown in Fig. 2, were obtained by fitting a suitable power law to the data in the vicinity of the threshold region (14). The values obtained from the fits are indicated by symbols in Fig. 3. They represent a monotonic decrease of the threshold with increasing oxide field. The likely origin of this effect is the Schottky lowering of the potential maximum near the metal- SiO_2 interface due to the simultaneous presence of an electric field E_{ox} and the image force of the electron in the oxide. The potential $\Phi_{im}(z)$ as a function of the distance z from the interface is given by:

$$\Phi_{im}(z) = -eE_{ox}(1 - z/t_{ox})z - \frac{e^2}{16\pi\epsilon_0\epsilon_{ox}z} \quad [1]$$

and is schematically shown by the dashed curve in Fig. 1. Here, ϵ_0 is the permittivity of free space, $\epsilon_{ox}=3.9$ is the dielectric constant of SiO_2 , and t_{ox} is

the oxide thickness. Setting $d\Phi_{im}(z)/dz = 0$ to find the position of the maximum in the potential, one obtains

$$z_m = \left(\frac{e}{16\pi\epsilon_0\epsilon_{ox}E_{ox}} \right)^{1/2} \text{ cm,} \quad [2]$$

and the lowering of the potential

$$\delta eV_o = \left(\frac{eE_{ox}}{4\pi\epsilon_0\epsilon_{ox}} \right)^{1/2} = \left(\frac{eV_{ox}}{4\pi\epsilon_0\epsilon_{ox}t_{ox}} \right)^{1/2} \text{ eV.} \quad [3]$$

Equation [3] was used to obtain the solid curve in Fig. 3. The fit to the experimental thresholds is quite good for the higher oxide biases. The deviation from the theoretical curve for the lower bias values can be attributed to remnant negative charge effects at the SiO_2 -Si interface that are reflected in spectral threshold shifts, as discussed above. The small deviations at the highest biases are within experimental uncertainty for the determination of the thresholds (± 0.02 eV), but may still be affected by an additional effective lowering of the potential due to tunneling through the top of the barrier. For bias values higher than indicated, the BEEM current was dominated by the F-N tunnel current of the capacitor structure, and thus unmeasurable. From the data we deduce that the flat band threshold ($V_{ox}=0$ V) for Pd/SiO_2 is 3.99 ± 0.02 eV.

TRANSMISSION PROBABILITIES IN SiO_2

Experimental Determination

The collector current can be expressed as

$$\frac{I_c}{I_T} = K\tau_{mo}T_{ox}\tau_{os} \quad [4]$$

where τ_{mo} and τ_{os} are the kinematic transmission probabilities across the metal-oxide and oxide-silicon interfaces (9). T_{ox} is the transmission probability across the oxide, and K is an energy independent constant of order unity that is used as a fitting parameter and includes the attenuation of the injected current in the metal layer. τ_{mo} varies slowly with energy and exhibit little structure (14). $\tau_{os}=1$ for $V_b \gtrsim 0$ V. τ_{mo} can be expressed analytically in a free electron model that is based on the overlap of available conduction band states on either side of the interface, and includes the energy distribution of the electrons injected by the tip, the Fermi function and quantum mechanical transmission probabilities. This is not the case for the transmission probability T_{ox} for the oxide because of the strong electron-phonon scattering (13). As we will dis-

cuss in the next section, T_{ox} can be calculated by numerically integrating the Boltzmann equation. However, T_{ox} can be deduced from the experimental data (9). Transmission across the metal was assumed to be energy independent, a justifiable assumption over an energy range for which the mean free paths are larger than the metal film thickness. In addition, no features in BEEM spectra have been attributed to the metal overlayer, whose primary effect is a featureless attenuation of the injected electrons.

Experimentally T_{ox} is determined by first calculating I_c with eq. [4] assuming $T_{ox}=1$. This curve is fitted at the threshold over a narrow (~ 0.2 eV) energy range. The deviation of the calculated curve from the experimental spectrum is due to the energy dependence of T_{ox} , which is readily determined by dividing the experimental spectrum by the calculated one (8). The result of such a determination of T_{ox} for a 150 Å SiO_2 layer is shown in Fig. 4 for two different values of V_{ox} . As can be seen, the higher positive oxide bias increases the collection efficiency and hence the transmission probability. The peaks in T_{ox} above threshold appear to be artifacts attributed to statistical noise in the data.

Monte Carlo Calculations of T_{ox}

Details of the Monte Carlo simulation used to calculate T_{ox} have been described in Ref. 9. Here we will give a summary and some added details on the treatment of image force effects. The electron transport model used is based on a Monte Carlo integration of the Boltzmann transport equation, which requires a description of the electron motion in the conduction band structure of SiO_2 in the presence of the electric field E_{ox} , as well as a detailed account of the electron scattering processes in the oxide. A single valley conduction band was assumed for the oxide, with an energy dependent effective electron mass $m_0 = 0.5 m_e$ at the bottom of the band. At high energies, the electron mass is assumed to resume the free-electron value m_e . Electron-phonon scattering was based on semi-empirical scattering rates for both longitudinal-optical(LO) phonon scattering - the two dominant LO-phonon modes with energies of 63 and 153 meV were included - and acoustic phonon scattering (15,16).

In our previous work, the following boundary conditions were used to calculate T_{ox} (9). The electrons were isotropically injected into the oxide at a kinetic energy, $E_{kin} = eV_T - eV_o$. For each injection energy, the transmission probability was determined by tracking energy, momentum and position of the injected electrons until they leave the oxide either at the metal contact or at the silicon substrate. Only the latter contribute to the transmitted current. Back-scattering into the SiO_2 from either contact was neglected. This assumption is reasonable because E_{kin} of the exiting electrons is several eV.

Such hot electrons have a high probability of loosing a large fraction of their energy through inelastic electron-electron scattering in the Si (impact ionization), thereby disallowing reentry. The transmission probability T_{ox} can be calculated as,

$$T_{ox} = \frac{n_{Si}}{N}, \quad [5]$$

where N is the number of injected electrons (typically 1000) and n_{Si} is the number of electrons reaching the silicon substrate. T_{ox} calculated in this manner for a 150 Å oxide and for $V_{ox}=4.4$ V ($V_b=5$ V) is shown by the open symbols in Fig. 4. Its value decreases monotonically from unity at threshold (zero kinetic energy at the point of injection) to a value of ~ 0.1 for $V_T=8$ V.

The addition of image force effects into the calculation has pronounced effect on the transmission probabilities. Because of the strong bending of the conduction band near the metal-SiO₂ interface (see Fig. 1, dashed line) in the presence of the image force at high fields E_{ox} , the kinetic energy of the injected electrons are quite large within the region $0 < z < z_m$. As a point of reference, using eqn. [2] with $t_{ox}=75$ Å and for $V_{ox}=4.4, 0.1$ V, $z_m=4, 26$ Å, respectively, values that are comparable to the electron mean free paths in SiO₂ (13). The large E_{kin} within z_m of the interface causes a drastic increase in the scattering rates that dramatically lowers the transmission probabilities. The image force used in the simulation is the classical one (eqn. [1]). The singularity at $z=0$ was removed in a manner described by Fischetti et al. (17). Due to the steep potential gradient at the point of injection, the step increments in the simulations had to be drastically reduced in order not to miss scattering events. This caused a considerable increase in computation times. In addition, it was necessary to assume normal injection of the electrons at the metal-SiO₂ interface, as the assumption of isotropic injection resulted in abnormally small transmission probabilities. The results of two simulations of T_{ox} for $V_{ox}=0.1$ V (circles) and $V_{ox}=4.4$ V (triangles) are shown in Fig. 4. A comparison of the simulations with and without image force effects clearly shows the importance of their inclusion. In physical terms, it is the enhanced acoustic phonon scattering in the region $0 < z < z_m$ that leads to rapid momentum randomization and strong back scattering of the electrons injected near threshold. This effect is absent for a triangular barrier and can only be partially mimicked by introducing isotropic injection conditions. In fact, at threshold such an ad-hoc approach can not succeed because electrons that emit a single phonon will not be able to return to the metal contact without tunneling through the triangular barrier, leading to a significant overestimation of the transmission probability.

DISCUSSION AND CONCLUSIONS

It is clear from the observed threshold shifts of Fig. 2 and the good agreement with classical image force lowering that image force effects are relevant in the injection process, as well as substantial for oxide fields commonly used in transport studies using MOS capacitor structures. Their omission in the simulations of our earlier studies still lead to acceptable agreement with experiment because the studies were mainly made under low E_{ox} (including $E_{ox} < 0$) conditions. A negative E_{ox} shifts the potential energy maximum to the $\text{SiO}_2\text{-Si}$ interface, rendering the image force less effective in modifying the threshold, although still enhancing the scattering rates at the point of injection.

The scattering rates are fundamentally different for the optical and acoustic phonons (13,16), which affects the shape and energy dependence of T_{ox} . The large energies of the LO-phonons lead to strong energy relaxation near the energy of the dominant LO-mode (153 meV). The LO-rate rapidly decreases as the kinetic energy increases (to $\sim 1/10$ within 1 eV) because of the Coulombic nature of the interaction. LO-phonon scattering becomes increasingly forward oriented with increasing electron energy (4). Acoustic phonons have much smaller energies and contribute little to the energy relaxation rate. However, they dominate the momentum relaxation, which increases with electron energy and favors large angle (Umklapp) scattering at kinetic energies $\gtrsim 3$ eV.

These differences between the two phonon types are directly reflected in the BEEM results. The decrease in T_{ox} for $V_T \gtrsim 6$ V ($E_{kin} \gtrsim 2$ eV) in Fig. 4 is due to acoustic phonon scattering, which is also prominently evident in the "raw" BEEM data of Fig. 2 for $V_T > 6$ V. What is not evident *a priori*, is that acoustic phonon scattering is also dominant near threshold when image effects are included. In the region of $z < z_m$, E_{kin} can reach values for which acoustic phonon scattering dominates, thus scattering a large fraction of electrons back into the metal before they reach z_m . This is the cause for the drop in the simulated T_{ox} from near unity to 0.6 when image forces are included (Fig. 4). The agreement between simulation and experimentally determined T_{ox} is quite good for low V_{ox} , but includes a substantial region of discrepancy within 1 eV of threshold for $V_{ox} = 4.4$ V. This discrepancy, already observed for modest biases in our earlier data (9), increases for larger values of V_{ox} (not shown). The reason for this is at present not known, but appears to be related to a field dependency of the quantum mechanical transmission probability (18), which was not included in the simulations thus far. Its inclusion may be questioned on the ground that the SiO_2 is amorphous and that lattice scattering due to disorder would dominate. However, it has been argued that amorphous SiO_2 has a short-range order of 10-20 Å that is comparable to that of crystalline forms of SiO_2 (15). This length exceeds the measured electron mean-free path in SiO_2 .

at most electron energies (13), which leads one to conclude that disorder induced scattering is likely to be small compared to phonon scattering.

An additional observation, that of an enhanced spectral strength with increasing V_{ox} , as shown in Fig. 2, can also be attributed to image force effects. The collector current, as stated in eqn. [4], depends also on τ_{mo} , which includes the overlap of the density of states projected onto the interface plane in reciprocal space (9). It is limited by the density of states of the oxide. However, the image force enhances this overlap at the interface through an increase in E_{kin} , which increases τ_{mo} . This increase is larger than the increase in scattering due to a larger E_{kin} , thereby enhancing the net transmitted current, as observed experimentally.

In summary, we have observed for the first time threshold shifts with increasing oxide biases in BEEM spectra on MOS capacitor structures, and attributed the shifts to image force lowering of the oxide potential near the metal-oxide interface. The shifts agree well with the shifts predicted by classical image force theory. Monte Carlo simulations that also include these effects have been used to calculate the transmission probability T_{ox} for a 150 Å SiO₂ MOS structure. The calculation give new insights into the role of acoustic phonon scattering in determining T_{ox} near threshold. Agreement between experimentally determined probabilities and simulations are good for low oxide fields, but exhibit some discrepancies near threshold for high oxide fields.

ACKNOWLEDGEMENTS

Fruitful discussions with D.J. DiMaria and M.V. Fischetti are gratefully acknowledged, as are the growth efforts of the oxides by C. D'Emic. The experimental aspects have greatly benefited from the technical assistance by M. Prikas. This research was partially supported by the Office of Naval Research, under contract N00014-95-C-0087.

REFERENCES

1. R. Williams, Phys. Rev. **140**, A569 (1965).
2. E.H. Nicollian, A. Goetzberger and C.N. Berglund, Appl. Phys. Lett. **15**, 174 (1969).
3. P.M. Solomon, in The Physics of SiO₂ and its Interfaces, S.T. Pantelides, Editor, p. 35, Pergamon Press, New York (1978).
4. M.V. Fischetti and D.J. DiMaria, in The Physics and Technology of Amorphous SiO₂, Roderick A.B. Devine, Editor, p. 160, Plenum Press, New York (1988).
5. M.P. Murell, M.E. Welland, S.J. O'Shea, T.M.H. Wong, J.R. Barnes, A.W. McKinnon, M. Heyns and S. Verhaverbeke, Appl. Phys. Lett. **62**, 786 (1993).
6. S.J. O'Shea, R.M. Atta, M.P. Murell and M.E. Welland, J. Vac. Sci. Technol. **B 13**, 1945 (1995).
7. K. Saito, M. Matsuda, M. Yasutake and T. Hattori, Jpn. J. Appl. Phys. **34**, L 609 Part 2 (1995).
8. R. Ludeke, A. Bauer and E. Cartier, Appl. Phys. Lett. **66**, 730 (1995).
9. R. Ludeke, A. Bauer and E. Cartier, J. Vac. Sci. Technol., **B 13**, 1830 (1995).
10. W.J. Kaiser and L.D. Bell, Phys. Rev. Lett. **60**, 1406 (1988).
11. M.T. Cuberes, A. Bauer, H.J. Wen, M. Prietsch and G. Kaindl, Appl. Phys. Lett. **64**, 2300 (1994).
12. N.D. Lang, A. Yacoby, and Y. Imry, Phys. Rev. Lett. **63**, 1499 (1989).
13. E. Cartier, D. Arnold, D.J. DiMaria, M.V. Fischetti, P. Braunlich, S.C. Jones, X.A. Shen, R.T. Casper and P.J. Kelly, Reviews of Solid State Science **5**, 531 (1991).
14. R. Ludeke and A. Bauer, Phys. Rev. Lett. **71**, 1760 (1993).
15. M.V. Fischetti, D.J. DiMaria, S.D. Brorson, T.N. Theis and J.R. Kirtley, Phys. Rev. **B 31**, 8124 (1985).
16. D. Arnold, E. Cartier and D.J. DiMaria, Phys. Rev. **B 49**, 10278 (1994).
17. M.V. Fischetti, S.E. Laux and E. Crabbé, J. Appl. Phys. **78**, 1058 (1995).
18. C.R. Crowell and S. M. Sze, J. Appl. Phys. **37**, 2683 (1966).

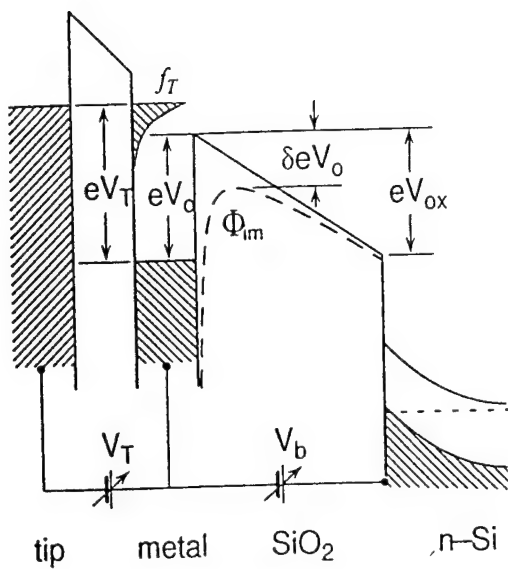


Fig. 1. Schematic energy diagram of a BEEM experiment on an MOS structure under positive oxide bias V_{ox} .

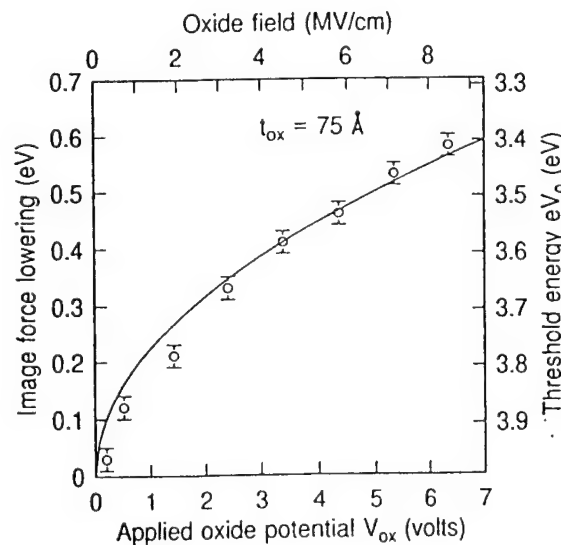


Fig. 3. Observed threshold shifts (circles) for data of Fig. 2 and shifts deduced from classical image force theory (line).

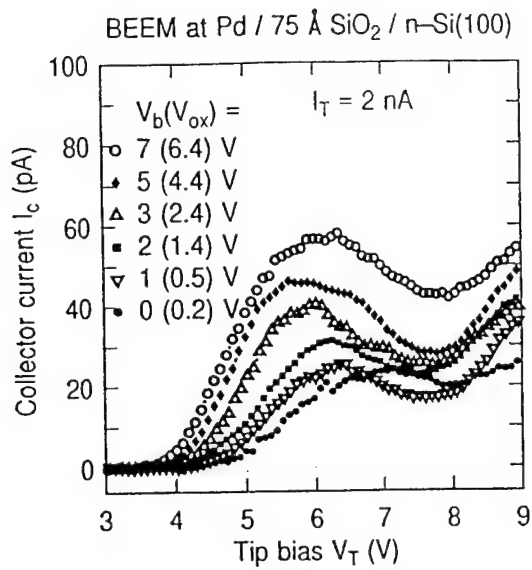


Fig. 2. BEEM spectra (I_T vs. V_T) for a 75 Å SiO_2 layer for indicated positive oxide biases.

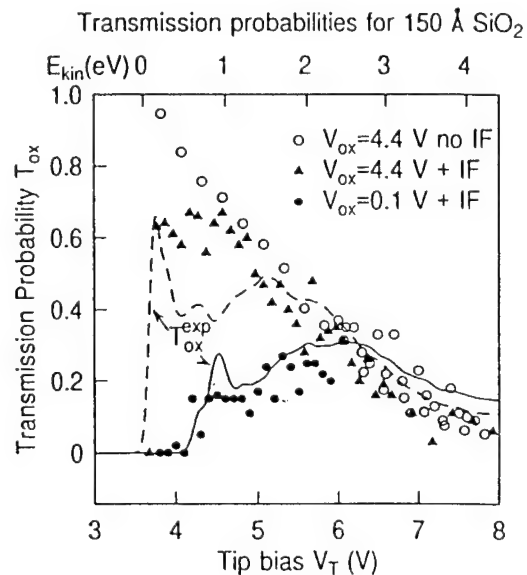


Fig. 4. Transmission probabilities T_{ox} calculated by Monte Carlo methods (symbols) and deduced from experimental data (lines).

Stressing and high field transport studies on device-grade SiO₂ by ballistic electron emission spectroscopy

R. Ludeke,^{a)} H. J. Wen, and E. Cartier

IBM T.J. Watson Research Center, P.O. Box 218, Yorktown Heights, New York 10598

(Received 22 January 1996; accepted 20 April 1996)

The tip of a scanning tunneling microscope was used to inject hot electrons across the gate and into the oxide of a metal-oxide-semiconductor structure. This method, known as ballistic electron emission microscopy (BEEM), allows an arbitrary choice of the energy of the injected electrons, which may be further accelerated by the application of a gate bias. The high current densities and choice of energy make BEEM an attractive method to study hot electron transport and breakdown phenomena in dielectrics. The studies reported here were made on Pd/SiO₂/Si(100) structures with a SiO₂ layer thickness of 3.8 nm. Monte Carlo techniques were used to calculate the spreading of the electron beam as it traverses the oxide. A strong dependence of the spreading on the kinetic energy and oxide thickness were observed. Using the calculated beam spreads to determine current densities and injected charge densities, the charge-to-breakdown (Q_{bd}) was measured for several breakdown sequences. The Q_{bd} 's consistently exceeded by several orders of magnitude the values obtained by conventional Fowler-Nordheim (FN) tunnel injection under high field conditions. Most of the time, breakdowns could not be achieved for 3.8 nm oxides. It is concluded that impurity/defects still control all observed breakdowns; an intrinsic limit—although claimed to have been reached—has not yet been established. Changes in the BEEM spectra with injected electron charge are interpreted in terms of a three stage process to breakdown: (I) electron trap creation and filling at the SiO₂-Si interface, (II) prebreakdown believed to occur through thinning of the oxide that starts at the oxide-Si interface, and (III) oxide punch-through, characterized by an injection threshold ≤ 1 V, close to that for Si. The role of hot hole injection into the SiO₂ valence band was also assessed and deemed a negligible factor in the degradation process under the zero or low oxide biases used in the experiment reported here. © 1996 American Vacuum Society.

I. INTRODUCTION

From a design point of view, future generations of integrated circuits (IC) can be scaled well below the presently manufactured 0.25 μm technology, a projection that requires gate oxides ultimately reaching thicknesses below 2 nm.¹⁻³ However, the reliability of thin gate oxides is one of the most important problems in metal-oxide-semiconductor (MOS) technology. Hence, the ability of manufacturers to mass produce such aggressively scaled ICs will depend on the successful solution of a number of materials and processing problems, among which is the oxide integrity for gate oxides in the 4 nm range and below. This problem has been designated a potential show stopper.⁴ In this thickness range, interface roughness, deviations from stoichiometry, and impurities in the oxide and at the SiO₂-Si interface are believed to be especially critical. Their roles in affecting device reliability and eventually oxide breakdowns are presently not known, and attempts at gaining further understanding of these issues are undertaken at a number of laboratories.⁵⁻¹⁹ A fundamental physical description of oxide degradation and failure are of crucial importance in formulating models that predict device reliability and lifetimes from burn-in and accelerated aging studies.

Oxide breakdown studies are based on failure analysis of electrically stressed MOS capacitor structures or MOS field

effect transistors (FETs). Conventionally, energetic (hot) electrons are injected into the conduction band of the SiO₂ by means of field assisted injection or Fowler-Nordheim (FN) tunneling. Following injection, the electrons gain energy through field acceleration until they reach the opposite interface. The injection may occur in a constant voltage or a constant current mode. The time is measured until device failure occurs (time to breakdown). This time, which is dependent on the fluence or total injected charge, exhibits a complex dependence on field and oxide thickness, which can be rationalized in terms of electron heating in the oxide film.⁹ The total charge injected at failure is referred to as charge to breakdown, Q_{bd} . An example of the dependence of Q_{bd} on oxide field and thickness is shown in Fig. 1.¹⁶ These Q_{bd} 's represent state-of-the-art values on high quality oxides. Their values have increased over the years as oxide growth and substrate cleaning methods have improved, implying that the origin of breakdowns are still associated with defects or impurities. It is general practice, however, that for the best oxides, such as those shown in Fig. 1, the breakdown is addressed as the *intrinsic* mode,^{11,14,20} because breakdown distributions are narrow and quite distinct from early fails or low-field break-down. In a strict sense, however, *intrinsic* would imply an oxide free of defects, with the Q_{bd} 's reflecting the practical upper limit of oxide reliability.

A fundamental and little disputed aspect of oxide breakdown is the role of the hot electrons in generating charge

^{a)}Electronic mail: ludeke@watson.ibm.com

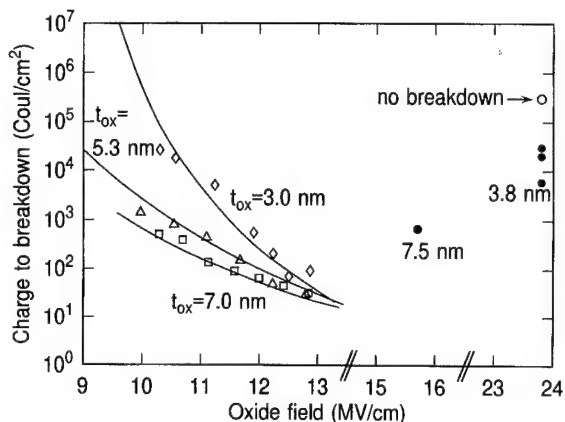


FIG. 1. Normalized charge to breakdown as a function of average electric field for indicated oxide thicknesses at room temperature. These results were obtained through field stressing (injection by FN tunneling at the polysilicon gate). Open data points are experimental results, solid lines are model calculations-adapted from Ref. 16. The solid data points represent oxide failures achieved with BEEM for 3.8 nm and 7.5 nm oxides. The energies of the STM injected electrons were converted to the equivalent field necessary to achieve those values.

traps at the interfaces. Microscopic details of such traps are either lacking or highly speculative, with the exception of traps generated at the cathode due to the presence of hydrogen. The latter is released at the anode through impact with energetic electrons (kinetic energy ≥ 2 eV). The hydrogen diffuses to the cathode where it combines with another hydrogen atom and escapes. The release of the second hydrogen is believed to leave behind an interface state or an electron trap.^{7,9} For thicker oxides under high oxide fields, conditions for which some electrons in the oxide reach energies exceeding 9 eV (the SiO₂ band gap energy), electron-hole pairs may be created in the oxide by impact ionization, with the holes being swept to the injecting cathode where they can be trapped by oxygen vacancies, for example. Electron-hole recombination can then create interface states and electron traps. This mechanism is important only for oxide thicknesses ≥ 10 nm, and will not be further discussed, as these conditions are not encountered in the present experiments. Hole injection into the oxide may also occur at the Si-SiO₂ interface through electron-hole pairs generated by impact ionization of the hot electrons reaching the anode (Si substrate). Although deemed a low efficiency process,²¹ some breakdown models rely exclusively on hole injection as the primary trap creation mechanism at the cathode, and the principal mechanism leading to progressive oxide degradation emanating from the cathode.^{14,22} Other models de-emphasize the role of hole trapping and attribute the start of oxide degradation to electron trapping at the anode.^{12,13,15}

In this article, we present results of stressing thin SiO₂ layers by directly injecting hot electrons into the conduction band of SiO₂ with the tip of a scanning tunneling microscope (STM). This method obviates the need for field acceleration to energize the electrons in the SiO₂ conduction band, although this is still an option that allows additional experimental flexibility. The STM mediated injection provides un-

precedented spatial resolution and a choice of the location of stressing. The results reported here were obtained for 3.8 nm device grade oxides. The principal conclusions of this study are: (i) in general, the oxides were difficult to break down in spite of injecting fluences exceeding by several orders of magnitude the reported Q_{bd} values of conventionally (FN) stressed oxides (such as those in Fig. 1) for comparable anode energies; (ii) when breakdowns were observed, the Q_{bd} 's far exceeded the best-of-breed published results; (iii) strong spectral evidence suggests that breakdown emanates from the anode following a clearly resolved trapping/charging stage and a prebreakdown phase; and (iv) hole injection appears to be inconsequential in breakdown processes initiated by STM-mediated hot electron injection.

II. EXPERIMENTAL DETAILS

A. Ballistic electron emission microscopy/spectroscopy

Ballistic electron emission microscopy (BEEM) is a STM based microscopy that differs from conventional STM by the presence of a thin metallic or other conducting film overlying the substrate—the SiO₂-Si structure in the present case. The sole purpose of this conductive layer is to provide a potential reference plane (generally at ground potential) relative to which the STM tip is biased. The electrons injected into this layer by the STM tip have an energy equal to eV_T , where V_T is the STM tip bias. The thickness of the metal layer is comparable or preferably less than the electron mean free path, so that the electrons can traverse the layer without scattering (ballistically). If their energy is larger than the potential step at the interface—in the present case the difference eV_0 between the Fermi level in the metal and the bottom of the SiO₂ conduction band—the electrons have a finite probability of getting injected into the conduction band, traverse the oxide and of being collected as a collector current I_c in the Si substrate. This probability is dependent on the overlap of conduction band density of states at the interfaces, the transmission probability T_{ox} across the oxide, as well as transmission probabilities of a quantum mechanical origin. These issues have been detailed elsewhere.^{23,24} Suffices to say here that T_{ox} is strongly dependent on the scattering rates of electrons with longitudinal optical phonons (energy dispersive) and acoustical phonons (momentum dispersive), rates which are strongly dependent on the kinetic energy of the electrons.^{21,25} The latter is determined by a combination of the energy at the point of injection ($eV_T - eV_0$) and any gain in energy from field acceleration in the oxide due to the presence of an oxide potential V_{ox} applied by means of a bias potential V_b . An energy diagram for a BEEM experiment is illustrated in Fig. 2 for conditions of positive (accelerating) and negative (retarding) oxide potentials.

In the spectroscopy mode, the raster scan of the STM is stopped and the collector current I_c is measured as V_T is ramped over a range that includes the barrier step potential V_0 . I_c becomes finite once V_T exceeds V_0 for $V_{ox} > 0$ or exceeds $V_0 - V_{ox}$ for $V_{ox} \leq 0$, conditions illustrated in Fig. 2. The STM is generally operated at a constant tunneling cur-

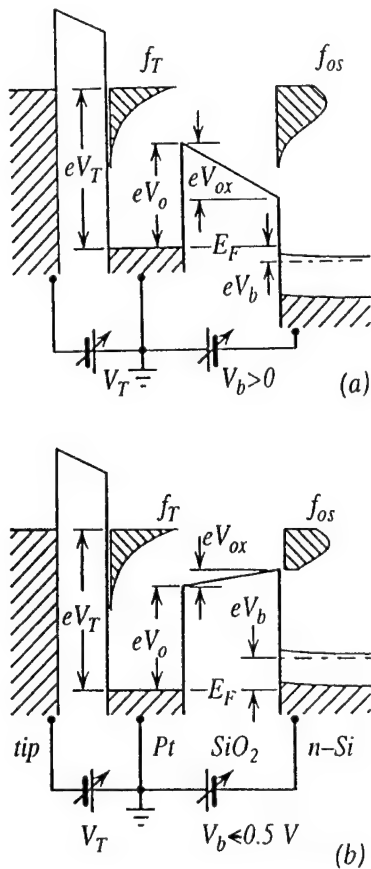


FIG. 2. Schematic energy band diagram for a BEEM experiment on an MOS structure for positive oxide bias V_{ox} (a), and for negative V_{ox} (b). V_{ox} is controlled by means of the gate bias V_b . For Pd/SiO₂/Si, $V_{ox} < 0$ when $V_b < -0.5$ V. The energy of the electrons injected by the STM tip is determined by the tip bias V_T . Their energy distribution is represented by the exponential function f_T . The distribution of the electrons reaching the SiO₂-Si interface is shown by the hatched distributions f_{os} . eV_0 is the energy difference between the Fermi level E_F of the Pd layer and the bottom of the SiO₂ conduction band.

rent $I_T \cdot I_c$ can also be used for image contrast in the scanning mode, thereby generating an electron transmission image of the MOS structure, commonly referred to as a BEEM image,²⁶ that is recorded simultaneously with the STM topographic image.

In stressing studies using BEEM, electrons at a given energy (eV_T) are injected locally (well within a nm) for a given time, with the collector current determining the total fluence. Then an I_c versus V_T spectrum is taken to assess the consequences of the stressing in terms of changes in the local transmission characteristics, including threshold shifts δV_0 . This process is then repeated until either the stressed area moves out of range due to instrument drifts, or the oxide breaks down as evidenced by a low value of V_0 . Alternatively, spectra over a broad energy range are repeatedly taken at the same spot until either of the two previously mentioned events occur. As a point of reference, an I_c of 50 pA collected over an area of 5 nm² (realistic for oxides dominated by ballistic transport, i.e., oxide thickness $t_{ox} \leq 5$ nm) corresponds to a charge injection of 10^3 C/cm² s!¹ In our experi-

ments, we can achieve injection energies of 9 eV. To achieve this value by conventional FN injection, one would need to apply a field of ~ 24 MV/cm to a 5 nm oxide. Still larger effective energies can be achieved with BEEM by applying an accelerating oxide bias.

B. Sample preparation

Device-grade amorphous SiO₂ layers were thermally grown in the range 750–800 °C at 1 atm of dry oxygen for 30–50 min. The substrates were 125-mm-diam Si(100) wafers doped to the low 10^{17} range. No additional treatments were performed after the oxidation. Oxide thicknesses for the studies reported here are 3.8 and 7.5 nm. Approximately 8×15 mm² samples were cleaved from the wafers and introduced into an ultra high vacuum (UHV) preparation chamber. Arrays of Pd dots, 0.2 mm in diameter, were deposited by thermal evaporation of Pd through a shadow mask, with the substrate held at ~ 30 K. The finished sample was allowed to warm up to room temperature and was subsequently transferred under UHV into the STM chamber. The grounding contact needed to bias the tip was carefully positioned onto a selected Pd dot by means of three orthogonally mounted inchwormsTM. Deposition at low temperatures improves the surface morphology of the thin (~ 3.5 nm) Pd films, resulting in a morphology that consisted of a nodular structure typically 8 nm in diameter that protruded ≤ 1 nm above the valleys. An STM image is shown in Fig. 3(a). A smooth surface morphology is needed to minimize BEEM image contrast arising from the surface topography of the metal, which has previously been observed to be strongly reflected in the BEEM image.^{27,28} The corresponding BEEM image of the 3.8 nm Pd/3.8 nm SiO₂/Si(100) structure is shown in Fig. 3(b). The surface topography is clearly replicated in the BEEM image. However, the nodular structure of the topographic image appears rather flat in the BEEM image, that is, there is little evidence that thickness differences in the metal film affect the net transmission. The reason for this is that the mean free paths in the metal film are larger than the thickness of the metal film. However, near the grain boundaries the scattering drastically increases, resulting in the electrons being scattered outside the acceptance cone for transmission across the metal-SiO₂ interface.²⁹

The change from the previously used Pt gates²³ to the presently used Pd metallurgy revealed a somewhat surprising enhancement in the net transmission characteristics across the MOS device. This enhancement is shown in Fig. 4, where we compare the BEEM spectrum of a 3.3 nm Pt film with that of a Pd film of comparable thickness, with both films deposited on 3.8 nm oxides. It should be noted that a tunneling current of 10 nA was used with the Pt gates,²³ whereas for Pd, this current was typically in the 1–5 nA range. The enhanced transmission for Pd not only provides enhanced statistics, but makes stressing studies much easier by allowing larger currents to be injected into the oxide. An added advantage of lower tunneling currents lies in the improved collimated nature of the injected current. This is a direct result from the increased tunnel gap during injection at

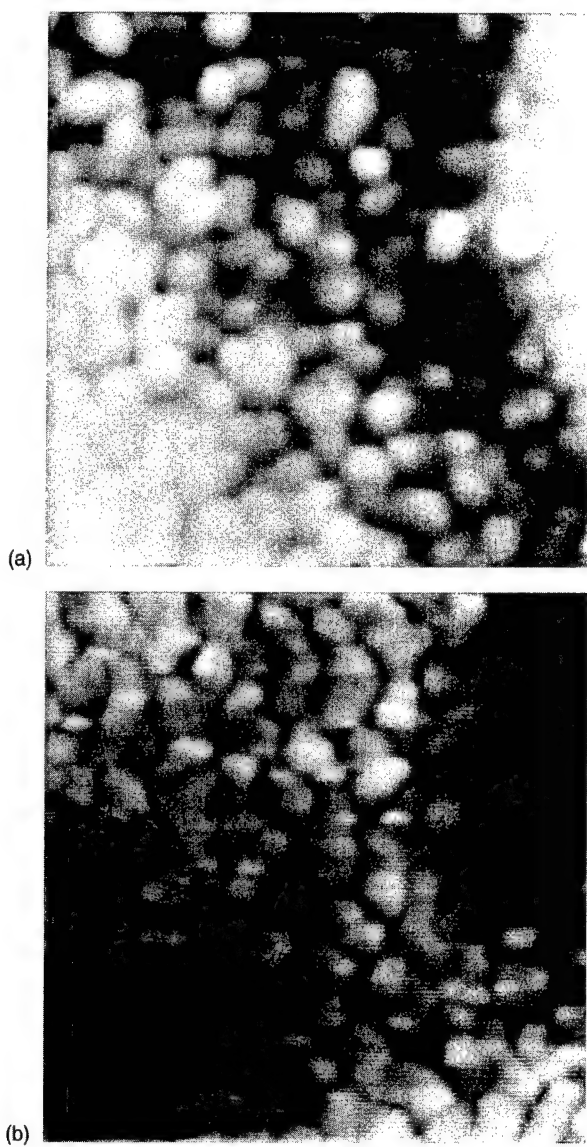


FIG. 3. $100 \times 100 \text{ nm}^2$ STM topograph (a) and BEEM image (b) of a 3 nm Pd/3.8 nm $\text{SiO}_2/\text{Si}(100)$ structure. Black-white range over the image is 3 nm in topography, and 100 pA in BEEM. $V_T = -6 \text{ V}$, $I_T = 2 \text{ nA}$, $V_b = 0 \text{ V}$. The average peak to valley in the topography image is less than 1 nm.

lower currents.³⁰ A more collimated electron beam is subject to fewer scattering events, which enhances the transmission across the MOS structure. This in turn results in crisper spectral features, as shown in Fig. 5. As the data indicates, under optimal conditions useful spectra can be readily obtained with tunnel currents of $\leq 0.5 \text{ nA}$.

C. Monte Carlo (MC) simulations

Details of the (MC) simulations, which are based on the code developed by Fischetti *et al.*,²⁵ have been given elsewhere.^{23,24} In the present application, MC simulations were used to estimate the spreading of the electron beam as it traverses the SiO_2 layer. Knowledge of the spreading is needed in order to estimate current and charge densities during electrical stressing of the SiO_2 . To calculate the spread-

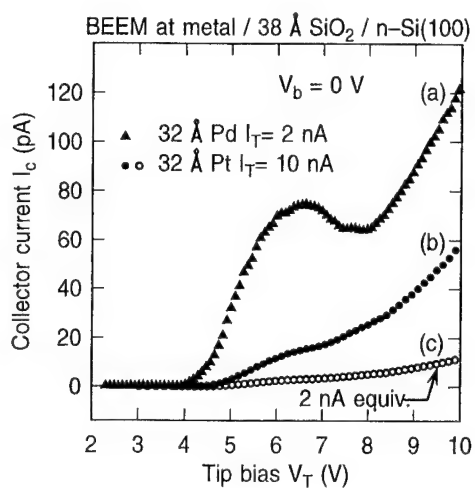


FIG. 4. Comparison of BEEM spectra for similar MOS structures except for the gate metal. Pd gates allow substantially larger transmission than the previously used Pt gates. Spectrum (a) is for a Pd gate, (b) for a Pt gate and (c) is curve (b) normalized to a 2 nA tunnel current.

ing in the oxide, normal injection across the Pd– SiO_2 interface at one single point was assumed (delta function). The potential in the oxide included image force lowering and the applied oxide bias. Electrons returning to the metal were discarded. The position of the transmitted electrons was recorded and the normalized local current density $j(r)/I_{in}$, was calculated after sufficient statistics had been acquired (typically 10^5 electrons). The distance r is measured away from the injection point, and I_{in} is the injection current. In Fig. 6, typical results of the simulations are summarized for different combinations of the oxide thickness, the oxide bias, and the tip bias. The two distributions for $V_T = 5.5$ (open sym-

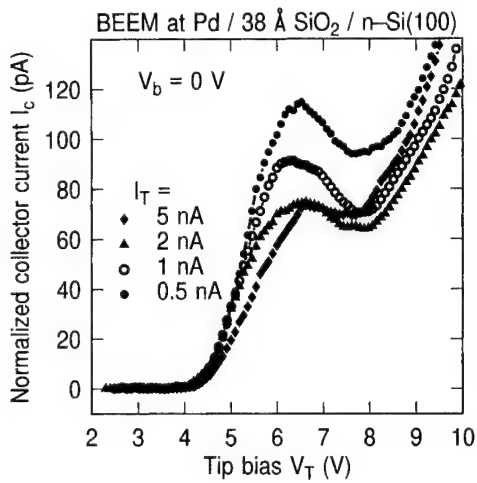


FIG. 5. Normalized collector currents for a Pd/ $\text{SiO}_2/\text{Si}(100)$ structure for a range of indicated tunnel currents. The curves have been normalized to the $I_T = 2 \text{ nA}$ spectrum, to which the ordinate scale refers. The relative intensities scale inversely with I_T , which is attributed to the higher collimation (and transmission) for the smaller I_T 's, for which the STM tip-surface distance is greater.

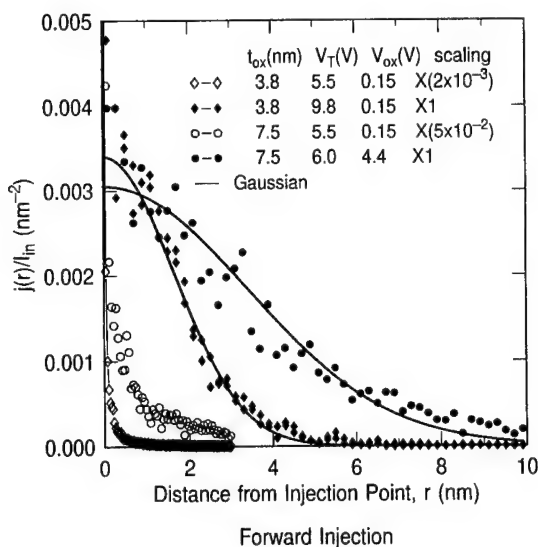


Fig. 6. Spatial distribution of the normalized current densities at the Si/SiO₂ interface after electron transport through 3.8 and 7.5-nm-thick SiO₂ films as calculated by MC simulations for various bias conditions. The figure serves to illustrate the strong dependence of the beam spreading on the electron energy in the oxide. At low electron energies (open symbols, $V_T=5.5$ V) little broadening is predicted. Strong broadening will occur if electrons are either injected at high energy (3.8 nm, $V_T=9.8$ V full diamonds), or if the electrons are heated inside the oxide by a strong electric field (7.5 nm, $V_{ox}=4.4$ V full dots).

bols) were done at a small accelerating bias. At this tip bias, the electrons travel at an energy of 1.5 eV through the oxide, where phonon scattering is small and mostly via longitudinal optical phonons (forward scattering). This results in a streaming type motion in the presence of a small accelerating field and leads to very little beam broadening by the transport through the oxide. In these cases, the beam size on the substrate side is expected to be comparable to the size of the injection beam. The two distributions were scaled to the same heights in such a way that the additional broadening in the thicker oxide can be clearly seen. The peak at $r=0$ overshoots the y axis of the plot by one order of magnitude, such that actual broadening is considerably smaller than suggested at a first glance.

Most interestingly, considerably broader distributions are obtained if the electrons are either injected at high energies (for 3.8 nm film, solid diamonds) or accelerated by a strong electric field (7.5 nm film, solid circles) in the oxide. The broadening is caused by a rapid increase of the acoustic phonon scattering (Umklapp dominated, isotropic, quasi-elastic scattering) with increasing kinetic energy of the electrons. This scattering dominates at energies above 3 eV and leads to strong backscattering that both reduces the overall transmission efficiency and quite significantly spreads the beam. In the 3.8 nm film, the electrons were injected at a tip bias of 9.8 V, which corresponds to an initial electron energy in the oxide of about 5.8 eV. Alternatively, electrons were injected at an energy of 1.5 eV into a 7.5 nm oxide and subsequently heated by a strong electric field, such that their average energy reaches values of 4–5 eV. Again, significant beam

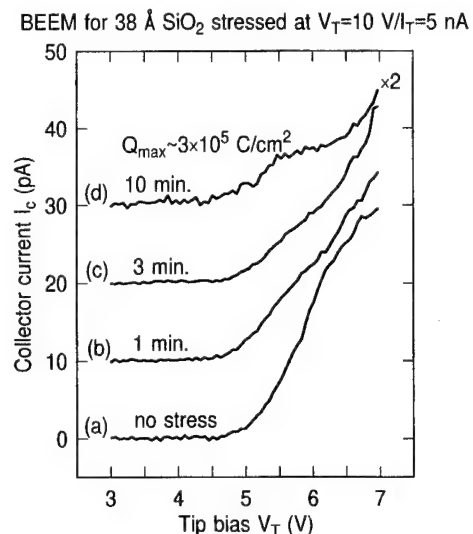


Fig. 7. Spectra of threshold region for BEEM-stressed Pd/3.8 nm SiO₂/Si structure. The kinetic energy of the injected electrons is ~6 eV. The total injected charge was $\sim 3 \times 10^5$ C/cm². This charge is plotted in Fig. 1. No oxide breakdown occurred. The stressing location is indicated in Fig. 8.

spreading is predicted and the increased oxide thickness leads to additional broadening. Under conditions where the electrons reach energies in excess of 3–4 eV, the beam size on the substrate side is predicted to be largely determined by the spreading in the oxide. This has to be taken into account when calculating local current densities and charge to breakdown.

In the present determination of current and charge densities, it was assumed that $r=2.3$ nm. For this value 74% of the current injected into the oxide is included in the density determinations. The remaining current in the tail of the distribution contributes little to the density. This leads to an effective area of 17 nm² for the beam spread at the SiO₂–Si interface for the 3.8 nm oxide at a kinetic energy of 5.8 eV.

III. STRESS MEASUREMENTS

As pointed out before, the mere fact of taking a BEEM spectrum, such as those of Figs. 4 and 5, involves the injection of large charges into the oxide. A conservative, lower estimate of this charge is 300 C/cm² over a time span (about 1 s) that corresponds to a voltage change $\Delta V_T \approx 0.5$ V during a typical spectral sweep. For electrons injected at $V_T=10$ V, with $V_b=0$ V, their kinetic energy in the oxide is ~6 eV, a value achieved with FN injection only in the presence of an oxide field of ~24 MV/cm for a 3.8 nm oxide. At such large energies or equivalent oxide fields, breakdown should be observed frequently if the local oxide characteristics were similar to those of the quality oxides represented in Fig. 1. However, breakdowns in 3.8 nm oxides were seldom observed during routine spectral scans with $1 \leq V_T \leq 10$ V and $V_b=0$ V, and never observed on oxides ≥ 7 nm thick unless a positive bias was applied. An extreme case of stressing without breakdown is illustrated in Fig. 7, which depicts a series of spectral scans taken at the same location of an MOS structure

with $t_{\text{ox}}=3.8 \text{ nm}$. A spectrum was taken after each dosage of injected charge. Except for an almost imperceptible increase in the threshold position, indicative of some charging at the SiO₂-Si interface, no spectral changes are observed after 3 min of stressing ($Q_{\text{inj}} \sim 10^5 \text{ C/cm}^2$). After 10 min of stressing the spectrum weakened and shifted to slightly higher energies. The weakening of the spectrum is indicative of some additional scattering in the oxide, possibly due to the generation of interface defects. These may be precursors to breakdown (see following section), but the evidence of a conventional BEEM spectrum and threshold indicates that the oxide is still largely intact. Additional stressing was not possible because of instrument drift, which, although extremely small at this particular time ($\sim 2.5 \text{ nm/h}$), caused the STM tip to drift out of the stressed area ($\sim 1 \text{ nm}^2$) over the duration of the stressing time. $Q_{\text{inj}} \sim 3 \times 10^5 \text{ C/cm}^2$ after completion of the stressing. This value, marked on Fig. 1 at an equivalent field of 24 MV/cm, is totally incompatible with the rest of the Q_{bd} 's for conventionally stressed oxides, strongly suggesting again that the Q_{bd} 's of Fig. 1 are not intrinsic but defect controlled. The stressing did not cause any observable damage in the Pd film. Topography and BEEM images of the stressed area are shown in Fig. 8(a) and 8(b), respectively. The stressed area has been marked with a cross. The BEEM image barely shows an area of slightly weakened transmission at the stress point.

Stress experiments that resulted in breakdown were successful rather infrequently (of the order of 10%), which suggest that the sites where breakdowns occur are quite dispersed, of rather low density and most likely controlled by impurities and/or defects. A breakdown sequence is illustrated in Fig. 9, which consisted of applying a $V_T=10 \text{ V}$ (kinetic energy ~ 6 eV in the oxide) for predetermined time intervals, each of which was followed by a spectral scan. After stressing for 10 s (curve *b*), a threshold shift to higher energies is clearly observed. A partial breakdown is observed after stressing for 20 s, with the threshold moving down to about 1 V and the collector current increasing by orders of magnitude (the dashed curves represent a 100× demagnification). The low threshold is a clear manifestation that the oxide barrier has disappeared and that a direct contact exists to the Si substrate. The total injected charge to breakdown corresponds to $\sim 6 \times 10^3 \text{ C/cm}^2$. Another breakdown sequence is shown in Fig. 10. The oxide was repeatedly stressed at the same point of a 3.8 nm oxide with $V_T=10 \text{ V}$ and $V_b=0 \text{ V}$. Spectral scans were taken after each stress application. Only a fraction of the scans are shown in the figure, starting with the first scan (a) on a virgin section of the sample and ending with spectrum (g), which represents the locally broken down oxide. The sequence shows a weakening of the transmitted collector current that is accompanied by threshold shifts to higher energies. After injecting $\sim 7 \times 10^3 \text{ C/cm}^2$ the intensities again increase, as shown in spectrum (d), and the thresholds move progressively to lower energies ultimately reaching the breakdown stage (curve *g*) after $\sim 3 \times 10^4 \text{ C/cm}^2$ have been injected. Following such breakdown events, the surface of the MOS structure is

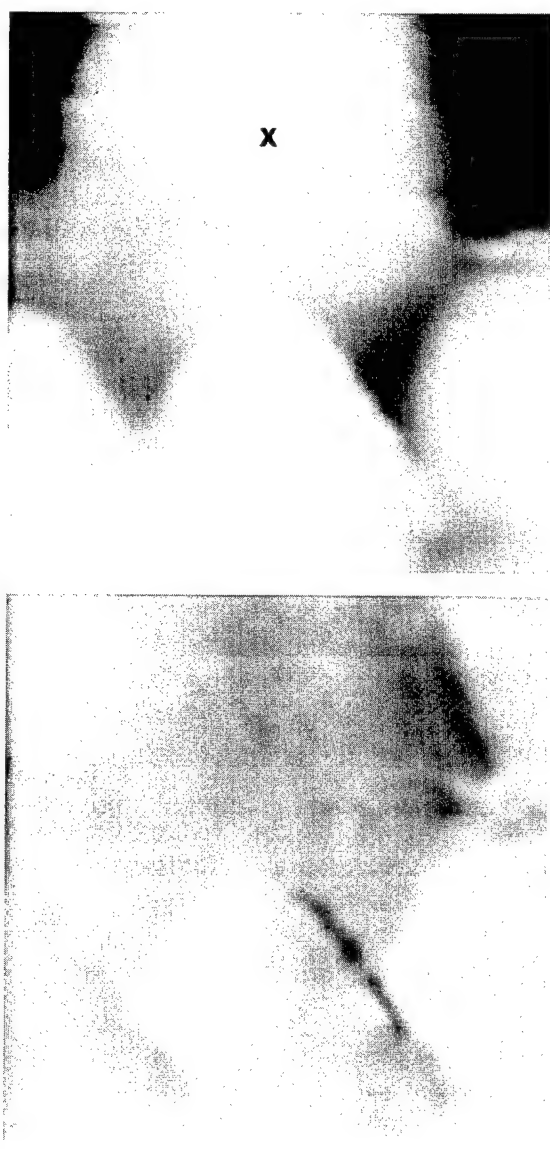


FIG. 8. $12.5 \times 12.5 \text{ nm}^2$ STM topograph (a) and BEEM image (b) of a 3 nm Pd/3.8 nm SiO₂/Si(100) structure. Black-white range over the image is 1.9 nm in topography, and 30 pA in BEEM. $V_T=-5 \text{ V}$, $I_T=5 \text{ nA}$, $V_b=0 \text{ V}$. The location of the BEEM stressing area is marked an x.

heavily damaged. The damaged area is of the order of 10 nm across, and generally consists of a crater with surrounding rough hillocks of dimensions of 5–10 nm. It should be emphasized that the damage resulting from the breakdown is not due to a tip crash, but appears to be the result of the large currents injected locally and/or discharge of injected trapped charge in the stressed area. The morphology in the prebreakdown phase was not investigated.

IV. DISCUSSION AND CONCLUSIONS

A key feature of the stressing and breakdown studies with BEEM is the initial shift of the threshold V_0 to higher values. This shift is plotted as a function of injected charge in Fig. 11 for the data of Fig. 10. The increase δV_0 , together with the attenuation of the intensity of I_0 , depicted in Fig. 10, is

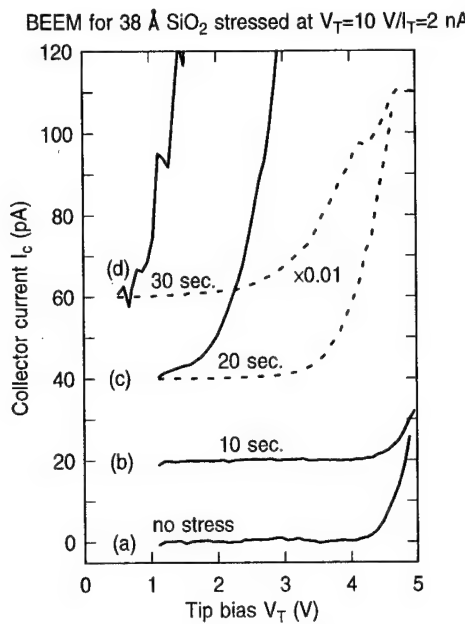


FIG. 9. A successful breakdown sequence for a 3.8 nm oxide stressed with 6 eV (kinetic energy) electrons. The shift to higher V_0 between curve (a) and (b) is due to negative charge at the SiO_2 -Si interface. $V_b=0$ V. Total injected charge to breakdown (defined by reaching $V_0 \sim 1$ V, as in curve c) is $\sim 6 \times 10^3 \text{ C/cm}^2$.

equivalent to applying a negative bias to the oxide, as demonstrated in a previous publication.²³ The responsible field for this shift is due to electrons trapped in the vicinity of the SiO_2 -Si interface. This view is consistent with previous observations based on FN injection.^{10,12,13,15} However, one could argue that in the present case the injected electrons are

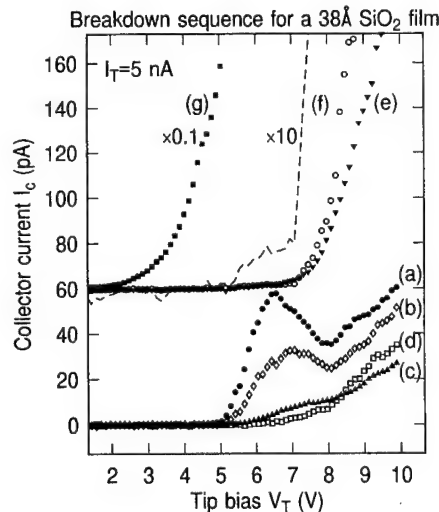


FIG. 10. Oxide breakdown sequence from no stress (curve a) to fully broken down oxide region or punch through (curve g) for a 3.8 nm oxide. The oxide was stressed between spectra at $V_T=10$ V for 10–30 s periods. Not every spectrum and stress sequence is shown. $V_b=0$ V. Of interest is a second threshold in the stressed area beginning with spectrum (d) and clearly seen in the magnified spectrum (f). The threshold is ~ 2 V above V_0 and appears to be related to trap generation reported in Ref. 9.

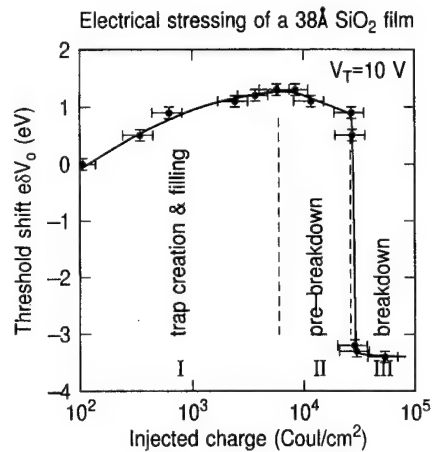


FIG. 11. Shifts in the fundamental threshold V_0 as a function of injected charge taken from the data of Fig. 10. Three phases of stressing are depicted. Prebreakdown commences after a maximum has been reached and coincides with the appearance of a second threshold, as discussed in Fig. 10.

already sufficiently energetic to cause damage at the injecting Pd electrode, a scenario that cannot entirely be excluded. However, any trapped charge in such hypothetical states would be screened by the metal and contribute a negligible amount to the threshold shift. A simple calculation, with the metallic screening treated by the classical image force,³¹ gives the following relationship between $e\delta V_0$ and the distance d of the charge from the metal-SiO₂ interface:

$$e\delta V_0 = \frac{e^2}{4\pi\epsilon_0\epsilon_r} \left[\frac{1}{r} - \left(\frac{1}{r^2 + 4d^2} \right)^{1/2} \right], \quad (1)$$

where r is the distance between the trapped charge and the injected electron as it crosses the plane parallel to the interface that includes the trap. ϵ_0 and ϵ_r are, respectively, the permittivity of vacuum and the dielectric constant. Clearly, $e\delta V_0$ approaches zero as d approaches the metal-SiO₂ interface, so that the trapped charge must reside in the vicinity of the SiO₂-Si interface to produce a sizeable δV_0 . For a shift of 1 eV or more, with the negatively charged trap 3.5 nm from the Pd-SiO₂ interface, the electron must pass within 0.35 nm of the trap. Alternatively, if the charge were uniformly distributed, a 1 eV shift corresponds to an interface charge of 5.7×10^{12} electrons/cm². In a realistic situation there will be a number of filled traps, as evidenced by the increasing shift with dosage, and the net shift will arise from the sum of contributions from each individual charge. During stressing, Fig. 6 indicates that the electron beam has spread over an area of radius ~ 2 nm with tails of the distribution extending somewhat farther. At the threshold, however, the beam has spread very little and is thus more sensitive to local distributions. Fluctuations in thresholds are indeed observed even for unstressed areas a few nanometers apart, corroborating the highly localized resolution of BEEM, particularly for thin oxides. Consequently, the shifts in V_0 represent interface trap charging on a truly local (< 1 nm) scale, but the trap creation from the energetic electrons occurs over an area of ~ 20 nm² for a 3.8 nm thick oxide.

Trap creation and charging also occur for $V_T < 10$ V, as can be ascertained from curve (a) of Fig. 10 which represents a spectrum for a previously unstressed area. Yet its intensity for $V_T \geq 8$ V is uncharacteristically low compared to those of Figs. 4 and 5. The lower intensity implies an ongoing charging as the data is taken. This phenomenon is not observed in spectra taken randomly over the sample and suggests the presence of a weak spot at the point of injection that ultimately results in breakdown. Upon further stressing a maximum in δV_0 is reached, as shown in Fig. 11, which indicates that a maximum was reached in the density of negative charge trapped near the SiO₂-Si interface. A negative charge in the absence of an applied bias leads to a local energy profile similar to that depicted in Fig. 2(b). Further injection leads to a gradual decrease of V_0 , which may result from an increased charge leakage due to the deterioration of the oxide or from either positive charges generated at the SiO₂-Si interface (anode), or electron trapping at the cathode.⁹ The maximum in V_0 coincides with the onset of larger currents for $V_T \geq 7$ eV, as seen in spectra (d)-(f). The enhanced current is due to an ongoing modification of the oxide, the simplest explanation being the destruction of the oxide that gradually progresses into the oxide starting from the SiO₂-Si interface. The local thinning explains the dramatic increases in I_c as the stressing progresses, curves (e) and (f). The $\times 10$ enhanced curve (f), shown by the dashed line, clearly reveals a remnant of a conventional BEEM spectrum with a threshold at 4.8 eV. The reason for the weakened threshold region in this spectrum is attributed to added scattering at defect sites in the progressively deteriorating oxide. However, once V_T exceeds 7 V, the oxide breakdown proceeds rapidly as suggested by the rapid rise of I_c . Upon completion of spectrum (f) punch-through of the oxide resulted, as indicated by the low $V_0 \approx 1$ V, and the large currents.

The onset of the current enhancement in what we refer to as the prebreakdown region in Fig. 11, and represented in Fig. 10 by curves (c)-(f), is approximately 2 eV above V_0 . Perhaps coincidentally, this energy also corresponds to the threshold for hydrogen release and trap formation at the anode of MOS capacitor structures.⁷ The hydrogen then diffuses to the cathode (injecting electrode) to produce electron traps. As discussed above, our measurements are not sensitive to such traps at the injecting interface, and it is not clear at present how the hydrogen release would affect the oxide breakdown scenario depicted here. Nevertheless, if present, electron trapping at the cathode would increase the accelerating field in the oxide, thereby accounting for both a decrease in V_0 in the prebreakdown regime, and an enhancement of oxide deterioration by increasing the electron energy as they reach the anode. The implication that most of the events that lead to breakdown are initiated at the SiO₂-Si interface (anode) is also consistent with the MC simulations. These indicate that beam spreading due to acoustic phonon scattering is accentuated in the oxide away from the injecting interface. Since this scattering occurs with little loss/gain in energy, the effectiveness in damaging the oxide is enhanced as the electrons sample a greater volume, which increases the

probability that an electron encounters a weak spots where the breakdown may be initiated. This breakdown scenario starting at the oxide-Si interface is consistent with those proposed by several other workers,^{12,13,15,32} but inconsistent with oxide degradation attributed to hot hole injection into the oxide at the SiO₂-Si interface.¹⁴ The hot holes are created by impact ionization of the hot electrons as they enter the Si. The hole injection model requires the high fields present in conventional FN injection to accelerate the holes toward the cathode. This situation does not apply in the present case for a 3.8 nm oxide with no applied bias. In fact, the electron traps initially created by the stressing produce a retarding field for the holes, keeping them from being injected into the valence band of the SiO₂.

The Q_{bd} values obtained from various breakdown events have been plotted in Fig. 1, as well as the total charge injected in one experiment that did not reach breakdown. The injection energies of the BEEM experiments were converted to an equivalent electric field that would achieve the same energies under FN injection.³³ The stressing current at maximum tip bias was converted to a charge density by multiplying I_c by the time and dividing the product by the area of the electron beam reaching the SiO₂-Si interface (~ 17 nm²), as determined from the MC simulations depicted in Fig. 6. The Q_{bd} 's thus obtained fall consistently above the curves obtained from conventional stress experiments.¹⁶ These were interpreted in terms of an intrinsic breakdown limit, a conclusion that is challenged by the present results. Even the new points obtained here are not intrinsic, as much higher charge dosages did not routinely cause breakdowns in the 3.8 nm oxides. Consequently we conclude that even the higher observed breakdown dosages are still limited by extrinsic effects, either defects or impurities at the interface. This conclusion offers hope that in the future, device lifetimes and device reliability can be considerably improved. Our observations are consistent with an increase in oxide robustness observed over the years as capacitor areas and device dimensions shrink.³⁴⁻³⁶ It is generally acknowledged that these trends are directly attributable to a decreasing probability of finding defects/impurities in the oxide as the device areas decrease.

It is a reasonable question to ask if Q_{bd} 's obtained with BEEM can be compared to those obtained under FN injection. The conversion of the former from an energy scale to an effective electric field scale assumes that only the electron energy is important and that field effects in the FN stress mode contribute negligibly to the breakdown. Previous studies have shown that the principal trap, defect and interface state generation mechanisms are dependent solely on the kinetic energy of the hot electrons injected into the oxide, with no evidence of a field dependence other than to accelerate the electrons to the required energies for defect generation.^{7,9,37} This is not to say that the field is unimportant but rather that thus far there is little evidence of the field playing a primary role in determining the breakdown mechanism. For the electric field stressed modes, such as FN, defect formation can also occur from holes generated by impact

ionization in both the SiO₂ and the Si (anode) with subsequent injection into the SiO₂ valence band. The field is thus important to accelerate the holes towards the cathode where they can create traps and interface states. These processes also depend on the energy of the holes.³⁸ However, hole generation depends on the energy gained by the electrons, with a minimum oxide potential of 8 V being required for hole injection to occur from the Si (anode).³⁸ This potential threshold is higher than the gate voltages used by Schuegraf and Hu¹⁶ to obtain the data of Fig. 1 with the exception that the data for the 7 nm oxide beyond 11 MV/cm correspond to a gate voltage exceeding 8 V. However, no change in slope is apparent in the data of the 7 nm oxide, strongly suggesting that hole injection for thin oxides and for the given field ranges is not a principal contributor to breakdown. It is also worth noting that the BEEM-stressed Q_{bd} for the 7.5 nm oxide in Fig. 1 was obtained with an applied field of ~ 6 MV/cm in addition to a kinetic energy of 4.2 eV at the point of injection. From these discussions, it can be surmised that the oxide field has a yet to be identified role on Q_{bd} 's for thin oxides (aside from accelerating the electrons in FN stressing). Consequently, the comparison of FN-stressed and BEEM-stressed data is a reasonable undertaking with any additional, but still unknown, field enhanced contributions in the FN case being compensated by the higher energies sustained by the BEEM-injected electrons throughout their passage across the oxide.

V. CONCLUSIONS

In conclusion, we have demonstrated that spatially highly resolved stress studies using the STM can give new insights into breakdown phenomena in ultrathin oxides. Unlike conventional stressing by means of FN injection, the present technique allows an arbitrary choice of injected electron energies, thereby greatly simplifying the injection and oxide transport processes. The latter have also been modeled by MC simulations, from which the spreading of the electron beam as it traverses the oxide was calculated. Stress induced breakdowns under conditions that far exceed those for conventionally stressed state-of-the-art oxides imply that breakdowns are still controlled by defects/impurities in the oxide, and that an intrinsic breakdown limit has not yet been reached. When observed, the breakdown scenario suggests a three-fold sequence of initial trap creation and filling, followed by a prebreakdown phase that appeared to be associated with a progressive oxide deterioration starting at the SiO₂-Si interface, and finally a catastrophic punch through, characterized by a very low barrier to electron injection. The data furthermore suggests that hole transport in the oxide is unlikely to occur for the low oxide biases used in the present experiments.

ACKNOWLEDGMENTS

Fruitful discussions with D. J. DiMaria and M. V. Fischetti are gratefully acknowledged, as are the growth efforts of the samples by C. D'Emic. The experimental aspects have greatly benefited from the technical assistance by M. Prikas.

This research was partially supported by the Office of Naval Research, under Contract No. N00014-95-C-0087.

- ¹C. Hu, Proc. IEEE **81**, 682 (1993).
- ²C. A. Mead, Analog Integrated Circuits and Signal Processing **6**, 9 (1994).
- ³Y. Taur, Y.-J. Mii, D. J. Frank, H.-S. Wong, D. A. Buchanan, S. J. Wind, S. A. Rishton, G. A. Sai-Halasz, and E. J. Nowak, IBM J. Res. Develop. **39**, 245 (1995).
- ⁴Semiconductor Technology Workshop, Working Group Reports, Semiconductor Industry Association, San Jose, 1993, p. 27.
- ⁵J. C. Lee, I.-C. Chen, and C. Hu, IEEE Trans. Electron Devices **35**, 2268 (1988).
- ⁶P. Olivo, T. N. Nguyen, and B. Ricco, IEEE Trans. Electron Devices **35**, 2259 (1988).
- ⁷D. J. DiMaria and J. W. Stasiak, J. Appl. Phys. **65**, 2342 (1989).
- ⁸P. Olivo, T. N. Nguyen, and B. Ricco, IEEE Trans. Electron Devices **38**, 527 (1991).
- ⁹D. J. DiMaria, E. Cartier, and D. Arnold, J. Appl. Phys. **73**, 3367 (1993).
- ¹⁰P. P. Apte, T. Kubota, and K. C. Saraswat, J. Electrochem. Soc. **140**, 770 (1993).
- ¹¹M. Nafría, J. Suñé, and X. Aymerich, IEEE Trans. Electron Devices **40**, 1662 (1993).
- ¹²P. P. Apte and K. C. Saraswat, IEEE Electron Device Lett. **14**, 512 (1993).
- ¹³L. K. Han, M. Bhat, D. Wristers, J. Fulford, and D. L. Kwong, Proceedings of the IEEE International Electron Device Meeting, 1994, p. 617.
- ¹⁴K. F. Schuegraf and C. Hu, IEEE Trans. Electron Devices **41**, 761 (1994).
- ¹⁵S.-H. Lee, B.-J. Cho, J.-C. Kim, and S.-H. Choi, Proceedings of the IEEE International Electron Device Meeting 1994, p. 605.
- ¹⁶K. F. Schuegraf, D. Park, and C. Hu, Proceedings of the IEEE International Electron Device Meeting, 1994, p. 609.
- ¹⁷M. Depas, B. Vermeire, P. W. Mertens, M. Meuris, and M. M. Heyns, Semicond. Sci. Technol. **10**, 753 (1995).
- ¹⁸C.-H. Lin, J. Cable, and J. C. S. Woo, IEEE Trans. Electron Devices **42**, 1329 (1995).
- ¹⁹E. Hasegawa, A. Ishitani, K. Akimoto, M. Tsukiji, and N. Ohta, J. Electrochem. Soc. **142**, 273 (1995).
- ²⁰D. J. DiMaria, D. Arnold, and E. Cartier, Appl. Phys. Lett. **61**, 2329 (1992).
- ²¹D. Arnold, E. Cartier, and D. J. DiMaria, Phys. Rev. B **49**, 10278 (1994).
- ²²I.-C. Chen, S. Holland, and C. Hu, IEEE Trans. Electron Devices **32**, 413 (1985).
- ²³R. Ludeke, A. Bauer, and E. Cartier, J. Vac. Sci. Technol. B **13**, 1830 (1995); Appl. Phys. Lett. **66**, 730 (1995).
- ²⁴R. Ludeke, E. Cartier, and H. J. Wen, J. Electrochem. Soc. (to be published).
- ²⁵M. V. Fischetti, D. J. DiMaria, S. D. Brorson, T. N. Theis, and J. R. Kirtley, Phys. Rev. B **31**, 8124 (1985).
- ²⁶W. J. Kaiser and L. D. Bell, Phys. Rev. Lett. **60**, 1406 (1988).
- ²⁷R. Ludeke and A. Bauer, Phys. Rev. Lett. **71**, 1760 (1993); J. Vac. Sci. Technol. A **12**, 1910 (1994); Phys. Scr. T **55**, 90 (1994).
- ²⁸R. Ludeke, J. Vac. Sci. Technol. A **11**, 786 (1993).
- ²⁹L. D. Bell, W. J. Kaiser, M. H. Hecht, and L. C. Davis, in *Scanning Tunneling Microscopy*, edited by J. E. Stroscio and W. J. Kaiser (Academic, San Diego, CA, 1993), p. 307.
- ³⁰N. D. Lang, A. Yacoby, and Y. Imry, Phys. Rev. Lett. **63**, 1499 (1989).
- ³¹M. V. Fischetti, S. E. Laux, and E. Crabbé, J. Appl. Phys. **78**, 1058 (1995).
- ³²D. R. Wolters and A. T. A. Zegers-Van Duynhoven, in *The Physics and Technology of Amorphous SiO₂*, edited by A. B. Devine (Plenum, New York, 1988), p. 391.
- ³³For FN injection and quasi-ballistic transport, the equivalent oxide field F necessary to accelerate an electron to reach an energy E relative to the SiO₂ conduction band at the anode is: $F \approx (qV_0 + E)/qw$, where $V_0 = 3.15$ V was assumed for a polysilicon gate, w is the oxide thickness and q is the electron charge.
- ³⁴J. Suñé, I. Placencia, N. Barniol, E. Farrés, F. Martín, and X. Aymerich, Thin Solid Films **185**, 347 (1990).
- ³⁵R. P. Vollertsen and W. G. Kleppmann, Proc. IEEE **4**, 75 (1991).
- ³⁶D. J. Dumin, J. R. Maddux, R. S. Scott, and R. Subramonian, IEEE Trans. Electron Devices **41**, 1570 (1994).
- ³⁷E. Cartier and D. J. DiMaria, Microelectron. Eng. **22**, 207 (1993).
- ³⁸D. J. DiMaria, E. Cartier, and D. A. Buchanan, J. Appl. Phys. (in press).

Image force effects and the dielectric response of SiO₂ in electron transport across metal–oxide–semiconductor structures

H. J. Wen, R. Ludeke,^{a)} D. M. Newns, and S. H. Lo
IBM T. J. Watson Research Center, Yorktown Heights, New York 10598

(Received 14 October 1996; accepted 8 January 1997)

Hot electrons of variable energy were injected from a scanning tunneling microscope tip into a Pd/SiO₂/Si(100) metal–oxide–semiconductor structure. An analysis of the emerging collector current in the Si substrate, a technique known as ballistic electron emission microscopy, revealed a monotonic barrier height lowering with increasing positive oxide bias, in excellent agreement with a scaled classical image force theory. Calculations using the WKB approximation suggest a negligible contribution to the observed shifts from electrons tunneling through the barrier. From an extrapolation to zero oxide field the Pd–SiO₂ barrier height of 4.08 ± 0.02 eV was deduced. An image-force dielectric constant of 2.74 in between the so-called optical (2.15) and static (3.9) dielectric constant was determined. In order to understand this intermediate value, a theoretical calculation of a retarded image force on the moving electron is carried out for the first time. The calculations yield an image-force dielectric constant of 2.69, that is consistent with the experimentally determined value. This intermediate dielectric constant is evidence for electron–phonon interaction and corresponds to an average dielectric response integrated over the time of progression of the electron in SiO₂. © 1997 American Vacuum Society. [S0734-2101(97)05403-1]

I. INTRODUCTION

It is well known that image force effects lower the barrier height at a metal-semiconductor or metal-insulator interface, and that tunneling through the barrier may give a lower effective barrier as well.¹ In general, both effects increase with an increasing external field applied across the insulator, although in the context of Fowler–Nordheim tunneling the image force potential was ignored by some workers.^{2,3} The tunneling induced barrier lowering is usually small in nondegenerate semiconductors, as well as in relatively thick insulator layers. The image force induced barrier lowering (image force lowering) was traditionally determined by internal photoemission measurements.^{4–6} From the observed barrier lowering as a function of the applied electric field an effective dielectric constant can be derived, often called the image-force-dielectric constant. With this technique, barrier heights between metal/SiO₂ and Si/SiO₂ interfaces and their field dependencies have been studied.^{5,6} In these studies, an image-force-dielectric constant of $\epsilon_{ox} = 2.15$, equal to the optical dielectric constant in SiO₂, was determined, a value that has been accepted ever since.^{7,8} Arguments supporting that value were based on the transit time τ that an electron needs to move from the metal–oxide (MO) interface ($z=0$) to the potential maximum ($z=z_m$). In the case of Si the transit time was deduced to be between 1×10^{-14} s and 5×10^{-15} s and it was argued that the image-force dielectric constant should be comparable to the dielectric constant for electromagnetic radiation of these periods. A corresponding value equal to the static dielectric constant of 12 was determined, which agreed with the value obtained by internal photoemission measurements.¹ This somewhat fortuitous agreement results from the nonpolar nature of Si, whose dielectric constant is

essentially constant for electromagnetic radiation from dc to $\lambda = 1 \mu\text{m}$.⁹ In contrast, SiO₂ is a polar material, whose optical phonon modes result in strong variations of the dielectric constant in the range of $\lambda = 40$ to $4 \mu\text{m}$.⁹ In this case a transit time of 5×10^{-15} s, which corresponds to $\lambda = 1 \mu\text{m}$, should correspond to a dielectric constant at optical frequencies, i.e., 2.15. It should be noted that a response characterized by the optical dielectric constant means that the lattice polarization of the medium cannot follow the moving electron; in other words, the particle moves so fast that the electron–phonon interaction does not occur. Consequently, the moving electron senses a stronger image force than at rest. To the authors' opinion, the traditional transit time argument that the image-force-dielectric constant should be comparable to the dielectric constant for electromagnetic radiation of the period equal to the transit time lacks physical justification and therefore is not a measure for predicting a dielectric response. In order to know how the dielectric medium responds to a moving electron, we need to consider the details of the electron–phonon interaction.

In this work, we use ballistic electron emission microscopy (BEEM) as a new technique to study the field dependent barrier lowering at the Pd/SiO₂ interface of metal–oxide–semiconductor (MOS) structures. We demonstrate that the barrier lowering exhibits a linear dependence on the square root of the oxide bias. In order to know whether or not the observed barrier lowering contains a contribution from electrons tunneling through the barrier, the WKB approximation is used to calculate tunneling probabilities. Our calculations lead us to conclude that a tunneling contribution is negligible in our method of measuring barrier heights. Therefore the barrier lowering only includes contributions from image force effects. Since the experimental results exhibit a behavior proportional to the square root of the applied

^{a)}Electronic mail: ludeke@watson.ibm.com

oxide field, the classical image force theory is considered to be valid. In this way, an image-force dielectric constant of 2.74 is determined, a value that is considerably larger than the optical dielectric constant. In order to assess the origin for such a value between 2.15 and 3.9, we formulate a novel theoretical model of transport dynamics in the interface region. In this treatment, an electron–phonon interaction force, which ultimately determines the dielectric response to fall between the two extreme cases, is introduced into the equation of motion for the electron. We establish that the “transit time” τ is a kind of time scale for the electron–phonon interaction, i.e., as long as $\omega\tau>0$ (ω is a phonon frequency), there is always some electron–phonon interaction contribution; only when $\omega\tau\rightarrow 0$ will the term representing electron–phonon interaction disappear and the medium respond with an optical dielectric constant. For the condition of our BEEM experiment, an image-force-dielectric constant of 2.69 was obtained by solving the equation numerically. This value is in excellent agreement with the experimentally determined one of 2.74. However, the concept of time for a fast moving particle as presented here may be of questionable applicability, for which a quantum mechanical treatment is more suitable as discussed in Sec. IV.

II. EXPERIMENTAL DETAILS

A. Ballistic electron emission microscopy

BEEM is a scanning tunnel microscope (STM)-based microscopy/spectroscopy that differs from the conventional STM mode by the presence of a thin metal electrode overlying the semiconductor structure to be measured. The sole purpose of this electrode is to supply a conductive ground plane relative to which the STM tip is biased. In our studies hot electrons were injected from the tip into Pd/ SiO_2 /Si MOS structures. An energy band diagram for the present BEEM experiment is shown in Fig. 1. The tip bias V_T is referenced to the thin grounded metal film (the metal Fermi level is defined to be the zero potential). Therefore, eV_T is a direct measure of the kinetic energy of the electrons injected into the metal. Provided that the metal film thickness is of the order of the electron scattering length in the metal, most of the electrons will traverse the metal ballistically to reach the far interface. It should be noted here that no features in BEEM spectra have been attributed to the metal layer, except for causing a featureless attenuation of the injected electrons. Therefore, transmission across the metal is assumed to be independent of the electron energy, a justifiable assumption over an energy range for which the mean free paths are larger than the metal thickness. Electrons with sufficient energy to overcome the potential barrier at the Pd/ SiO_2 interface may ultimately reach the semiconductor conduction band, where they are collected, forming a collector current I_C . As a function of increasing V_T , I_C is zero until V_T reaches a threshold (V_0), a value equal to the interface barrier height. The value of V_0 is usually extracted from the spectra by means of a model fit. A separate gate bias (V_b) between the metal and semiconductor can also be readily applied within the BEEM configuration. This allows com-

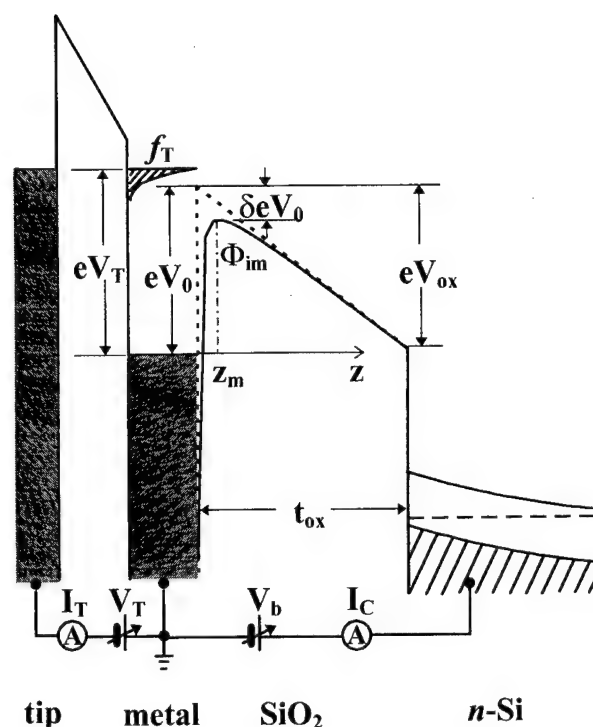


FIG. 1. Schematic energy diagram of a BEEM experiment on a MOS structure under positive oxide bias V_{ox} .

plete control over the field in the oxide and facilitates field dependent transport studies. As V_b affects both the potential drop across the oxide (V_{ox}) and the band bending of the Si at the SiO_2 –Si interface, their relationship is nonlinear and is obtained by solving the appropriate Poisson equation with the assumption of a negligible density of interface states.^{7,10} In addition, V_{ox} also includes a part of the built in potential of 0.50 V due to the work function difference between the metal and the semiconductor. In the present case, the work function of Pd is larger than that of *n*-type Si, therefore the flat band ($V_{\text{ox}}=0$) condition requires a negative gate bias proportional to the work function difference.

B. Sample preparation

Device quality oxide layers were thermally grown near 800 °C in dry oxygen on 125 mm diameter Si(100) wafers doped in the low 10^{17} cm^{-3} range. No additional treatments were made after oxidation. Here we report studies on an oxide layer with a thickness of $75 \pm 1 \text{ \AA}$; the thickness was determined with an ellipsometer. Approximately $2 \times 12 \text{ mm}^2$ pieces were cut from the wafers and introduced into an UHV sample preparation chamber, where Pd dots, 0.2 mm in diameter, were thermally evaporated through a shadow mask. During deposition, the substrate was held at a temperature of about 30 K. That was necessary in order to inhibit surface diffusion. A roughness of about 10 Å for a Pd film of thickness of 35 Å was measured. After evaporation, the sample was allowed to warm up to room temperature and was subsequently transferred under UHV into the STM

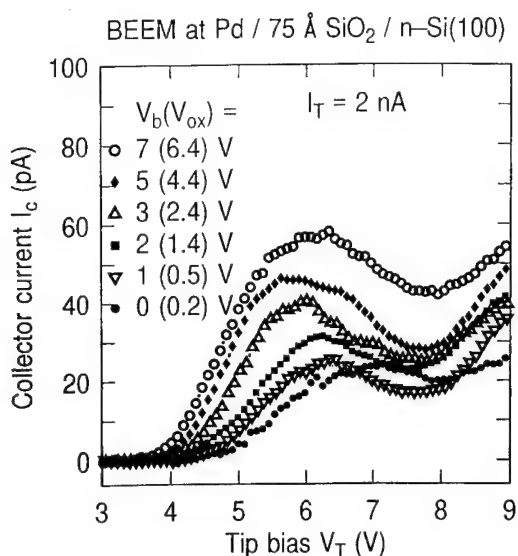


FIG. 2. BEEM spectra (I_T vs V_T) for a 75 Å SiO₂ layer for indicated positive oxide biases taken at $I_T = 2$ nA.

chamber, where the BEEM grounding contact was gently positioned onto a selected Pd dot by means of three orthogonally mounted inchworms. MOS structures with leakage resistance $\geq 10^{12}$ Ω were generally suitable for our studies. All data were taken in the conventional, feedback controlled constant tunnel current (I_T) mode. For each V_b a set of, typically, 16–25 spectra were taken in a grid pattern covering a area of 250×250 Å². The BEEM data reported here are generally averages over approximately ten similar spectra. Additional details regarding the STM and data acquisition can be found elsewhere.¹¹ It is noted here that within a given set of spectra, variations in the threshold of up to several tenths of a volt were observed, which are assigned to a negative charge at the SiO₂-Si interface region.^{12,13} The spectra presented here were averaged over those that exhibited a common, lowest threshold in a given set of spectra.

C. BEEM spectra for 75 Å SiO₂

Representative spectra for a 75 Å oxide of MOS structures are shown in Fig. 2 for various positive oxide biases. Both the applied bias V_b and the resulting potential drop V_{ox} across the oxide are indicated on the figure. The spectra are characterized by a rapid increase in I_T beyond the threshold near 4 V, followed by a saturation, then a decrease, which in turn is followed by a second increase for $V_T > 8$ V. The decrease in I_T at ~ 2 V above threshold is evidence for the onset of acoustic phonon scattering in the oxide and is a clear manifestation of the importance of this scattering mechanism in oxide transport.^{10,14} At these energies, the strong momentum randomizing phonon collisions cause the electrons to scatter back into the metal. The momentum relaxation rates level off at higher energies and the collector current again increases because the density of states, i.e., the available phase space, is increasing. Optical phonon scattering is important only near threshold. With increasing oxide

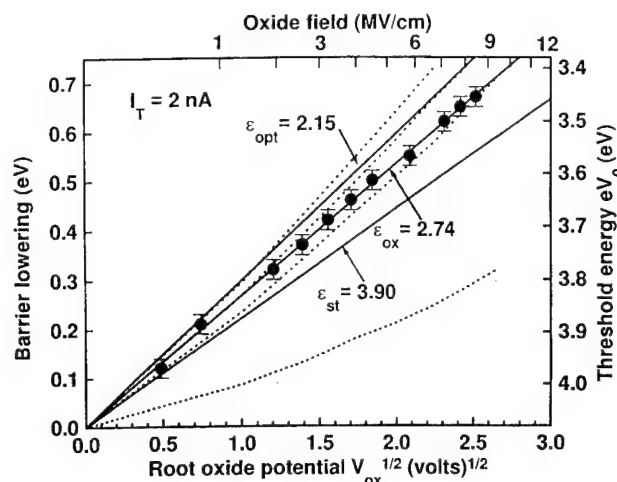


FIG. 3. Observed threshold shifts (solid circle) resulting from fits to the BEEM data of Fig. 2, as well as shifts deduced from classical image force theory (solid lines, corresponding to $\epsilon_{ox} = 2.15$, 2.74, and 3.90, respectively). Dotted lines are theoretical results calculated by WKB approximation; the three upper most lines correspond to $\epsilon_{ox} = 2.15$, 2.74, and 3.90; the bottom line was obtained without considering image force effects.

bias V_b , the spectra clearly show a shift to low energy as well as an increase in absolute intensity. The increase in intensity is attributed both to an increase in the transmission probability in the oxide due to the positive bias,¹⁰ and to increases in available phase space due to the image force potential.¹² In this article we will only concentrate on the threshold shifts (barrier lowering). The observed barrier lowering derived from the spectra of Fig. 2 are plotted as a function of $V_{ox}^{1/2}$ and are shown by solid circles in Fig. 3. These threshold values were obtained by fitting the BEEM data with a simulated spectrum of the current in the vicinity of the threshold region ($V_0 \pm 0.5$ eV).¹⁰ The simulation is based on the assumption that the transmission probability in the oxide is constant and field independent over the considered threshold region. The latter assumption implies that quantum mechanic contributions to the transmission probability, which are included in our theoretical BEEM spectrum, are also relatively field independent—an assertion supported by the excellent agreement between experiment and Monte Carlo simulated oxide transmission probabilities for positive oxide fields.¹⁰ In order to determine the threshold energy, the experimental data were visually fitted by varying only the threshold energy and the intensity prefactor over the energy window, with emphasis on an excellent fit on the steeply rising part of the spectrum just above the threshold. Since this portion of the spectrum is devoid of any contributions from electrons tunneling through the barrier, we speculate that the determined threshold energy is not influenced by tunneling contributions, a conclusion supported by the excellent agreement of the threshold energies with classical image force theory, as well as by calculations based on the WKB approximation. In addition, we did not observe a rising background with increasing oxide fields that would suggest contributions from tunneling electrons. Nevertheless, the issue of tunnel contributions will be considered and discussed in

detail in Sec. III. The fit to the data can be made to within ± 0.02 eV, as marked in the figure. It should be noted that the right axis scale for the threshold is only in reference to the experimental data (solid circle), while the left axis (image force lowering relative to the flat band condition in the oxide) is valid for all curves. In Fig. 3 we clearly see that the experimental data are distributed along a straight line, a strong manifestation of the validity of the classical image force theory as discussed in the following.

III. DATA INTERPRETATION

A. Experimental result: $\epsilon_{\text{ox}}=2.74$

Since the barrier lowering exhibits a linear behavior, a least-squares linear fit with a chi value of only 0.0022 was made to the data, as shown in Fig. 3. Originally the fitted curve missed the origin, which indicates that our initial estimate of $V_{\text{ox}}=0.45$ V for zero bias was off by 53 mV. Accordingly, the V_{ox} values for the data were uniformly shifted by this amount. The fitted curve must go through the origin, since at zero field ($V_{\text{ox}}=0$) the barrier height is the same in the presence or absence of the image force potential. By extrapolating to $V_{\text{ox}}=0$ V, a threshold value of 4.08 ± 0.02 eV is deduced for the Pd–SiO₂ potential barrier under flat band conditions. The straight line implies that the concept of a classical image force expression: $\Phi_{\text{im}}(z)=eV_0 - eV_{\text{ox}}(z/t_{\text{ox}}) - (e^2/16\pi\epsilon_0\epsilon_{\text{ox}}z)$ is still valid, from which the maximum position of the potential: $z_m=[et_{\text{ox}}/16\pi\epsilon_0\epsilon_{\text{ox}}V_{\text{ox}}]^{1/2}$ and the barrier lowering: $\delta eV_0 = [eV_{\text{ox}}/4\pi\epsilon_0\epsilon_{\text{ox}}t_{\text{ox}}]^{1/2}$ eV due to the image force are derived, where ϵ_0 is the permittivity of free space, ϵ_{ox} is the dielectric constant of SiO₂, and t_{ox} is the oxide thickness. The energy difference between the Fermi level in the metal and the bottom of the conduction band in the oxide is described as eV_0 , as indicated in Fig. 1. The expression of the barrier lowering δeV_0 indicates that the slope of the fitted line is equal to $[e/4\pi\epsilon_0\epsilon_{\text{ox}}t_{\text{ox}}]^{1/2}$, with ϵ_{ox} as the only adjustable parameter, whose value is determined to be 2.74 ± 0.11 . This uncertainty was estimated from the error range in the data. This value is considerably larger than the optical dielectric constant (2.15) and lies in between it and the static value (3.9). In the following, we demonstrate through a model calculation that $\epsilon_{\text{ox}}=2.74$ is more accurate in describing the dielectric response than the optical one, though, that value is supported by internal photoemission results.^{5,6,15}

B. Assessment of tunneling contribution

Before we present the theoretical model describing the dynamic dielectric response, we need to clarify the issue of whether or not the observed barrier lowering includes contributions from electrons tunneling through the barrier. It is, in principle, possible that electron tunneling contributes to the observed barrier lowering, even though the described determination of the threshold does not include a tunneling current. We state two facts to conclude that a tunneling contribution to the determined barrier lowering is negligible: (a) the barrier lowering clearly shows a linear dependence on the

square root of the oxide bias $V_{\text{ox}}^{1/2}$, a result valid only within the classical image force theory, since a tunneling contribution would give a nonlinear behavior; and (b) theoretical results based on the WKB approximation exclude any substantial contributions for tunneling electrons in the determination of the BEEM thresholds. It should be kept in mind that the latter corresponds to electrons going over the barrier at nearly unit transmission probability, whereas that for tunneling electrons diminishes exponentially rather rapidly for energies below the barrier maximum. These concepts were quantified and the results are presented by dotted lines in Fig. 3. The approach taken here is to assess the field dependence of tunneling electrons at a given transmission probability. Unlike standard tunnel current calculations for MOS capacitor structures, the tunnel current for BEEM experiments cannot be calculated analytically due to the complexity of hot electron scattering processes in the metal and at the interfaces. Calculations were carried out with and without the inclusion of image force lowering, as well as for the various $\epsilon_{\text{ox}}=2.15$, 2.74, and 3.90 values. An electron effective mass at the bottom of the conduction band of $0.5 m_0$ (m_0 is the electron rest mass) was used.⁸ No strong dependence on the mass, although varied from $0.3 m_0$ to $0.5 m_0$, was observed. The singularity of the image force potential at the interface ($z=0$) was removed by assuming $\Phi_{\text{im}}(z)=0$ for $\Phi_{\text{im}}(z) \leq 0$. Tunneling probabilities were calculated as a function of tip voltage for various oxide biases. A virtual threshold energy can be set at a certain tunneling probability, then barrier lowering relative to the zero field case can be plotted as a function of $V_{\text{ox}}^{1/2}$. The tip voltages at the tunneling probability of 50% are plotted by dotted lines in Fig. 3. The three uppermost lines were calculated with $\epsilon_{\text{ox}}=2.15$, 2.74, and 3.90; the bottom curve was obtained by excluding the image force potential altogether. First of all, it is clearly seen that the bottom curve deviates irrecoverably from the experimental data. This allows us to conclude that the image force potential plays the main role in the observed barrier lowering. Second, the theoretical curves are nonlinear, a behavior that increases with increasing bias and become even more dominant for lower tunneling probabilities. We argue that the absence of such deviations from linearity in our data precludes substantial contributions of tunneling in our methodology of determining thresholds. This statement does not mean that tunneling is absent, but rather that its contribution below threshold is inconsequential to the determination of the threshold. This is attributed to the rapid increase of phase space for transmission above threshold that entirely determines the collector current behavior on which the threshold were fitted. For a tunneling probability of 100%, the calculated results exhibit the expected linear behavior that exactly matches solutions of the classical image force theory for all three values of ϵ_{ox} . Therefore we conclude that the observed barrier lowerings are solely attributed to the image force potential, with an effective dielectric constant of 2.74. It should be noted that Monte Carlo calculation by Fischetti *et al.*¹⁶ lead to similar conclusions.

C. Classical calculation of retarded image force: $\epsilon_{ox}=2.69$

In order to understand the origin of the experimentally determined $\epsilon_{ox}=2.74$, we now present a theoretical calculation of the effective dielectric constant for an electron in a model BEEM experiment.

In the model, the electron moving in SiO₂ as a classical particle with trajectory $\mathbf{r}_p(t)$ and charge e produces a potential $V(\mathbf{r},t)$. We calculate $V(\mathbf{r},t)$ and then obtain the force acting back on the particle at $\mathbf{r}=\mathbf{r}_p$. The dielectric medium is assumed uniform with a local dielectric response. The presence of the metal/dielectric interface is taken into account by introducing the image of the particle. Then all potentials in the left-hand half space ($z<0$) are automatically zero when we define the potential on the plane ($z=0$) to be zero. We start from the formula¹⁷

$$V(\mathbf{r},t)=V^0(\mathbf{r},t)+\int d^3r' \mathbf{P}(\mathbf{r}',t) \times \nabla_{r'} \frac{1}{|\mathbf{r}-\mathbf{r}'|}, \quad (1)$$

where $V(\mathbf{r},t)$ is the total potential, $V^0(\mathbf{r},t)$ the external potential caused by the particle and its image in vacuum, and $\mathbf{P}(\mathbf{r},t)$ is the induced polarization in the dielectric medium given by

$$\mathbf{P}(\mathbf{r},t)=-\int_0^t \alpha(t-t') \nabla V(\mathbf{r},t') dt', \quad (2)$$

where $\alpha(t-t')$ is the local response or susceptibility per unit volume. Gaussian units are used throughout. Using Green's theorem, Eq. (2) becomes

$$V(z,t)+4\pi \int_0^t dt' \alpha(t-t') V(z,t') = V^0(z,t), \quad (3)$$

where \mathbf{r} is replaced by z , since the particle in our case is traveling along the z -axis. Equation 3 is solved by taking its Laplace transform. After some manipulations and inverse Laplace transformations, the expression for the time dependent potential is finally obtained as:

$$V(z,t)=+\frac{1}{\epsilon_0} \left[\frac{e}{z+z_p(t)} \right] - \left(\frac{\epsilon_s-\epsilon_o}{\epsilon_s \epsilon_o} \right) \times \int_0^t \omega^2(t-t') e^{-\omega(t-t')} \left[\frac{e}{z+z_p(t')} \right] dt', \quad (4)$$

where the phonon response is described by $\alpha(t)=\omega^2 t e^{-\omega t}$. The latter is obtained from the Fourier transform of the probability distribution $w(x)=4\omega^3 x/\pi(x^2+\omega^2)^2$, and represents a Debye-like power law behavior at low frequencies with a high frequency cutoff, the simplest form of a broadened phonon spectrum short of the actual multimode distribution. For SiO₂ the higher lying optical mode ($\omega=0.153$ eV⁹) was assumed to represent the oxide, $\epsilon_s=3.9$ and $\epsilon_0=2.15$. It must be noted that the first term in Eq. 4 represents only the image term of the external potential and a self-energy term representing the quantum mechanical polaron cloud surrounding the particle is not included in Eq. 4, since the particle is treated classically. The integral term rep-

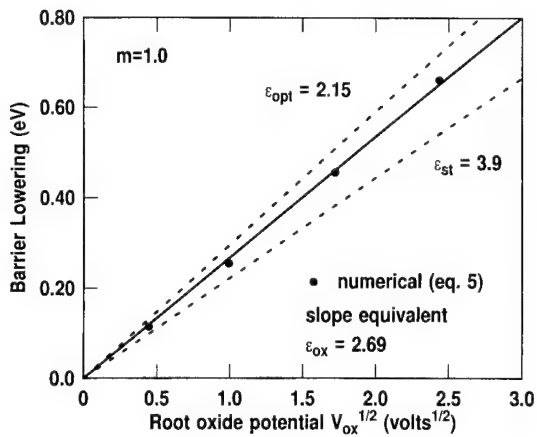


FIG. 4. Results from a classical calculation of the retarded image force in a polarizable medium near a metal interface. Solid circles are numerical results. The slope fitted to the numerical results is equivalent to an effective dielectric constant $\epsilon_{ox}=2.69$. The two dotted lines represent the optic (2.15) and the static (3.9) limits, respectively.

resents the effect of electron–phonon interaction over a time period t . Since the phonons are described by harmonic oscillators without damping, the electron–phonon interaction does not transfer any energy from the electron to the dielectric. The total energy of the electron is thus conserved. The equation of motion is obtained by differentiating Eq. 4:

$$-m \frac{d^2 z_p}{dt^2} = -\frac{V_{ox} e}{t_{ox}} + \frac{1}{4\epsilon_0} \left[\frac{e^2}{r_0^2 + z_p^2(t)} \right] - \left(\frac{\epsilon_s - \epsilon_o}{\epsilon_s \epsilon_o} \right) \int_0^t \omega^2(t-t') e^{-\omega(t-t')} \times \left[\frac{e^2}{[z_p(t) + z_p(t')]^2 + 4r_0^2} \right] dt'. \quad (5)$$

We have included here a softening factor r_0 in the image force term in order to avoid the singularity at $z_p=0$. The differential equation is run until the critical velocity v_c , and hence critical kinetic energy ($E_c=1/2mv_c^2$) is determined for the particle to just cross the barrier. The results are demonstrated in Fig. 4. In the calculation we use an electron mass $m=1$, in agreement with some recent findings.¹⁸ The numerical results, again plotted against $V^{1/2}$, exhibit a nearly linear behavior, in good agreement with the classical image force theory. The slope of the fit to the numerical data is equivalent to $\epsilon_{ox}=2.69$. This value is in very good agreement with the value 2.74 extracted from the experimental data. Based on the above considerations we conclude that the electron–phonon interaction is the underlying cause for the increase of ϵ_{ox} from 2.15 to 2.69. It should be noted that in the model the upper cutoff frequency of 0.153 eV for the optical phonon mode was used. Both acoustic phonon scattering and longitudinal–optical (LO) phonon scattering occur in SiO₂, however, they depend in a fundamentally different way on the electron energy.^{14,19} Since acoustic phonons have much smaller energies, they contribute little to the energy relaxation rate, but lead to strong momentum relaxation,

which increases with electron energy and favors larger angle scattering. Therefore electron scattering by acoustic phonons is not considered in our model, since when it occurs, the electron will be scattered back to the metal.¹⁰ In contrast, the more energetic LO phonons cause strong energy relaxation for electrons with energy near that of the dominant LO mode. With increasing electron energy LO phonon scattering rates rapidly decrease due to the polar nature of the electron-phonon interaction, and the scattering becomes increasingly forward oriented. There are two dominant LO phonon modes in SiO₂, with energies of 0.063 and 0.153 eV, that correspond to two resonances in the dielectric response.⁹ Since the electron-LO phonon interaction occurs only if the electron energy is comparable with that of the phonon modes,¹⁹ we can speculate that electron-phonon interaction may only happen when the electron approaches the barrier maximum with an energy ≤ 0.2 eV. This notion is consistent with the observation that electrons at different oxide biases (leading to different "transit time" to the barrier maximum) experience the same scattering rates, as manifested by the field independent dielectric constant ϵ_{ox} .

IV. FINAL REMARKS AND CONCLUSIONS

The response of a polarizable medium to a moving charge is a fundamental phenomenon in condensed matter physics. The classical model presented in this article was set up to describe a system governed by quantum effects. Nevertheless, the results of an effective image force dielectric constant lying in between the static and the optical are intuitively physical and in agreement with our experimental results. The reason for the different values of ϵ_{ox} obtained from different experimental methods is largely due to the improved sensitivity of BEEM to detect the low energy electrons that barely surmount the barrier. However it should be noted that a quantum mechanical treatment may be required for the real system. Provided the velocity of the particle exceeds a certain limit, electrons on the metal surface are not able to follow the time varying field of the moving particle; in effect, the metal/dielectric interface can no longer be treated just by introducing the image of the particle.^{20,21} The concept of transit time is not valid either. Since the time scale of the moving particle is so short (10^{-15} s), the uncertainty principle no longer allows us to describe the particle with a certain velocity at a certain time. Therefore the classical treatment using trajectories to describe a particle's motion needs to be replaced by quantum mechanic solutions. In addition, the quantum mechanic polaron cloud surrounding the propagating particle, which modifies the particle's self-

energy, may need to be considered as well. The latter issue appears to be an important consideration for low electric fields, for which the barrier maximum lies deep within the oxide.

In conclusion, the article presents field induced barrier lowering observed with the BEEM technique. Calculations based on the WKB approximation exclude an electron tunneling contribution to the observed threshold shifts. For the Pd/SiO₂ interface, a flat band threshold of (4.08 ± 0.02) eV was deduced. A new value of 2.74 for the image force dielectric constant was obtained, which is supported by a classical model of the retarded image force. As a consequence, a deeper understanding of the dielectric response of a polarizable medium to a moving charge was achieved.

ACKNOWLEDGMENTS

The authors benefited from the technical assistance of M. Prikas. This research was supported by the Office of Naval Research under Contract No. N00014-95-C-0087.

- ¹S. M. Sze, *Physics of Semiconductor Devices*, 2nd ed. (Wiley, New York, 1981).
- ²Z. A. Weinberg, *J. Appl. Phys.* **53**, 5052 (1982).
- ³Z. A. Weinberg and A. Hartstein, *Solid State Commun.* **20**, 179 (1976).
- ⁴S. M. Sze, C. R. Crowell, and D. Kahng, *J. Appl. Phys.* **35**, 2534 (1964).
- ⁵R. J. Powell, *J. Appl. Phys.* **41**, 2424 (1970).
- ⁶P. M. Solomon and D. J. DiMaria, *J. Appl. Phys.* **52**, 5867 (1981).
- ⁷E. H. Nicollian and J. R. Brews, *MOS Physics and Technology* (Wiley, New York, 1982).
- ⁸M. V. Fischetti and S. E. Laux, *J. Appl. Phys.* **78**, 1058 (1995).
- ⁹*Handbook of Optical Constants of Solids*, edited by E. D. Palik (Academic, Orlando, 1985), p. 753.
- ¹⁰R. Ludeke, A. Bauer, and E. Cartier, *Appl. Phys. Lett.* **66**, 730 (1995); *J. Vac. Sci. Technol. B* **13**, 1830 (1995).
- ¹¹M. Prietsch, A. Samsavar, and R. Ludeke, *Phys. Rev. B* **43**, 11850 (1991).
- ¹²R. Ludeke, E. Cartier, and H. J. Wen, *J. Electrochem. Soc.* **96-1**, 580 (1996).
- ¹³R. Ludeke, H. J. Wen, and E. Cartier, *J. Vac. Sci. Technol. B* **14**, 2855 (1996).
- ¹⁴E. Cartier, D. Arnold, D. J. DiMaria, M. V. Fischetti, P. Braunlich, S. C. Jones, X. A. Shen, R. T. Casper, and P. J. Kelly, *Rev. Solid State Sci.* **5**, 531 (1991).
- ¹⁵C. A. Mead, E. H. Snow, and B. E. Deal, *Appl. Phys. Lett.* **9**, 53 (1966).
- ¹⁶M. V. Fischetti, S. E. Laux, and E. Crabb, *J. Appl. Phys.* **78**, 1058 (1995).
- ¹⁷J. D. Jackson, *Classical Electrodynamics* (Wiley, New York, 1962).
- ¹⁸S. Zafar, K. A. Konrad, Q. Liu, E. A. Irene, G. Hames, R. Kuehn, and J. J. Wartman, *Appl. Phys. Lett.* **67**, 1031 (1995).
- ¹⁹D. Arnold, E. Cartier, and D. J. DiMaria, *Phys. Rev. B* **49**, 10278 (1994).
- ²⁰J. Heinrichs, *Phys. Rev. B* **8**, 1346 (1973).
- ²¹G. D. Mahan, in *Collective Properties of Physical Systems, Proceedings of the Nobel Symposium XXIV*, edited by B. I. Lundqvist and S. Lundqvist (Academic, New York, 1974).

8/12/97

*Submitted
to PRL*

Dielectric Response in Electron Transport across Metal-Oxide-Semiconductor Structures

H.J. Wen, D. M. Newns and R. Ludeke

IBM T.J. Watson Research Center,
P.O. Box 218, Yorktown Heights NY, 10598

(Received: Dec xx, 1996)

The oxide-field dependent threshold shifts for STM injected electrons into MOS structures follow classical image force theory, and yield a dielectric constant intermediate between the optical and static values. A theory based on the classical equation of motion for an electron in the retarded phonon field gives results close to these experimental findings. We conclude that optical phonons play a significant role in defining the potential seen by electrons in SiO₂.

Pacs numbers: 73.40.-c, 73.40.Qv, 73.50.Fq, 77.22.Ch

The response of a polarizable medium to a moving charge has been a fundamental issue for many years [1-8], and one of considerable practical relevance for electron transport in solid state devices, such as metal-oxide-semiconductor (MOS) and metal-semiconductor structures [9-16]. The issue of relevance here is the dielectric response, expressed through an effective dielectric constant ϵ_{im} , that determines the strength and shape of the potential sensed by an electron on the dielectric side of a metal-oxide interface. Past studies have concluded that ϵ_{im} is given by the high frequency or optical dielectric constant $\epsilon_{op} \sim 2.15$ of the oxide (SiO_2) in the MOS structure [9-12], a conclusion that we challenge on experimental and theoretical grounds in this letter. Our observations are based on the direct measurement of the electric field dependent minimum energy (threshold) needed for an electron to surmount the potential barrier of the MOS device. This novel approach allows for a direct evaluation of ϵ_{im} and sets the framework for a theoretical assessment of its magnitude without the difficulty of solving transport equations.

Changes in the response of a medium to a potential varying in a time interval τ shorter than a characteristic response frequency are referred to as dynamic effects [1,2]. Such effects are manifested by a reduced screening of charge moving outside a metal surface that results when $1/\tau$ exceeds the collective response of the metal electrons [4,5,6]. The latter is described by the surface plasmon, whose energy $\hbar\omega_s$ is of order of several eV.

A different and rarely studied type of dynamic response ensues when the vacuum is replaced by a polarizable medium [8], whose dielectric response is largely governed by optical phonons of energies of order of 100 meV. This case is of relevance to transport dynamics of low energy electrons injected into the conduction band of SiO_2 of a MOS structure. Within classical image force theory the screening of the combined metal-oxide system is represented by the potential $V_{im}(x) = -q/(16\pi\epsilon_0\epsilon_{im}x)$, where q is the electron charge, x the distance from the metal surface and ϵ_0 the permittivity of vacuum. Exchange and correlation effects in a full quantum mechanical treatment remove the singularity at

$x=0$, a feature consistent with experiment [17], with the solution approaching the classical form a few Bohr radii from the interface [18]. ϵ_{im} is a function of a time dependent perturbation arising from the electron traversing the interface region, and deviations from its high frequency optical limit are due to the electron's ability to partially polarize the SiO_2 lattice. It is to be expected that ϵ_{im} is dependent on the methods of both electron injection and detecting the electrons that reach the Si. Our approach of measuring transmission thresholds uniquely establishes critical velocities of a go/no-go transmission process over the potential barrier that we model in a classical framework by solving the retarded Newton's equation. Its numerical solution yields an $\epsilon_{im}=2.69$.

The system of concern here is a metal-oxide-semiconductor (MOS) structure comprised of a Pd film, a SiO_2 layer of thickness t_{ox} and a Si substrate. The application of a voltage V_{ox} across the metal and silicon allows the combined image and field potential, given by $V(x) = V_{im}(x) - xV_{ox}/t_{ox}$, to modify the potential barrier between the metal and the SiO_2 conduction band minimum, as shown in Fig. 1. The maximum V_o of the potential decreases by δV_o with increasing V_{ox} and its position x_m moves closer to the interface:

$$\delta V_o = (qV_{ox}/4\pi\epsilon_{im}\epsilon_o t_{ox})^{1/2} \quad \text{V}; \quad x_m = (qt_{ox}/16\pi\epsilon_{im}\epsilon_o V_{ox})^{1/2} \quad \text{m}. \quad (1a,b)$$

The field dependent threshold potential is defined as $V_{th}=V_o-\delta V_o$. Since x_m is of order of a nm, injected electrons with energy close to eV_{th} (measured relative to the Fermi level E_F of the metal) will reach x_m in a time scale shorter than $1/\omega_{ph}$. From estimates of this time scale or transit time $\tau \sim x_m/\bar{v}_{el}$, where \bar{v}_{el} is an average electron velocity in the region of the image force ($5-10 \times 10^7$ cm/sec), it has been argued that the electron moves so fast that the lattice polarization cannot respond. Consequently, such energetic electron is screened only by the valence electrons of the SiO_2 , as reflected through ϵ_{op} [11]. An accurate and direct determination of the field dependence of V_o can be used to test this argument, as the image potential maximum acts as a high pass spectrometer in close, but variable proximity to the metal- SiO_2 interface. Here we use Ballistic Electron Emission

Spectroscopy (BEES) to determine V_{th} directly and from its field dependence we obtain a dynamic dielectric response $\epsilon_{im}=2.74\pm0.11$ for SiO_2 . This value lies between the static ($\epsilon_{st}=3.9$) and optical ($\epsilon_{op}\sim 2$) limits and differs considerably from earlier values of 2.15 obtained by internal photoemission [9,10,12]. For lack of a better value, the latter has been used exclusively in the interpretation of transport data [13,14] and in device simulations by Monte Carlo methods [16]. The discrepancy between the two methods is largely due to the direct determination of V_{th} with BEES, which avoids the questionable curve fitting routines and extrapolations inherent to internal photoemission [11]. The latter thus determines a "threshold" corresponding to quite energetic electrons that sense a dielectric response different from that encountered by the near-threshold electrons found in conventional electron injection methods.

BEES and sample preparation have been presented elsewhere and only a sketch will be given [19]. BEES is a scanning tunneling microscope (STM) based method for injecting hot electrons from a tungsten tip into the thin metal overlayer of an MOS structure. The tip bias V_T , referenced to the metal, reflects directly the energy eV_T of the injected electrons. The latter traverse the metal ballistically and may enter the conduction band of the SiO_2 for $V_T > V_{th}$ (Fig. 1). Under the positive bias shown most of the electrons that have surmounted the barrier will be collected in the Si substrate as a collector current I_C . Thus a spectrum of V_T vs I_C will show a threshold near $V_T = V_{th}$ beyond which I_C rises. The MOS samples were fabricated from rectangular pieces of thermally oxidized Si(100) (phosphorus-doped to the mid 10^{16} cm^{-3}), with $t_{ox} = 7.5 \text{ nm}$, onto which $0.2 \text{ mm } \phi$, 3.5 nm thick Pd dots were evaporated in Ultra High Vacuum (UHV) and subsequently transferred in UHV to the STM chamber. Typically 16-25 BEEM spectra were measured for each bias voltage V_b , from which V_{ox} was calculated [13,19]. After a change in V_b , spectral acquisition was delayed by several minutes to allow minority carriers to reach equilibrium. Some 5-12 spectra, each exhibiting the same low threshold within a set, were averaged to improve statistics. The remaining spectra had thresholds that were larger by up to se-

veral tenth of an eV, shifts that are attributed to electrons locally trapped during data acquisition [20].

Representative spectra for $V_b > 0$ and $I_T = 2 \text{ nA}$ are shown in the inset of Fig. 2. As the oxide bias V_b increases the spectra intensify and shift to lower energy. The thresholds V_{th} were obtained with an accuracy of $\pm 0.02 \text{ V}$ by fitting a calculated expression, based on non-conservation of transverse momentum [21], to the data in the vicinity of the threshold region. The positions of the thresholds are marked by short vertical lines in the inset of Fig. 1, and their values are plotted in Fig. 2 as a function of $V_{ox}^{1/2}$. A least squares fit through the data indicates a high degree of linearity that agrees with the prediction of classical image theory. A fit with eq. (1a) overlaps the least squares fit to the data for $\epsilon_{im} = 2.74 \pm 0.11$. From the zero field intercept we deduce that the Pd/SiO₂ barrier height is $4.08 \pm 0.02 \text{ eV}$. Contributions to I_C from electrons tunneling through the top of the barrier have been considered, but both WKB modeling [22] and Monte Carlo simulations [16] indicate that such contributions can be neglected here.

In order to understand the underlying physics of the experimental observations we develop next a theory based on the classical equation of motion for an electron in the retarded phonon field. The electron is treated as a classical particle with trajectory \vec{x}_e . We calculate its potential $V(\vec{x}, t)$ and from it the force acting on the particle at $\vec{x} = \vec{x}_e$. We assume a uniform dielectric medium with a local dielectric response. The metal-dielectric interface at $x=0$ is represented through the image potential of the particle. We start with the well known formula [23]:

$$V(\vec{x}, t) = V^0(\vec{x}, t) + \frac{1}{4\pi\epsilon_0} \int d^3x' \vec{P}(\vec{x}', t) \nabla_{x'} (1/|\vec{x} - \vec{x}'|) , \quad (2)$$

where V^o is the external potential due to the particle and image, switched on at $t=0$. The induced polarization \vec{P} is defined through the local polarizability α :

$\vec{P}(\vec{x},t) = -\epsilon_0 \int_0^t \alpha(t-t') \nabla V(\vec{x},t') dt'$. Eq. (2) is solved by using Green's theorem and taking the Laplace transform, giving $\bar{V}(x,p) = \bar{V}^o/[1 + \bar{\alpha}(p)]$. $\bar{\alpha} = \bar{\alpha}_{op} + \bar{\alpha}_{ph}$ is the sum of the optical response, independent of p , and the phonon response $\bar{\alpha}_{ph} = g\omega_{ph}^{o,2}/(p^2 + \omega_{ph}^{o,2})$, where g is the phonon coupling strength and ω_{ph}^o a bare phonon frequency. Through the frequency dependent dielectric function $\epsilon(p) = \epsilon_{op} + \bar{\alpha}_{ph}$, it can readily be shown that $g = \epsilon_{st} - \epsilon_{op}$. After suitable substitutions and inverse Laplace transformations, one obtains the expression in terms of the renormalized phonon frequency $\omega_{ph} = \omega_{ph}^o(\epsilon_{st}/\epsilon_{op})^{1/2}$:

$$V(x,t) = \frac{V^o(x,t)}{\epsilon_{op}} - \frac{(\epsilon_{st} - \epsilon_{op})}{\epsilon_{st}\epsilon_{op}} \int_0^t \omega_{ph} \sin[\omega_{ph}(t-t')] V^o(x,t') dt' . \quad (3)$$

V^o has contributions from the image term $V_{im}^o \propto q/[x + x_e(t)]$ and a self energy term $V_{se}^o \propto -q/[x - x_e(t)]$. $x_e(t)$ represents the particle coordinate. V_{se} leads to the polaron cloud surrounding the particle, a quantum mechanical concept that we neglect in our present classical treatment. It should be noted that the phonon contributions to the potential are now explicitly represented by the integral term in eq. (3). The equation of motion $m\ddot{x}_e = \text{Force}(x_e)$ is obtained by differentiating $V(x,t)$ w.r.t. x , and setting x to x_e :

$$m \frac{d^2 x_e}{dt^2} = \frac{V_{ox}q}{t_{ox}} - \frac{q^2}{16\pi\epsilon_0\epsilon_{op}[x_e^2(t) + r_o^2]} + \frac{(\epsilon_{st} - \epsilon_{op})}{4\pi\epsilon_0\epsilon_{st}\epsilon_{op}} \int_0^t \frac{q^2 \omega_{ph} \sin[\omega_{ph}(t-t')]}{[x_e(t) + x_e(t')]^2 + 4r_o^2} dt' . \quad (4)$$

We have included a softening factor r_o for the image force to avoid its divergence at $x=0$. Its value $r_o=1.33$ a.u. was chosen so that the peak in $V(x,t)$ relative to the Fermi level in the metal equals V_o (≈ 4 V). A further refinement was the replacement of the single Einstein mode at ω_{ph} by a phonon spectrum $\propto \omega/(\omega^2 + \omega_c^2)^2$, whereupon the factor

$\omega_{ph} \sin(\omega_{ph}t)$ becomes $f(t) = \omega_c^2 t e^{-\omega_c t}$; here ω_c is defined by the upper phonon cutoff frequency of 153 meV in SiO₂ [24]. We solve eq.(4) for x_e as a function of time, with the initial velocity of the particle as it enters the oxide as the boundary condition. For a given value of the external field, the initial velocity is then varied so as to find the critical velocity to get a trajectory which just makes it over the barrier. This leads to the energy plotted as the ordinate in Fig. 3. Two masses, $m = m_{el}$ and $m = 0.5m_{el}$ (m_{el} is the electron mass), were used, with the results shown in Fig. 3. The numerical solutions lie close to a straight line when plotted against $V_{ox}^{1/2}$. From the slope in the case $m = m_{el}$, which is close to the SiO₂ conduction band mass [25], an image dielectric constant $\epsilon_{im}=2.69$ was obtained, in very close agreement with the experimental value.

The measured and calculated value for $\epsilon_{im}\approx2.7$ is incompatible, as mentioned earlier, with the transit time argument. Over the applied range of V_{ox} the variations in V_{th} are relatively small (3.5-4 V), whereas x_m varies from ~0.4-2.2 nm. Consequently, \bar{v}_{el} can be treated as nearly constant. For a value $\bar{v}_{el} \sim 8 \times 10^7$ cm/sec, based on half of the injection energy, the range of the transit time τ corresponds to an equivalent impulse of $10\omega_{ph}$ - $50\omega_{ph}$, a range that is clearly in the optical response range of SiO₂ ($\epsilon_{ox}\sim2$). The critical issue in this letter is not only the intermediate value of ϵ_{im} , but also the experimental finding and theoretical corroboration that ϵ_{im} is essentially constant over the range of applied V_{ox} . This property is again attributed to the relative independence of \bar{v}_{el} on V_{ox} , since for short transit times the integral term of eq. (4), which is responsible for the deviation of ϵ_{im} from the optical value and represents the average force exerted by the phonons on the electron, can be simplified to be $\propto \omega_{ph}^2 / \bar{v}_{el}^2$. Our numerical solutions (not shown) further show that the average force is constant, that is, it is independent of the oxide field and the value of x_m . Consequently, a new concept is advanced that the dielectric response depends on the nearly field independent mean velocity of the electron, rather than the transit time. For fields beyond the range of the experiment we expect deviations from the observed linearity, a tendency already suggested by the calculated points in Fig. 3.

In summary, we have observed a strong field effect in the threshold of STM mediated current injection into MOS structures. The observed behavior is attributed to image force effects, with negligible contributions from electrons tunneling through the barrier. The value of the associated image force dielectric constant, intermediate between optic and static limits, indicates that phonon contributions cannot be neglected. A classical response model supports this interpretation and, moreover, yields a value of ϵ_{im} in close agreement with experiment.

Acknowledgements. Fruitful discussions with Frank Stern, Peter Price, Norton Lang and Paul Marcus are gratefully acknowledged. This research was partly supported by the Office of Naval Research under contract N00014-95-C-0087.

References

- [1] J. Heinrichs, Phys. Rev. B **8**, 1346 (1973).
- [2] G.D. Mahan, in *Collective Properties of Physical Systems*, Nobel Symposium XXIV, B. I. Lundqvist and S. Lundqvist, Eds. (Academic Press, NY, 1974).
- [3] H. Raether *Excitations of Plasmons and Interband Transitions by Electrons*, Springer Tracts in Modern Physics, Vol. **88** (Springer Verlag, Berlin, 1980).
- [4] D. L. Haavig and R. Reifenberger, Phys. Rev. B **26**, 6408 (1982).
- [5] P. Guéret, E. Marclay and H. Meier, Appl. Phys. Lett. **53**, 1617 (1988) and Solid State Commun. **68**, 977 (1988).
- [6] B.G.R. Rudberg and M. Jonson, Phys. Rev. B **43**, 9358 (1991).
- [7] J. L. Farvacque and Z. Bougrioua, Semicond. Sci. Technol. **9**, 1324 (1994)
- [8] C. Auth, T. Hecht, T. Igel and H. Winter, Phys. Rev. Lett. **26**, 5244 (1995).
- [9] C. A. Mead, E. H. Snow and B. E. Deal, Appl. Phys. Lett. **9**, 53 (1966).
- [10] R. J. Powell, J. Appl. Phys. **41**, 2424 (1970).
- [11] C. N. Berglund and R. J. Powell, J. Appl. Phys. **42**, 573 (1971).
- [12] P. M. Solomon and D. J. DiMaria, J. Appl. Phys. **52**, 5867 (1981).
- [13] E. H. Nicollian and J. R. Brews, *MOS Physics and Technology* (John Wiley, NY, 1982) and references therein.
- [14] T. H. Ning, C. M. Osburn and H. N. Yu, J. Appl. Phys. **48**, 286 (1977).
- [15] S. M. Sze, *Physics of Semiconductor Devices* (John Wiley, NY, 1981) 2nd edition.
- [16] M. V. Fischetti, S. E. Laux and E. Crabbé, J. Appl. Phys. **78**, 1058 (1995).
- [17] G. Binnig, N. Garcia, H. Rohrer, J. M. Soler and F. Flores, Phys. Rev. B **30** 4816 (1984).
- [18] P. A. Serena, J. M. Soler and N. Garcia. Phys. Rev. B **34**, 6767 (1986).

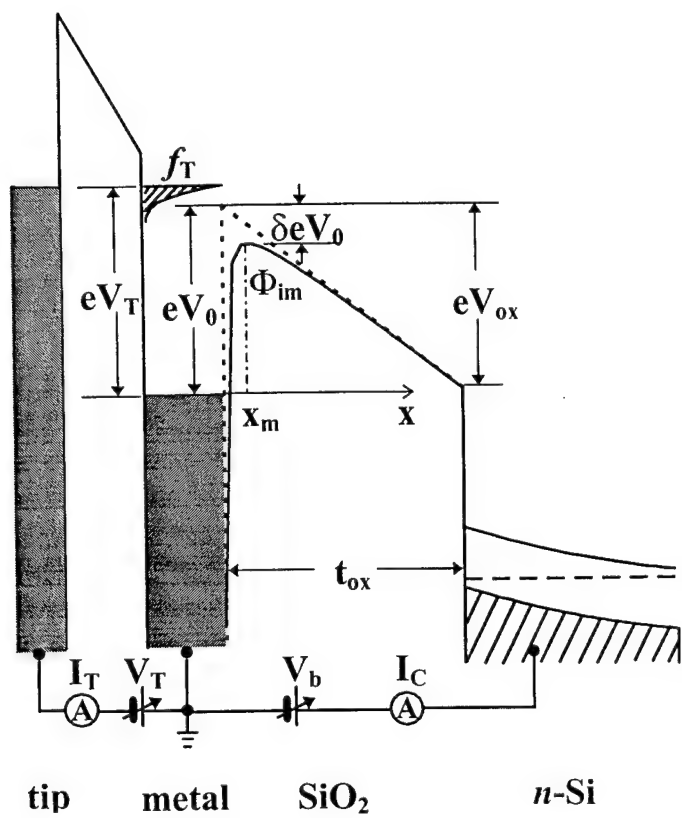
- [19] R. Ludeke, H.J. Wen and E. Cartier, J. Vac. Sci. Technol. **B 14**, 2855 (1996); R. Ludeke, A. Bauer and E. Cartier, J. Vac. Sci. Technol. **B 13**, 1830 (1995).
- [20] H. J. Wen and R. Ludeke, J. Vac. Sci. Technol. **B 15**, July/August (1997).
- [21] R. Ludeke and A. Bauer, Phys. Rev. Lett. **71**, 1760 (1993).
- [22] H.J. Wen, R. Ludeke, D. M. Newns and S. H. Lo, J. Vac. Sci. Technol.,**A 15** May/June (1997).
- [23] J. D. Jackson *Classical Electrodynamics* (J. Wiley, N.Y. 1962).
- [24] W. G. Spitzer and D. A. Kleinman, Phys. Rev. **121**, 1324 (1961).
- [25] S. Zafar, K. A. Conrad, Q. Liu, E. A. Irene, G Hames, R. Kuehn and J.J. Wortman, Appl. Phys. Lett. **67**, 1031 (1995).

Figure Captions

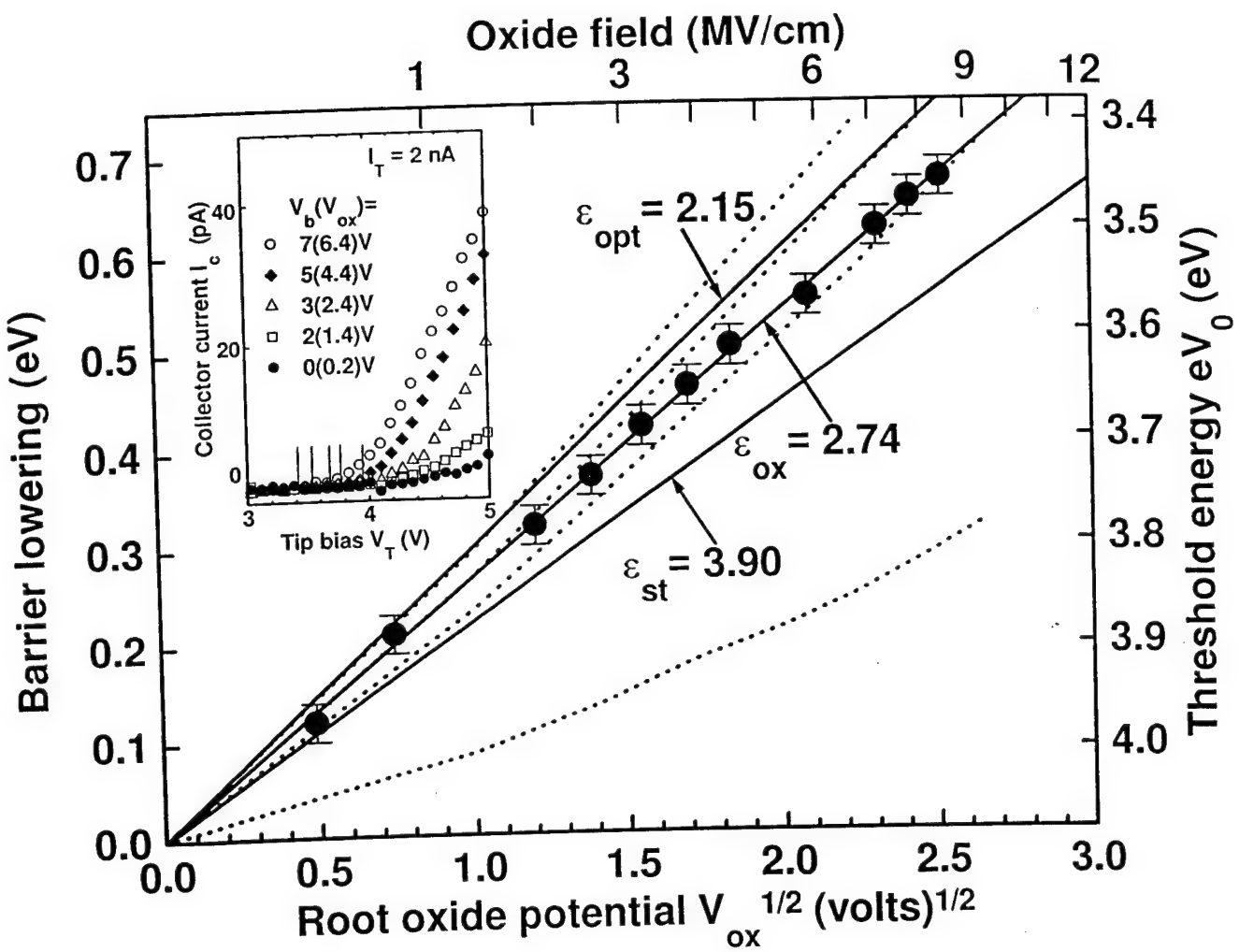
Fig. 1. Schematic energy diagram of a BEEM experiment on an MOS structure under positive oxide bias V_{ox} . The triangular, dotted potential represents the barrier in the absence of image force effects. The threshold energy (potential barrier height) is given by $eV_{th}=eV_o-e\delta V_o$.

Fig. 2. Observed threshold shifts (\bullet) obtained from fits to BEEM data (subset shown in inset) and calculated from eq. (1) (solid lines) for indicated ϵ_{ox} . The dotted lines represent calculated thresholds, via WKB, that include contributions from tunneling through the barrier, with values of $\epsilon_{ox}=2.15, 2.74$ and 3.90 used for the three top curves; the lowest dotted curve does not include image force contributions (after ref. 22).

Fig. 3. Field induced barrier lowering obtained by the dielectric response model (eq. 4). The slope of the fit through the numerical results (\bullet) for the case $m = m_{el}$, corresponds to an effective $\epsilon_{im} = 2.69$. The two dotted lines correspond to the optical (upper) and static (lower) limits.

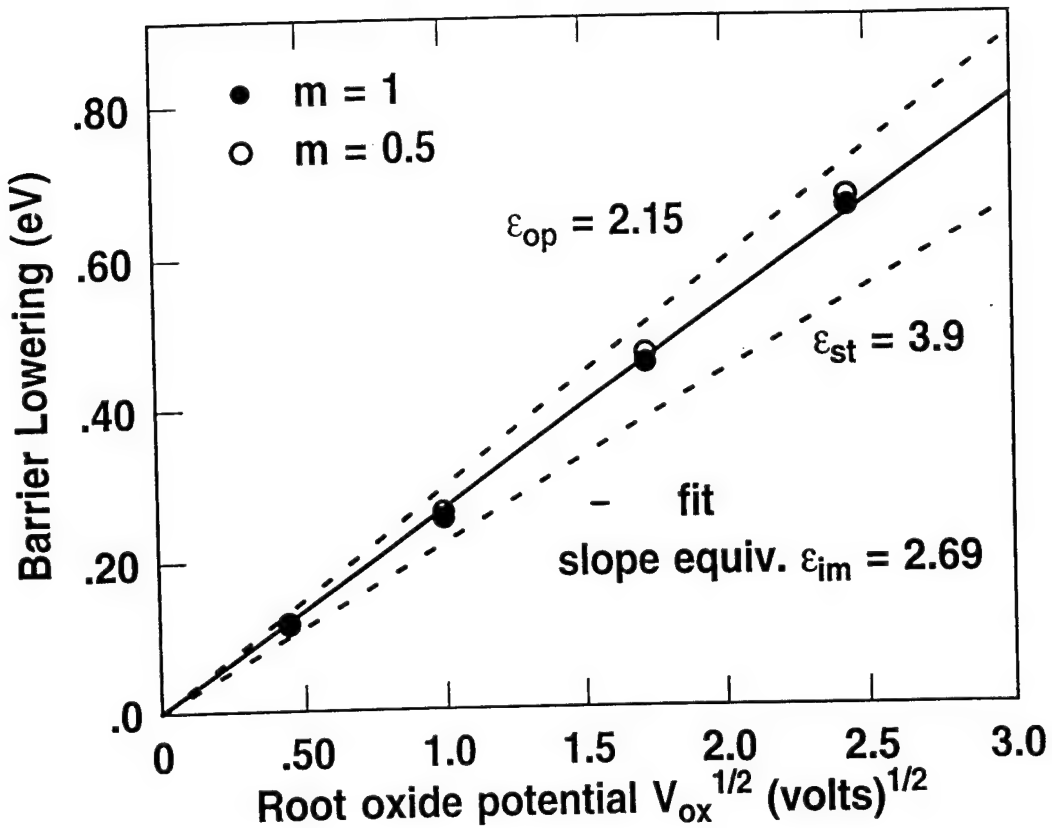


Wen et al. Fig. 1



Wen et al

Fig. 2



Reprinted from

MICROELECTRONIC ENGINEERING

An International Journal of Semiconductor Manufacturing Technology

Microelectronic Engineering 36 (1997) 255–262

Gate Oxide Characterization with Ballistic Electron Emission Microscopy

R. Ludeke and H.J. Wen

IBM T.J. Watson Research Center, P.O. Box 218 Yorktown Heights NY, 10598, USA



MICROELECTRONIC ENGINEERING

Editor (Japan)

SUSUMU NAMBA
Faculty of Engineering Science
Osaka University
Toyonaka-shi
Osaka
Japan

Editor (U.S.A.)

JOHN KELLY
Novellus Systems, Inc.
81 Vista Montana
San Jose, CA 95134
U.S.A.

Editor (Europe)

MARC VAN ROSSUM
IMEC
Kapeldreef 75
B-3001 Leuven
Belgium

Advisory Editors (Japan)

M. Komuro, *Electrotechnical Laboratory, Tsukuba*
S. Matsui, *NEC Corp., Tsukuba*
T. Nishimura, *Mitsubishi Electric Corp., Itami*
Y. Shiraki, *The University of Tokyo, Tokyo*
T. Takigawa, *Toshiba Corp., Kawasaki*
N. Yokoyama, *Fujitsu Laboratories Ltd., Atsugi*

Advisory Editors (U.S.A.)

A.R. Neureuther, *University of California, Berkeley, CA*
G. Owen, *Hewlett Packard, Palo Alto, CA*
H. Pfeiffer, *IBM, Hopewell Junction, NY*
L. Swanson, *FEI Company, Hillsborough, OR*
L.F. Thompson, *Bell Laboratories, Murray Hill, NJ*
E.D. Wolf, *Cornell University, Ithaca, NY*

Advisory Editors (Europe)

H. Ahmed, *Cambridge University, U.K.*
P. Balk, *Delft University of Technology, The Netherlands*
G. Declerck, *Interuniversitair Micro-Elektronica Centrum, Louvain, Belgium*
M. Gentili, *CNR – Istituto di Elettronica dello Stato Solido, Rome, Italy*
A. Heuberger, *Fraunhofer Abteilung für Mikrostrukturtechnik, Berlin, Germany*
M.E. Jones, *Imperial College of Science, Technology and Medicine, London, U.K.*
R.A. Lawes, *Rutherford Appleton Laboratory, Chilton, U.K.*
H.W. Lehmann, *Laboratories RCA Ltd., Zurich, Switzerland*
B. Lischke, *Siemens AG, Munich, Germany*
K.D. van der Mast, *Electron Optics, Philips, Eindhoven, The Netherlands*
V. Mifud, *Vacuum Generators Semicon Ltd., East Grinstead, U.K.*
W.C. Nixon (Founding Editor), *Cambridge University, U.K.*
J. Perrocheau, *ELISA, Les Ulis, France*
M. Pichot, *CNET, Meylan, France*
P. Vettiger, *IBM, Rüschlikon, Switzerland*
E. Wolfgang, *Siemens AG, Munich, Germany*

Aims and Scope

The aim of *Microelectronic Engineering* is to bring together in one publication, the results of European, American and Japanese work in the rapidly expanding field of integrated microelectronic, optic and optoelectronic devices. *Microelectronic Engineering* is an archival, peer-reviewed journal. It publishes full research papers, short communications, and review articles. The scope of this Journal includes materials, methods and designs for microfabrication, processing and inspection for microelectronic and optoelectronic elements from centimeters to nanometers.

The wide range of topics covered by the journal include:

1. *Lithography*
 - optical lithography (submicron dimensions, deep u.v. lithography)
 - electron optical methods and systems
 - ion beam methods and systems
 - X-ray optical methods and systems
 - resists
2. *Pattern Transfer*
 - ion implantation
 - dry etching
3. *Materials*
 - metallization
 - microstructuring growth processes
 - silicon on insulators
4. *Inspection and Testing*
 - electron beam testers
 - laser probes
 - signal and image processing
 - metrology
5. *Advanced Processing*
 - process integration
 - three dimensional integration
 - defect free processes
 - manufacturing science
 - rapid thermal processing
 - process modelling
 - equipment modelling
 - laser assisted processing
6. *Fabrication Aspects of Micromechanical Structures*
7. *Advanced Devices*
 - nanometer structures
 - dimension-sensitive devices properties
 - effect of small dimensions



ELSEVIER

Microelectronic Engineering 36 (1997) 255–262

MICROELECTRONIC
ENGINEERING

Gate Oxide Characterization with Ballistic Electron Emission Microscopy

R. Ludeke and H.J. Wen

IBM T.J. Watson Research Center, P.O. Box 218 Yorktown Heights NY, 10598, USA

Ballistic Electron Emission Microscopy (BEEM) is shown to be a versatile new tool for the study of hot electron phenomena in metal-oxide-semiconductor structures. The elusive problem of measuring oxide charge distributions is largely overcome by suitable modeling of the field dependent threshold shifts for both pre-existing defects and stress induced traps. Local oxide breakdowns were seldom observed, and then only after injecting charge dosages that exceeded by several orders of magnitude the best values reported on macroscopic samples.

1. INTRODUCTION

Virtually all knowledge of the electrical properties of dielectrics has been garnered from mostly traditional current-voltage or capacitance-voltage measurements made on metal-oxide-metal or metal-oxide-semiconductor (MOS) sandwich structures. A microscopic picture of the fundamental processes governing the electrical properties on an atomic scale was consequently deduced from such averaging measurements on macroscopic samples. However, with the relentlessly ongoing reduction of device dimensions, local fluctuations in material properties become increasingly dominant, and properties representing averages over macroscopic dimensions become less relevant at predicting device performance and reliability. Consequently, there exists a need to investigate material issues of thin SiO₂/Si layers on a microscopic scale.

The advent of the Scanning Tunneling Microscope (STM) provided the first practical means of investigating electrical phenomena on solid surfaces with resolution of atomic dimensions. Yet its application to the investigation of sub-surface phenomena required another instrumental advance of the STM, namely that of the Ballistic Electron Emission Microscope (BEEM) in 1988 [1]. Primarily used to study transport phenomena in Schottky barriers, the first BEEM applications on MOS structures were reported for Au-CaF₂-Si in 1994 [2], and for Pt-SiO₂-Si in the following year [3]. The use of an Atomic Force Microscope (AFM) to investigate transport through thin SiO₂ layers has recently been reported [4-6]. Whereas the AFM studies were performed directly on the oxide using a conducting cantilever/stylus, BEEM requires a conducting overlayer to which the STM tip bias is referenced. This conveniently allows an arbitrary choice of the energy of the electrons injected by the

STM tip into the MOS structure. BEEM has several additional advantages besides its unsurpassed spatial resolution, these include: a) a relatively narrow energy distribution (<0.3 eV) of injected electrons, b) independence on oxide thickness, with successful BEEM experiment reported on 25 nm oxide layers [7], and c) independent control over the injection energy and oxide bias, which thereby increases the accessible energy range and enhances experimental flexibility. In contrast, the traditional Fowler-Nordheim (F-N) and photo-injection methods depend solely on the high oxide fields to accelerate the injected electrons to suitable energies, but at a cost of a position dependent kinetic energy distribution of the electrons that complicates the determinations of energy dependent properties [8]. This method of achieving hot electrons becomes increasingly difficult for oxide thicknesses $t_{ox} < 100 \text{ \AA}$, the thickness regime for future VLSI applications.

BEEM has been successfully used on MOS structures to determine the energy and thickness dependent electron transmission probabilities in oxides [3], to visualize and quantify stress induced trapped charge [7,9], and to measure the dynamic dielectric response of SiO₂ from the field dependent image force lowering of thresholds [10]. Here we will describe the salient results of recent BEEM studies of hot electron transport through thin SiO₂ layers, with particular emphasis on the generation of trap states in the oxide and related stress studies that lead to the eventual breakdown of the oxide.

2. EXPERIMENTAL DETAILS

2.1 Ballistic Electron Emission Microscopy

The implementation of BEEM differs from that of the conventional STM by the presence of a thin conducting layer, usually a metal, deposited on top

of the semiconductor structure to be measured. The metal establishes a ground contact relative to which both the STM tip bias V_T and the oxide bias V_{ox} are referenced. The tip bias thereby establishes the energy eV_T of the electrons injected into the metal surface. A cartoon of this implementation is shown in Fig. 1a. For metal film thicknesses comparable or less than the electron mean free path, most of the electrons will traverse the metal ballistically to reach the far interface. If the electrons encounter a potential barrier at that interface, they will backscatter unless their energy exceeds that of the barrier. In this case a fraction of the electrons will reach the semiconductor, from where they emerge as a collector current I_c . Besides the conventional topography mode of the STM, the collector current I_c can also be used to provide contrast for a second, simultaneously recorded image (the BEEM image) that represents the local transmission characteristics of the semiconductor structure. In the spectroscopy mode of BEEM the STM image acquisition is interrupted at a predetermined location on the surface and I_c is measured as V_T is swept over a voltage range that includes the barrier potential maximum. Thus initially I_c is zero until V_T exceeds a threshold value V_o that represent the effective barrier potential of the device structure. V_o can be measured to an accuracy of ± 0.02 V [3,9].

The energy diagram for a BEEM experiment on a MOS structure is shown in Fig. 1b for zero oxide bias and near "flat-band" conditions that apply for a p-type Si substrate and a Pd gate [9]. The curved leading edge of the oxide barrier results from the inclusion of image force lowering [10]. The condition for injection into the conduction band of the SiO_2 is shown ($V_T > V_o$). The threshold for injection, V_o , is about 4 V. A maximum tip bias of $V_T=13$ V can be achieved with our STM. The corresponding kinetic energy E_{kin} relative to the SiO_2 conduction band minimum is ~ 9 eV for the hottest carriers in the vicinity of the metal- SiO_2 interface. The application of an oxide field modifies the electron energies further as they move across the oxide. In comparison, the achievement of comparable energies by F-N injection into a 5 nm oxide requires an electric field of 18 MV/cm, a virtually unattainable condition. The inclusion of both an accelerating field (Si substrate positive relative to the metal), supplied by the bias potential V_b , and the presence of a negative oxide charge is illustrated in Fig. 1c. The resulting potential is divided between band bending in the Si (shown here in the accumulation condition) and the potential V_{ox} across the oxide [3].

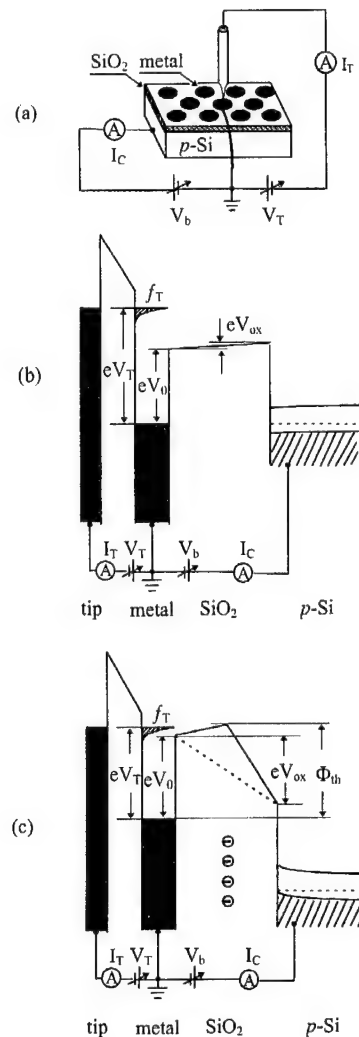


Fig. 1. Schematic of a BEEM experiment on an MOS structure. (a): layout, showing electrical connections. Energy band structure for (b): $V_b=0$, and (c): for $V_b>0$ and a negative oxide charge.

2.2 Sample Preparation

Oxide thicknesses for the studies reported here ranged from 3.8 to 7.5 nm. The device-grade SiO_2 layers were thermally grown near 800 °C in dry oxygen on 125 mm Si(100) wafers doped in the low 10^{17} cm^{-3} range. No additional treatments were performed after the oxidation. Working samples of $\sim 8 \times 15 \text{ mm}^2$ were cleaved from the wafers and introduced into the metal deposition chamber of our

ultra-high vacuum (UHV) BEEM/surface analysis system. Pd dots, 0.2 mm in diameter, were thermally evaporated onto the SiO_2 through a shadow mask. The substrate was held near 30 K during deposition in order to smooth the surface morphology of the thin ($\sim 35 \text{ \AA}$) Pd films. This process produced films with a nodular structure typically 80 \AA in diameter that protruded $<10 \text{ \AA}$ above the valleys, as shown in the STM topograph at the top of Fig. 2. A smooth surface morphology is needed to reduce BEEM image contrast arising from the surface topography of the metal [3], which cannot be eliminated as shown in the BEEM image at the bottom of Fig. 2. The finished sample was allowed to warm up to room temperature and was then transferred under UHV into the STM chamber.

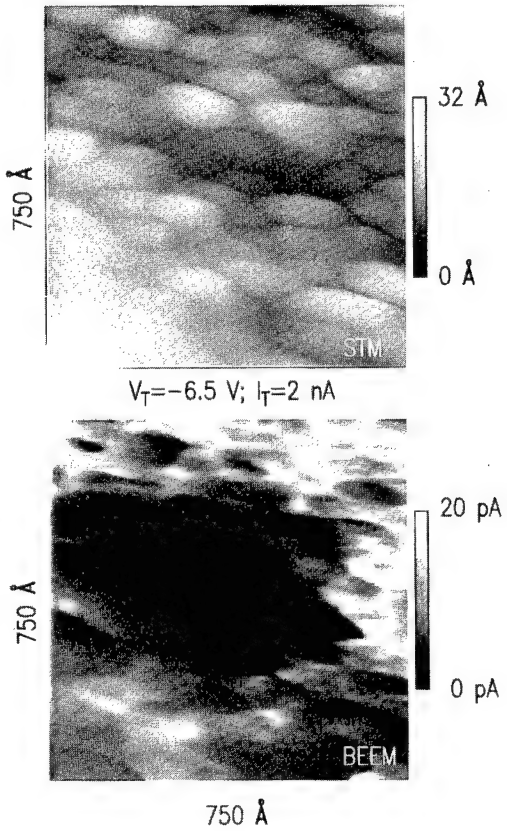


Fig. 2. STM topograph (top) and BEEM image (bottom) for a 4nm Pd/7.1 nm SiO_2 /p-Si(100) MOS structure stressed at $V_T = -10 \text{ V}$ over a $25 \times 25 \text{ nm}^2$ area that clearly appears as an $\sim 30 \text{ nm}$ oblong dark area in the BEEM image.

The grounding contact was carefully positioned onto a selected Pd dot by means of three orthogonally mounted Inchworms™. STM images and sets of BEEM spectra were then taken, the latter consisting of typically 25–36 spectra measured in a grid pattern covering a $25 \times 25 \text{ nm}^2$ area.

3. BEEM-INDUCED OXIDE CHARGES

3.1 Pre-existing defects

It was commonly observed that the thresholds in a set of BEEM spectra taken over a $25 \times 25 \text{ nm}^2$ area varied among the different spectra [3,9], which was attributed to local charging of existing defects. This interpretation was deduced from the facts that i) on a virgin area of the sample the first spectrum generally exhibited the lowest thresholds which could only be duplicated by going to another spot about 10 nm away; ii) most subsequent spectral scans at nearby locations revealed threshold increases that suggested the filling of defect sites by electrons scattered from a more distant location during a previous spectral scan; and iii) a saturation of the threshold shifts after several repeated scans at the same location, but at tip biases that kept the kinetic energies of the injected electrons below 2 eV. The saturation in particular indicates that at these low energies the electrons do not seem to generate additional trapping sites and that the charging occurs at sites already present at the time of the spectral acquisition. We have labeled these defects as pre-existing or process induced. Since we only observed threshold increases, which correspond to an increase in the oxide potential seen by the traversing electrons, we conclude that the trapped charge is due to electrons in the oxide. This situation is schematically shown in Fig. 1c.

As can readily be imagined upon inspection of Fig. 1c, an increase in the positive oxide bias will pull down (decrease) the barrier maximum at a rate that is directly proportional to the distance of the barrier maximum from the metal- SiO_2 interface. The barrier maximum corresponds approximately to the location of the centroid of the charge distribution, a fact that was used in the past to determine its value from the slope of the field dependent threshold shifts [7,11]. These determinations were made on relatively thick oxides, for which the charge distributions were far from the gate. For the thinner oxides discussed here, an appreciable part of the total charge density can reside within 2.5 nm of the interface, particularly that near the metal gate, where it is subject to image force effects. The re-

sulting potential in this region is extremely distorted, a condition that worsens with increasing positive oxide bias (accelerating fields). As a consequence the potential due to the oxide charge (other than a single sheet charge) is not uniquely described by a single centroid, with the consequence that the threshold shifts are no longer linear with applied oxide bias. This non-linearity is clearly shown in Fig. 3 for a 7.1 nm SiO₂ layer grown on a p-type Si(100) substrate. We can take advantage of the image force distorted potential to extract heretofore unavailable information on the charge distribution across the oxide. We do this after we develop a distributed sheet charge model in section 4 that incorporates image force and oxide field effects.

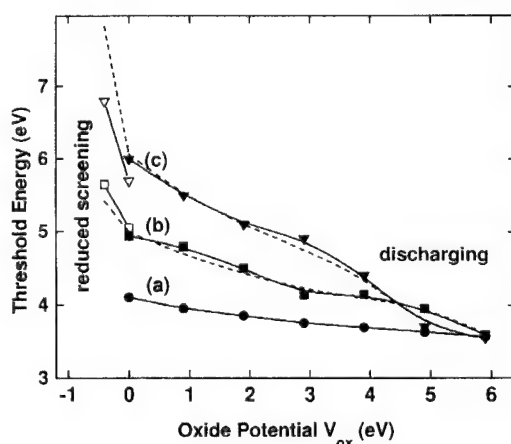


Fig. 3. Field dependent threshold shifts for a Pd/7.1 nm SiO₂/p-Si(100) sample: (a) for a charge free sample (only image force lowering); (b) for charge-saturated pre-existing defects; (c) for charge-saturated pre-existing defects and stress induced traps.

The field dependent threshold shifts for the existing defects, curve (b) in Fig. 3, was obtained in the following way. A virgin area 25×25 nm² on the MOS sample was repeatedly scanned at V_T=-6 V, I_T=2 nA and V_{ox}=0 until the thresholds, which were measured after each scan, no longer shifted, that is, the existing defects were fully saturated (the generation of additional trap at larger tip biases will be discussed in the next section). The oxide bias was then stepwise increased from 0 to 6 V, with a complete set of BEEM spectra taken over the saturated region for each bias value to determine the thresholds changes. These spanned a range of ~0.5 eV

over the 36 measured spectra for each bias value. Their distribution, essentially Gaussian over the range [9], is a measure of the statistical fluctuations of the local charge at each sampling site. In Fig. 3 we only plot the values at the peak of the distribution. The extrema of the distributions exhibit identical, but displaced behavior [9]. It is worth noting that the spread in thresholds was reproducible at other, similarly saturated regions of the sample; the spread thus represents a statistically meaningful range of fluctuations in charge density. For positive oxide potentials the thresholds shift, as expected, to lower energies. However, the shift is non-linear and even shows a tendency to saturate before exhibiting a further drop beyond V_{ox}=5 V. At 6 V the shift corresponds to that for an uncharged sample, curve (a), that is subject only to image force lowering [10]. The fact that the values nearly coincide at 6 V is an indication that the charge-saturated region has discharged. If the bias is now changed from positive to negative (open symbols) a drastic increase in the threshold occurs that is larger than the increase expected from solely changing the oxide potential (the "expected" change can be ascertained by extrapolating the slope into the negative region). We attribute this shift mainly to a change in electron screening, an issue that will be further discussed in section 4.

3.2 Stress-generated traps

We noted that when the kinetic energies of the electrons injected into the oxide exceed 2 V, pronounced threshold shifts in addition to those discussed above were observed [10]. This observation is a clear manifestation that additional charging occurs in the oxide, and moreover that it occurs at newly created trap sites. The 2 eV threshold for their creation coincides with the value for the well documented trap generation process associated with hydrogen release that is initiated through hot electron impact near the SiO₂-Si interface [12-15].

To assess the location of the generated traps through the field dependence of the spectral thresholds, we proceeded in a manner similar to that used for the existing defects. An area of 25×25 nm² was repeatedly scanned with tip biases as large as -10 V, I_T=2 nA and V_{ox}=0. Sets of spectra were analyzed after each scan to ascertain the threshold shifts. This procedure was repeated several times until the thresholds stopped shifting to higher values. The BEEM image of such a stressed area is shown as a darker, low transmission region in Fig. 2b. The area is larger than the scanned area due to the spreading of the beam as it traverses the oxide. The oxide

field dependence of the thresholds was subsequently measured. Due to the additional scattering at the trap sites the net collector current became rather weak, and the mean value in the distribution was difficult to determine. Hence we plot in Fig. 3, curve (c), only the minimum of the range of threshold shifts (the maximum tracks parallel to this curve [10]). Curve (c) is shifted higher in energy by ~ 1 eV compared to curve (b) for the pre-existing defects, a clear manifestation of the additional trapped charge in the oxide. The overall shapes of the two curves are similar, with a noticeably higher slope for curve (c), which indicates that the newly generated defects lie closer to the Si interface (a unit slope would mean that they are at the $\text{SiO}_2\text{-Si}$ interface). The steep drop that starts near 3 V and reaches the same value as the other two curves at 6 V is a clear indication of charge detrapping. Upon returning to zero oxide bias, these refill with the first spectral scan (open symbols), but do not quite reach the value for the fully saturated traps. A slight negative bias has an even more pronounced effect on the threshold shifts than for the existing traps. This shift is again attributed to the onset of screening changes, which are fully accountable by the model that will be discussed next.

Before proceeding, however, it is worthwhile to discuss the significance of the observed saturation in the threshold shifts, which indicates that the number of generated trap sites is limited as well. This ceiling in trap generation indicates that the process is non-intrinsic, that is, limited either by non-intrinsic precursors sites (some form of defect or impurity) that are activated, for the sake of argument, by the released hydrogen, or alternatively limited by the density of the hydrogen source (possibly Si-H bonds). Since for metal gate (particularly Pd) the abundance of hydrogen does not appear to be limiting, we surmise that the traps are associated with a bulk defect.

4. OXIDE-CHARGE DISTRIBUTIONS

4.1 Screened sheet charge model

The approach we take here is to model a charge region in the oxide by a series of equally spaced sheet charges, calculate the potential of each sheet charge subject to the proper boundary conditions, sum up the potentials and add the resulting defect potential to that of the oxide barrier. The latter includes both image force lowering and the applied oxide potential. We then calculate the net barrier

potential of the oxide and fit, by varying the charge density and location, the resulting field dependent maxima to the experimentally determined thresholds.

The charge injected into the oxide covers an area roughly circular with radius $R \sim 15\text{ nm}$, as shown in Fig. 2. We then represent this charge by several sheet charges of density σ_j that lie parallel both to each other and to the interfaces and are located at a distance d_j from the M-O interface. The potential $\phi_j(d_j - x)$ due to each sheet charge along the axial direction in a medium with dielectric constant ϵ_{ox} is given by [17]:

$$\phi_j(d_j - x) = \frac{\sigma_j \epsilon_{ox}}{2} \left\{ [(d_j - x)^2 + R^2]^{1/2} - |d_j - x| \right\} \quad (1)$$

The two interfaces restrain the potential to boundary conditions $\phi_j(d_j) = 0$ at the M-O interface, and $\phi_j(d_j - t) \approx 0$ at the O-S interface and for $V_{ox} > 0$. Here t is the oxide thickness. The latter boundary condition assumes that the oxide potential drives the semiconductor into accumulation, which occurs for the p-type substrates used in our studies. For $V_b < 0$ the Si at the interface is not accumulated and the potential remains finite until inversion is reached (this condition was not studied here). All these boundary conditions can be addressed by using the method of images [17]. Because of the two interfaces, the boundary conditions require multi-image charges, that is, image charges of image charges. The net potential per sheet charge is given by:

$$\begin{aligned} \Phi_j(x) = & \phi_j(d_j - x) - \phi_j(d_j + x) - \rho \phi_j(2t - d_j - x) + \\ & \rho \phi_j(2t + d_j - x) + \rho \phi_j(2t - d_j + x) - \rho \phi_j(2t + d_j + x) - \\ & \rho^2 \phi_j(4t - d_j - x) + \dots \end{aligned} \quad (2)$$

where $\rho = (\epsilon_s - \epsilon_{ox})/(\epsilon_s + \epsilon_{ox})$. Here ϵ_s is the effective dielectric constant at the Si interface, which is assumed to be large under conditions of accumulation ($V_{ox} > 0$) or equal to 11.8 otherwise. In the former case $\rho \approx 1$, in the latter $\rho = 0.49$. The first two terms in eq. 2 are the sheet charge potential and its image across the M-O interface, the remainder are the consequence of the presence of the O-S interface. These terms vanish when the interface is removed. This is formally achieved by setting $\epsilon_s = \epsilon_{ox}$, which yields $\rho = 0$.

The net potential due to a set of n sheet charges is:

$$\Phi_q(x) = \sum_{j=1}^n \Phi_j(x) \quad (3)$$

This potential is shown in Fig. 4 for two sets of 3 sheet charges, each depicted by a vertical bar: the dashed line labeled ϕ_{fs} is for $p=1$ (fully screened at the O-S interface), the dotted line marked ϕ_{ps} corresponds to $p=0.49$ (dielectric screening only). The drastic effect on the potential near the O-S interface is clearly seen as the screening is changed upon changing the carrier concentration of the Si at the interface from accumulation ($p=1$) to weak depletion ($p=0.49$).

4.2 Field dependent oxide potential and fits

The total, position dependent potential U seen by an electron injected from the gate and into the oxide is the sum of the "bare" oxide barrier V_o , the field effect V_{ox}/t , the dynamic image force lowering $q/(16\pi\epsilon x)$ [10] and Φ_q :

$$U = V_o - \frac{V_{ox}x}{t} - \frac{q}{16\pi\epsilon x} + \sum_{j=1}^n \Phi_j(x) . \quad (4)$$

This potential is shown as a function of $-0.5 \leq V_{ox} \leq 6$ V for two sets of 3 charges each that are indicated by vertical bars at the bottom of Fig. 4. Their height is proportional to the charge density, with the scale depicted on the right margin of the figure. Their strength σ_j and position d_j were chosen so as to give a reasonable fit of the field dependent maximum of U to the experimental data of Fig. 3.

The fits were done in the following way. First, σ_j and d_j were optimized for the maxima in U to fit the experimental field dependence of pre-existing defects, curve (b) in Fig. 3, using only the set of three sheet charges depicted on the left of Fig. 4 (these potential curves are not shown). The increasing σ_j 's close to the M-O interface are necessary to duplicate the observed "softening" of the slope in the experimental curve (b) as V_{ox} increases. As already discussed in section 3, the further lowering of the thresholds for $V_{ox}>4$ V is attributed to a field-induced discharge of some of the charge in the defect states. This situation is readily simulated by either setting 1 or 2 of the σ_j 's closest to the anode to zero for $V_{ox}=5$ and 6 V, respectively, or by stepwise reducing the σ_j 's equally. For $V_{ox}<0$, $p=0.49$ was used in eq. 2. The result of this modeling is shown by the dashed line overlying curve (b) in Fig. 3. Changes of order 10% in the parameters resulted in obviously inferior fits to the experimental data. Fits to the experimental results for the gener-

ated traps, curve (c) of Fig. 3, were accomplished by keeping the identical distribution and charge density of the pre-existing traps and adding another set of three sheet charges positioned close to the O-S interface, as shown by the bars in Fig. 4. We found no justification for changing their relative intensity, which was kept the same for the three components. Their strength and position, however, was crucial to fit the experimental data. Again it was important to "discharge" the σ_j 's for $V_{ox}>4$ V. For $V_{ox}>5$ V the generated traps were required to be discharged and only the pre-existing traps needed to remain partially filled for the model calculation to fit the experimental curve (c). Again, for $V_{ox}<0$ incomplete screening was assumed, with $p=0.49$.

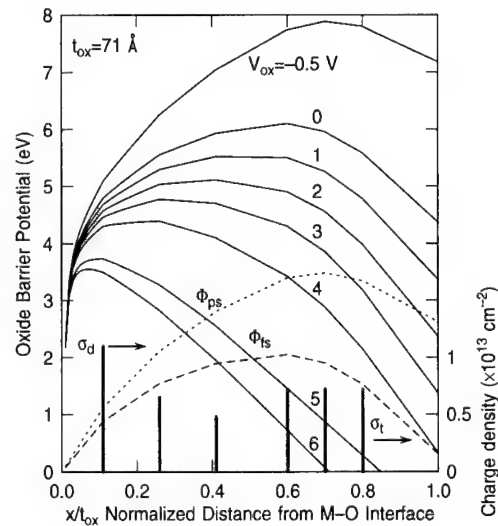


Fig. 4. Oxide-bias dependent barrier potential for the sheet charge model applied to a 7.1 nm oxide. The broken curves represent the potential only due to the charge, assuming full screening (ϕ_{fs}) and dielectric screening (ϕ_{ps}) at the $\text{SiO}_2\text{-Si}$ interface. Sheet charge location and density are marked by the six vertical bars. The density scale is on the right.

The following conclusion can be drawn from the model fits to the data. i) The pre-existing defects are close to the M-O interface and exhibit a rapidly decreasing density away from the interface. ii) The generated traps are located close, but not at the O-S interface, ($\sim 2/3$ of the distance from the M-O interface). iii) The unexpected threshold increases for negative V_{ox} can readily be explained by assuming a decrease in free carrier screening at the O-S interface, rather than a filling of interface states as

the Fermi level moves toward midgap. iv) Trap/defect discharging under high positive bias is the most plausible origin of the observed field induced decreases in the experimental thresholds.

5. BREAKDOWN STUDIES

Our studies have shown that stressing an oxide layer locally by injecting hot electrons with an STM in a BEEM experiment seldom leads to a destructive breakdown of the oxide, and when these occur, the net injected charge, often referred to as charge-to-breakdown or Q_{bd} , is orders of magnitude larger than those reported for F-N stressing on MOS capacitor structures [18]. We will present here only the salient results of these studies, for details the reader is referred to reference 18. Most of our breakdown experiments were performed on 3.8 nm oxides. In these experiments the tip of the STM is stopped at a chosen location on the surface, then V_T is set to a predetermined large value (in the range of 7-10 V) and the collector current is integrated to determine the charge injected into the oxide. The injection process is interrupted at periodic intervals to measure the threshold position. The latter increases initially and reaches a plateau, a trap generation and filling process analogous to that discussed above. If the stressing proceeds toward an eventual breakdown, the thresholds begin to decrease and an increase in the overall collector current is observed. This second stage of stressing was referred to as the pre-breakdown stage [18]. The simple view was taken that this stage commences with the collapse of the oxide barrier, an oxide thinning process that consists of the formation of regions of finite conductivity starting at the O-S interface. Additional stressing quickly led to the breakdown stage, a total collapse of the oxide barrier that resulted in a threshold of only 1 eV. The net collector current integrated to a point just prior to this oxide failure defines Q_{bd} .

To compare the Q_{bd} 's with "best-of-breed" results obtained by F-N stressing, such as those shown by open symbols and lines in Fig. 5 [19], the energies of the electrons were converted to equivalent electric fields necessary in F-N stressing to field-accelerate the electrons to the energies used in our experiments. This conversion assumes that the breakdown process depends predominantly on the energy of the electrons, and not on the field. The results of our breakdown studies are shown by the solid points on the right of Fig. 5. A stress experiment that led to no breakdown is shown by an open

circle. In order to calculate the charge density, we used Monte-Carlo simulation to calculate the area (spread) of the electron beam at the O-S interface [18]. It is obvious by looking at Fig. 5 that the BEEM initiated local breakdowns, when they occur, lie appreciably above an extrapolated curve of data obtained in a conventional, large area stressing experiment. The latter results were deemed to be limited by "intrinsic" properties of the oxide [19]. Our results clearly contradict this view, indicating instead that an intrinsic limit has not yet been reached, and that even in our case breakdowns are still limited by randomly distributed defects and/or impurities of unknown origin.

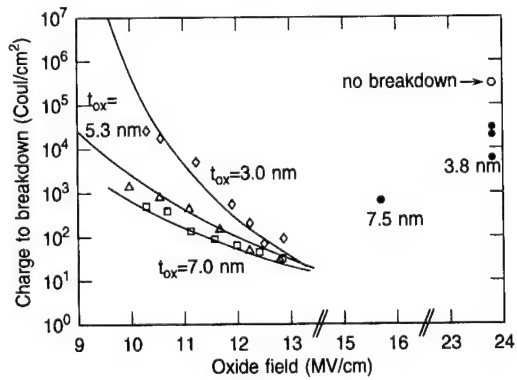


Fig. 5. Electric field dependent breakdowns for MOS structures of indicated thicknesses. Open data points and solid lines are adapted from ref. 19, and correspond to Fowler-Nordheim stressing of macroscopic samples. The solid data points are results from localized BEEM stressing studies. The energies of the STM injected electrons were converted to an equivalent field necessary to achieve those energies.

6. CONCLUSIONS

We have attempted to show the versatility of BEEM to study hot electron transport issues in MOS structures. The technique is the first truly microscopic method that can be used to address a variety of novel transport issues, including stress measurements, on device quality oxides. In particular, we have shown that the direct measurement of the oxide potential maxima (thresholds) allows the determination of charge densities profiles in oxides. In addition, we reviewed oxide breakdown studies that led to additional insights into the breakdown process, and which further indicated that oxide failures

are still dominated by occasional defects and impurities in the oxide.

We acknowledge fruitful discussions with D. DiMaria, D. Buchanan and E. Cartier. This research was partly supported by the Office of Naval Research, under Contract NO. N00014-95-C-0087.

REFERENCES

1. W. J. Kaiser and L. D. Bell, *Phys. Rev. Lett.* **60**, 1406 (1988).
2. M. T. Cuberes, A. Bauer, H.J. Wen, M. Prietsch and G. Kaindl, *Appl. Phys. Lett.* **64**, 2300 (1994).
3. R. Ludeke, A. Bauer and E. Cartier, *Appl. Phys. Lett.* **66**, 730 (1995), *J. Vac. Sci. Technol.*, **B 13**, 1830 (1995).
4. M.P. Murell, M.E. Welland, S.J. O'Shea, T.M.H. Wong, J.R. Barnes, A.W. McKinnon, M. Heyns and S. Verhaverbeke, *Appl. Phys. Lett.* **62**, 786 (1993).
5. S.J. O'Shea, R.M. Atta, M.P. Murell and M.E. Welland, *J. Vac. Sci. Technol.* **B 13**, 1945 (1995).
6. K. Saito, M. Matsuda, M. Yasutake and T. Hattori, *Jpn. J. Appl. Phys.* **34**, L 609 Part 2 (1995).
7. B. Kaczer and J. P. Pelz, *J. Vac. Sci. Technol.* **B 14**, 2864 (1996).
8. M. V. Fischetti and D. J. DiMaria, in *The Physics and Technology of Amorphous SiO₂*, Roderick A.B. Devine, Editor, p. 160, Plenum Press, New York (1988).
9. H.J. Wen and R. Ludeke, *J. Vac. Sci. Technol.* **B 15** July/August 1997, to be published.
10. H.J. Wen, R. Ludeke, D. M. Newns and S.H. Low, *J. Vac. Sci. Technol.* **15 A**, May/June 1997, in press.
11. D. J. DiMaria, *J. Appl. Phys.* **47**, 4073 (1976).
12. E. Harari, *Appl. Phys. Lett.* **30**, 601 (1977).
13. D. J. DiMaria and J. W. Stasiak, *J. Appl. Phys.* **65** 2342.
14. D. J. DiMaria, E. Cartier and D. Arnold, *J. Appl. Phys.* **73**, 3367 (1993).
15. D. A. Buchanan, A. D. Marwick, D. J. DiMaria and L. Dori, *J. Appl. Phys.* **76**, 3595 (1994).
16. R. H. Good and T. J. Nelson, *Classical Theory of Electric and Magnetic Fields*, Academic Press, New York, 1971.
17. J. D. Jackson, *Classical Electrodynamics*, John Wiley, New York, 1962.
18. R. Ludeke, H.J. Wen and E. Cartier, *J. Vac. Sci. Technol.* **B 14**, 2855 (1996).
19. K. F. Schuegraf, D. Park and C. Hu, *Proceedings of the IEEE International Electron Device Meeting*, 1994, p. 609.

Subscription Information

MICROELECTRONIC ENGINEERING (ISSN 0167-9317). For 1997 Volumes 35 to 38 are scheduled for publication. Subscription prices are available upon request from the publisher. Subscriptions are accepted on a prepaid basis only and are entered on a calendar year basis. Issues are sent by surface mail except to the following countries where air delivery via SAL mail is ensured: Argentina, Australia, Brazil, Canada, China, Hong Kong, India, Israel, Japan, Malaysia, Mexico, New Zealand, Pakistan, Singapore, South Africa, South Korea, Taiwan, Thailand, USA. For all other countries airmail rates are available upon request. Claims for missing issues must be made within six months of our publication (mailing) date. Please address all your requests regarding orders and subscription queries to: Elsevier Science B.V., Customer Support Department, P.O. Box 211, 1000 AE Amsterdam, The Netherlands. Fax: 31-20-4853432.

Submission of papers. Papers to be submitted for publication should be sent to one of the Editors-in-Chief. Each paper should be provided with the following: (a) A short title of the paper (for running heads). (b) An abstract not exceeding 150 words and preferably not containing long or complicated formulae. (c) A list of keywords. (d) Original drawings of the figures, suitable for photographic reproduction (drawn in large size, on separate sheets, with wide margins and using India ink). Lettering must be of uniform size (preferably striplettering): typewritten or handwritten lettering is not acceptable. (e) A passport photograph and a short biography of each contributing author.

Upon acceptance of an article, author(s) will be asked to transfer copyright of the article to the publisher. This transfer will ensure the widest possible dissemination of information.

The corresponding author receives **proofs**, which should be corrected and returned by airmail to the publisher within three days of receipt.

No page charge is made. 50 reprints of each paper will be provided free of charge. Additional reprints may be obtained at cost. A reprint order form will be sent to the corresponding author together with the proofs.

Preparation of manuscripts. Manuscripts should be written in English. They should be typewritten originals (plus 4 copies) with wide margins and double space between the lines. Please submit the manuscript in corrected, legible and final form. Corrections in the proof stage other than of printer's errors should be avoided; costs arising from such extra corrections will be charged to the author. Sections must be numbered and must have a title not consisting of formulae only. Long formulae must be displayed and numbered. All symbols which are not typewritten must be listed separately.

Footnotes, which should be kept to a minimum and should be brief, must be numbered consecutively and typed on separate sheets in the same format as the main text.

Figures must be numbered; they must be referred to in the text. The captions must be typed on separate sheets in the same format as the main text.

Tables must be numbered, and typed on separate sheets in ample spacing.

References must be numbered alphabetically. In the text they should be referred to by bracketed numbers. The list of references must be typed on separate sheets, in the same format as the main text, and ordered consecutively, according to the following examples for papers [1], books [2], contributed volumes [3] and unpublished papers [4].

- [1] C.K. Cheong and J.L. Teugels, On a generalization of the random walk, *Stochastic Process. Appl.* **1** (1973) 53-66.
- [2] S.M. Sze, *Physics of Semiconductor Devices*, Wiley, New York, 1969.
- [3] J.M. Abadie, Nonlinear programming, in: K.B. Haley, ed., *Operational Research '78*, North-Holland, Amsterdam, 1979, pp. 900-930.
- [4] S.I. Resnick, Almost sure limit points or record values, Tech. Rept. No. 39, Stanford Univ., Stanford, CA, 1972.

Copyright © 1997 Elsevier Science B.V. All rights reserved.

This journal and the individual contributions contained in it are protected by the copyright of Elsevier Science B.V., and the following terms and conditions apply to their use:

Photocopying. Single photocopies of single articles may be made for personal use as allowed by national copyright laws. Permission of the publisher and payment of a fee is required for all other photocopying, including multiple or systematic copying, copying for advertising or promotional purposes, resale, and all forms of document delivery. Special rates are available for educational institutions that wish to make photocopies for non-profit educational classroom use.

In the USA, users may clear permissions and make payment through the Copyright Clearance Center, Inc., 222 Rosewood Drive, Danvers, MA 01923, USA. In the UK, users may clear permissions and make payment through the Copyright Licensing Agency Rapid Clearance Service (CLARCS), 90 Tottenham Court Road, London W1P 0LP, UK. In other countries where a local copyright clearance centre exists, please contact it for information on required permissions and payments.

Derivative Works. Subscribers may reproduce tables of contents or prepare lists of articles including abstracts for internal circulation within their institutions. Permission of the publisher is required for resale or distribution outside the institution.

Permission of the publisher is required for all other derivative works, including compilations and translations.

Electronic Storage. Permission of the publisher is required to store electronically any material contained in this journal, including any article or part of an article. Contact the publisher at the address indicated.

Except as outlined above, no part of this publication may be reproduced, stored in a retrieval system or transmitted in any form or by any means, electronic, mechanical, photocopying, recording or otherwise, without prior written permission of the publisher.

Notice. *No responsibility is assumed by the publisher for any injury and/or damage to persons or property as a matter of products liability, negligence or otherwise, or from any use or operation of any methods, products, instructions or ideas contained herein.*

© The paper used in this publication meets the requirements of ANSI/NISO Z39.48-1992 (Permanence of Paper).

Printed in the Netherlands

0167-9317/97/\$17.00

Investigation of existing defects and defect generation in device-grade SiO₂ by Ballistic Electron Emission Spectroscopy

H.J. Wen, and R. Ludeke

IBM T. J. Watson Research Center, P.O. Box 218, Yorktown Heights, New York 10598

Degradation processes initiated by defect generation in device-grade SiO₂ were studied by locally injecting hot electrons from a scanning tunneling microscope (STM) tip into Pd/SiO₂/p-Si(100) MOS structures. An analysis of the emerging collector current in the Si substrate, a technique known as Ballistic Electron Emission Microscopy (BEEM), provides electron transport information, from which the oxide defect generation process was studied. The charging of the defects resulted in shifts of threshold energies for electron transport across the oxide. A novel sheet charge model was developed to assess the in-depth distribution and charge densities in the oxide from field-induced threshold shifts obtained from experiment. An as-fabricated MOS system with an oxide thickness of 71 Å was investigated and found to contain existing electron traps of charge densities in the range $(0.7\text{--}2.8)\times10^{13}$ e/cm² that are distributed within a 30 Å region adjacent to the metal/oxide interface. Further stressing was performed at zero oxide bias with increasing tip voltages of up to -10 V. New electron traps characterized by charge densities of $(1.9\text{--}3.6)\times10^{13}$ e/cm² and located within 40 Å of the SiO₂/Si interface were generated when the kinetic energy of the electrons injected into the SiO₂ conduction band exceeded 1.9 eV. This energy threshold is in very good agreement with the hydrogen-release energy that is frequently invoked to explain oxide degradation.

I. Introduction

The performance and reliability of modern metal-oxide-semiconductor (MOS) devices are ultimately dependent on the electronic properties of the silicon dioxide, and those of its interfaces with the Si substrate and the gate metal [1]. The electronic breakdown characteristics, which are determined by defects and impurities in the SiO_2 bulk or at its interfaces, become increasingly sensitive to local fluctuations in material properties as device dimensions are reduced [2-5]. The present understanding of degradation and breakdown mechanisms is largely based on studies on MOS capacitor structures with techniques such as Fowler-Nordheim (F-N) tunneling injection, internal photoemission, etc. [6-23]. The results of these studies represent properties typically averaged over sampling areas of 0.01 to 1 mm^2 , which do not necessarily reflect sample variations on a microscopic scale. Further shortcomings of the standard electron injection techniques, including F-N tunneling, require high fields across the oxide to energize the injected electrons. The high fields result in position dependent kinetic energy distributions of the electrons as they traverse across the oxide layer. For thicker oxides the energies may ultimately reach values sufficient to cause impact ionization in the oxide [6-10]. Even at much lower fields the electrons still may reach energies sufficient to generate hot holes in the Si by impact ionization, which then can be injected into the silicon dioxide valence band [11,12]. The presence of diverse types of hot carriers complicates the determination of oxide degradation mechanisms. The two most popular models, referred to as “impact ionization” and “trap creation”, are both based on strong electron heating in the oxide [6-16]. Impact ionization occurs when electrons in the oxide reach energies exceeding the SiO_2 band gap energy of 9 eV, which is necessary for creating electron-hole pairs in the oxide. Electron-hole recombination can then create interface states and electron traps. Defects in the “trap creation” model are generated by hot electrons breaking hydrogen-silicon bonds at the anode. The released hydrogen atoms diffuse to the cathode where they combine with other hydrogen atoms and escape, leaving defects behind. In this model the energy of hot electrons has a minimum threshold of ~ 2 eV in order to break H-Si bonds. However, under high field conditions the two defect generation mechanisms may coexist, which complicates the study of the many details of the processes. Moreover, such macroscopic results can not precisely describe microscopic details of broken bonds, interface

states and charge traps. In order to understand oxide breakdown from a more fundamental point of view, studies on a microscopic scale become necessary.

In this article we present results from Ballistic Electron Emission Microscopy (BEEM) studies of both existing defects and the generation of new defects in gate oxides and near the interfaces of MOS structures. The results reported here were obtained for a 71 Å gate oxide. An “as-fabricated” MOS structure was found to have electron trap densities in the range of $(0.7\text{--}2.8)\times10^{13}$ e/cm² that are distributed within a 30 Å region adjacent to the metal/oxide (M-O) interface. New electron traps, observed as trapped charge densities of $(1.9\text{--}3.6)\times10^{13}$ e/cm² distributed within 40 Å of the SiO₂/Si interface, were generated when the energy of the hot electrons exceeded 1.9 eV. This value is close to the minimum energy of ~ 2 eV required to break hydrogen-silicon bonds [15]. This process suggests that the initial defect generation, which eventually leads to a destructive breakdown of the oxide, is associated with the “trap creation” model by releasing hydrogen. Hole injection and impact ionization are absolutely excluded in the present study, since the stressing was carried out at zero oxide bias and the kinetic energy of hot electrons was below the threshold for band gap ionization.

II. Experimental details

A. Ballistic electron emission microscopy/spectroscopy at various oxide fields

BEEM is a STM based microscopy/spectroscopy. In this study electrons were injected from a STM tip into the metal layer of a MOS structure, as shown in Fig. 1 (a). The sole purpose of this metal layer is to provide a potential reference plane, represented by the Fermi level in the metal, which is connected to ground in the present case. With the STM tip biased at V_T relative to the Fermi-level in the metal, the electrons tunneling from the tip into the metal have a near-exponential energy distribution f_T with a maximum kinetic energy equal to eV_T, as shown in Fig. 1(b). In our BEEM configuration a maximum value of V_T = -13 V can be achieved, which corresponds to a kinetic energy of 9 eV relative to the conduction band minimum of the SiO₂ for the hottest injected electrons. For comparison, to reach this value in a 7 nm oxide by conventional F-N injection, a field of ~ 18 MV/cm would need to be applied. A separate gate bias V_b can also be readily applied between the metal and silicon substrate. This allows complete control over the field in the oxide and further modifies the electron energies. In general, the

potential drop V_{ox} includes one part from the gate bias V_b and another part from the difference in workfunctions between the metal and Si substrate. Since V_b affects both V_{ox} and the band bending of the Si at the SiO_2 -Si interface, the relationship between V_b and V_{ox} is nonlinear and can be obtained by solving Poisson's equation [1, 25]. Thus the energy of electrons injected into the SiO_2 conduction band can not only be arbitrarily selected by changing the tip bias, but also independently modified by adjusting the oxide bias, thereby increasing the accessible energy range and allowing greater experimental flexibility.

The thickness of the metal layer should be of order of the electron scattering length in the metal, or preferably less, so that most of the electrons traverse the metal layer ballistically. In order to traverse the MOS structure and reach the Si substrate, the kinetic energy of the electrons must be larger than the potential barrier height in the MOS structure. The barrier height and shape in MOS structures is a much more complicated issue than for the metal/semiconductor system. It varies with the oxide bias, charge in the MOS system, work-function difference between the metal and the Si substrate, and image force effects at the interfaces. Fig. 1(b) shows the schematic energy band diagram of the Pd/ SiO_2/p -Si system at $V_b = 0$. By taking the potential step V_0 at the Pd/ SiO_2 interface at zero oxide bias to be 4.08 eV [29, 30], a band offset of 3.2 eV at the SiO_2/Si interface and a Fermi level location ~ 0.2 eV above the valence band maximum in the Si substrate, a nearly zero work-function difference between Pd and p -Si is deduced. Therefore, at zero oxide bias the bands of the Pd/ SiO_2/p -Si system are essentially flat. It should be noted that only image force effects, but no electron tunneling through the barrier [29,30] are considered in Fig. 1 (b) and (c). For the conditions of Fig. 1(b), electrons need a minimum kinetic energy of eV_0 to attain finite probabilities for crossing the M-O interface, traversing the oxide and being finally collected in the Si substrate as a collector current I_C . As a function of increasing V_T , I_C is zero until V_T reaches the value of the potential step V_0 ; thereafter it increases monotonically. The I_C vs V_T spectra thus exhibit a threshold at V_0 . However, the location of the potential maximum and its height vary in the presence of an oxide charge. An energy diagram under positive oxide bias for an oxide film with negative trapped charge in the central region is shown in Fig. 1(c). One can readily realize that the effective barrier height Φ_{th} is strongly dependent on the charge density, charge distribution and the applied oxide bias. Assuming the charge is distributed narrowly (sheet charge) and parallel relative to the interfaces, the effective

barrier height lowering should then be linearly proportional to the applied oxide bias, with the slope of this relationship representing the location of the potential maximum as a fraction of the oxide thickness relative to the metal interface. In other words, charge density and charge location can be extracted from the field dependence of the effective barrier height. It should be noted that in Fig. 1(c) the sheet image charge in the metal is not depicted. Its inclusion is necessary for the interpretation of the BEEM results, and will be discussed in section III. The experiment was devised as follows. As a first step, the as-fabricated MOS structures (without any hot electron stressing) were investigated. The existing defects manifest themselves as negative charge, which increases the effective barrier height and reduces the transmission probabilities. The location of existing defects was extracted by analyzing the field dependence of the barrier height. Then hot electrons were injected with a variable tip voltage of up to -10 eV in order to stress the oxide film. In this way, new defects were generated and further characterized by their field dependence.

B. Sample preparation

Device quality oxide layers were thermally grown near 800 °C in dry oxygen on 125 mm diameter Si(100) wafers doped with boron to about 10^{16} cm^{-3} . No additional treatments were made after oxidation. Here we report studies on an oxide layer with a thickness $t_{\text{ox}} = 71 \pm 1 \text{ \AA}$. The thickness was determined with an ellipsometer. Approximately $2 \times 12 \text{ mm}^2$ pieces were cut from the wafers and introduced into an UHV chamber, where Pd dots, 0.2 mm in diameter, were thermally evaporated through a shadow mask. During deposition, the substrate was held at a temperature of about 30 K, which was necessary to inhibit surface diffusion. A peak-to-valley roughness of about 15 Å was measured for a 40 Å Pd film thickness. After evaporation, the sample was allowed to warm up to room temperature and was subsequently transferred under UHV into the STM chamber, where the BEEM grounding contact was gently positioned onto a selected Pd dot by means of three orthogonally mounted Inchworms. MOS structures with leakage resistance $\geq 10^{12} \Omega$ were generally suitable for our studies.

C. Data acquisition

All measurements were carried out when drifts caused by sample drift and piezocrystal creep were less than 1 Å/min. in both the x- and y-directions. The low drifts were achieved either

by waiting until the instrument was finally stabilized or by using drift compensation. In the spectroscopy mode the raster scan of the STM is stopped and the collector current I_C is measured as V_T is ramped over a range that includes the barrier height. The barrier height manifests itself as a threshold voltage in the I_C vs V_T scan, from which the threshold is extracted with a model fit to the data [25]. The fitting process ensures negligible contributions to the threshold value from electrons tunneling through the barrier [29,30]. The STM topographic images were taken in the conventional, feedback-controlled constant tunnel current (I_T) mode. I_C can also be recorded simultaneously, thereby generating an electron transmission or BEEM image of the MOS structure. Both point stressing and area stressing, achieved by injecting hot electrons at a point or over an area of $250 \times 250 \text{ \AA}^2$, were performed. In order to gain statistical information on a microscopic scale, I_C vs V_T curves were taken at 36 points of a grid pattern spread over a $250 \times 250 \text{ \AA}^2$ area of the surface, with a spacing of 40 \AA between points. It should be emphasized here that thresholds were obtained from single spectral scans (no averages), since we aimed to detect small changes that contain important information regarding the statistical nature of microscopic defects. Therefore all threshold energies presented here have an error bar of $\pm 0.05 \text{ eV}$. Further experimental details will be given as specific measurements are discussed. Details regarding the STM can be found elsewhere [26].

III. Data interpretation and discussions

A. Observation of existing traps and mechanisms of new trap generation.

As mentioned earlier, the experiment was arranged to first investigate as-fabricated oxides before any intentional stressing. The existing traps are referred to as background or initial defects/impurities in the oxide and at the interfaces, which are incorporated into the structure during fabrication or processing and can be easily charged up by the injection of electrons or holes. These defects vary with the fabrication process and may be different in sign, density and location from defects generated in aging studies. Therefore we intent to study first the existing, electrically active defects.

Fig. 2 depicts a set of sequentially taken BEEM spectra that show a monotonic increase of the threshold with the number of spectral scan. These shifts clearly indicates that the mere spectrum acquisition process already begins to fill the pre-existing traps. During acquisition of

in these spectra the STM tip was located at the same point over the sample, the tip voltage was ramped only up to -6 V and the oxide bias was held at zero in order to prevent electron energy from exceeding 2 eV, which is considered a “soft” threshold for generating new defects. Each scan took less than 20 s. After the 8th scan the energy position of the threshold was stabilized. The increasing threshold indicates that the existing defects are electron traps. The final, stabilized threshold energy is \sim 5.0 eV. This value, however, varies not only from one sample to another, as presented in Fig. 3 (the data in Fig. 2 were taken on sample 1 in Fig. 3) but may occur at different locations on a microscopic scale, as illustrated by the spread in thresholds depicted in Fig. 4. Such variations reflect a distribution in the local charge density of the existing traps, as will be presented in section III. D.

After the existing traps were saturated with electrons, i.e. no further shifts were observed in the BEEM spectra, hot electrons were injected with the STM tip on purpose to stress the oxide. The stress-induced defects manifest themselves as further shifts in the threshold energy, as shown in Fig. 3. The electron kinetic energy on the abscissa of Fig. 3 is given by $eV_T - e\Phi_{th}$. The zero threshold shift corresponds to the Pd-SiO₂ barrier height of 4.08 eV under flat band conditions [29,30]. As discussed in section II [Fig. 1 (b)], the flat band condition for Pd/SiO₂/p-Si corresponds to $V_b = 0$ V, with the assumption that no trap filling has occurred. Thus a deviation from the 4.08 threshold gives us an indication that the sample area below the tip is charged. For example, the first spectrum of Fig. 2 shows the threshold of 4.20 ± 0.05 eV, indicating a nearly charge-free area. The curves in Fig. 3 show a “soft” threshold of \sim 1.9 eV for the kinetic energy of the injected electrons. The curves continue to increase above this threshold, which indicates that more defects are generated by the increasingly hotter electrons. It must be noted that several spatially separated places were investigated during hot electron stressing. For a given electron kinetic energy above \sim 1.9 eV, fluctuations in the BEEM threshold with values as low as 5.0 eV were observed at several stressed points. Such extreme low values are attributed to leakage of the trapped charge, a process believed to occur in the pre-breakdown region [28]. The data presented in Fig. 3 correspond to the highest value measured at several stressing places for a given electron kinetic energy. The “soft” threshold of \sim 1.9 eV can be directly related to the “trap creation” model. This model implies that traps are created by hot electron-initiated breaking of

the hydrogen-silicon bonds at the SiO_2/Si interface, a process that needs an energy of ~ 2 eV [14-16, 23]. Consequently, we can postulate that the newly generated traps are located near the SiO_2/Si interface, a premise that is substantiated by the field dependent experiment presented in section III. C.

Since the kinetic energy for bond-breaking is referenced to the potential maximum, electrons of energies exceeding 1.9 eV are hot enough anywhere in the oxide to release hydrogen. In contrast, for F-N injection, the field accelerated electrons have a higher probability to release hydrogen as they move towards the anode. The defect generation process for the present case can be described as follows. Hot electrons with $E_k > 1.9$ eV release hydrogen both at the M-O interface and the SiO_2/Si interface. Since the M-O interface is believed to be a much hydrogen-rich source [23], hydrogen atoms diffuse from there to the SiO_2/Si interface, where they combine with other released hydrogen and escape. Both the hydrogen releasing and recombination processes are potential defect generation mechanisms.

B. Location of existing traps.

The trap densities and locations, as well as their polarity (electron or hole traps), are the relevant issues in trap characterization studies. In order to characterize existing traps, the following experiment was devised.

A pristine area of $250 \times 250 \text{ \AA}^2$ was first investigated in the spectroscopy mode by measuring a set of 36 spectra in a grid pattern. The tip voltage was ramped from -2V to -6V in order to avoid new defect generation. It was observed that only a few, but always the first of the 36 spectra showed a threshold energy of 4.05 ± 0.05 eV, whereas most subsequent spectra already exhibited increases in thresholds of ~ 0.5 eV. This implies that the electrons injected into the SiO_2 conduction band during acquisition of the first spectrum quickly fill nearby existing traps and that this sequence is repeated during subsequent spectral scans. This process also indicates that in the present case the electron beam spread in the oxide exceeds the sampling spacing of 40 \AA , as was also observed in a previous study [24]. The area was then scanned with a tip voltage of -6 V until no further shifts were observed in the threshold energies, which indicates that saturation of the trap filling process was achieved. It must be noted that after saturation the spread in threshold energies of the 36 spectra for each data set exhibited an approximate Gaussian distribution. Their

maximum, minimum threshold energies, and that at the distribution maximum are indicated in Fig. 4 by the up and down triangles and square symbols, respectively. The achievement of saturation means that the distribution does not change with further scans; it does not imply that each individual spectrum shows exactly the same threshold energy as the previous one, since the STM tip can not exactly approach the same 36 sampling points between consecutive data sets. Such statistical results are better than a result from only one stressing point, since they provide a distribution of the existing trap densities over a microscopic area.

The oxide field dependent experiment was then performed in order to determine the trap distributions and densities. Identical grid patterns of 36 spectra were taken for gate biases in the sequence of 1 V steps from 0 through 7 V and back to 0 and -1 V, which corresponds to external oxide potentials of the same values. This simple relationship results from the fact that the Fermi level at the interface remains near the top of the Si valence band (in accumulation) due to the internal oxide field caused by the trapped charge. The threshold energies for $V_{ox} = 7$ V were difficult to determine due to a relatively large background leakage current and therefore were not included in Fig. 4. The corresponding STM topographic images, generated concurrently with the spectral set, were used to check if the tip stayed at the same area. The results are presented in Fig. 4. It is seen that all three threshold data sets: minima, maxima and distribution maxima of the 36 spectra exhibit almost the same field dependence and are, moreover, equally separated in energies. This well behaved and scatter-free behavior leads to the following conclusions: (a) the consistent spread between extrema and the distribution maxima, as well as their smooth dependence on V_{ox} , are well represented by the limited sampling size of 36, that is, the data is statistically meaningful. (b) Although each data set was not taken at the same points, the locations where the data sets were taken statistically exhibited very similar electrical environments, (c) no further trap filling takes place when V_{ox} increases from zero, and (d) the distribution of the threshold energies represents a local fluctuation of trapped charge densities. In comparison, the pure image force lowering as a function of the oxide field is also indicated by the solid circles in Fig. 4. One readily sees that not only its field dependence differs from that of the three data sets, but that the shifts are also much smaller. It should be noted that this data set was taken from areas where no trapped charge was present, as detailed in our previous work [29,30].

As mentioned in section II A., the magnitude of the field-dependent threshold shifts depends on the location of the potential maximum, which in turn depends on the charge distribution in the oxide. The field dependence of the three parallel data sets in Fig. 4 exhibits approximately three regions, as distinguished by vertical dotted lines. The region of V_{ox} ranging from 0 to 3 V has a nearly linear behavior with a slope of ~ 0.3 , while the region for $V_{ox} > 3$ V first shows a segment of weak field dependence that is followed by one of strong dependence and eventual saturation. When the oxide potential V_{ox} changes from 0 V to -1 V, the threshold energies increase by ~ 0.6 eV, a value that is twice the 0.3 eV shift expected solely from the applied oxide bias.

We can understand the overall field dependence through a simple model that will be detailed in section D. The model assumes that the trapped charge is distributed over separated sheets of charge parallel to the metal/oxide interface. When there is only one sheet charge present the potential maximum is located at the sheet charge position, whereas in the presence of several sheets of charge the shape of the total potential depends on their relative strength. Since charge in an MOS structure is spatially distributed, a detailed rendering of its effect on the potential can be reasonably approximated by considering several sheets of charge. A few general observations of the field dependence of the thresholds are worth stating here. The 0.3 slope indicates that the potential maximum in the bias range $0 < V_{ox} < 3$ V is located around $0.3 \times 71 \approx 20$ Å from the M-O interface. This is a direct consequence of the reduced leverage of the applied oxide bias in affecting the potential maximum, whose position relative to the M-O interface is directly proportional to the slope of the field dependent threshold shifts. Consequently, the closer the barrier maximum is to the M-O interface, the smaller will be the barrier lowering for a given increase in oxide bias. The data up to the $V_{ox} = 3$ V indicates that the effective barrier lowering caused by a 3 V bias is 1 V, which compensates the original 1 V shift due to trap filling (approximately the shift between the solid circle and the square at $V_{ox} = 0$ V). However, for $V_{ox} > 3$ V, the softening of the curves implies that the field no longer affects the threshold energies. The curves bend down again upon further increasing the bias. This is attributed to a neutralization process and/or a discharge under high fields. It must be noted that after finishing the measurement at the high fields and before the bias was set to -1 V, three data sets at $V_{ox} = 0$ V were taken again. These points are represented by open symbols. The square and down triangle

are located 0.2 eV higher than the original positions, which can be assigned to a few new traps generated during the measurement at high fields. These new traps are believed to be similar as those discussed in section III. C. The dramatic increase in the thresholds for negative bias can only partially be attributed to the filling of additional electron traps close to the oxide/silicon interface. The additional charge required to fully account for the observed shift would exceed 10^{13} e/cm², a value that requires an extremely high density since the shift of the Fermi level in the Si at the interface is at most a small fraction of a volt by changing the bias from 0 to -1 V (the reader is reminded that the p-type Si at the interface is in accumulation). We attribute the excess in threshold shifts for negative bias as being predominantly caused by a change in the screening at the Si-SiO₂ interface from metallic to dielectric as the bias polarity is changed from positive to negative. This topic will be discussed in section III D.

C. Location of generated traps

A procedure similar to that for the pre-existing defects was followed to characterize new traps generated by hot electrons of energies exceeding 1.9 eV. A pristine area of $250 \times 250 \text{ \AA}^2$ was again chosen and characterized spectroscopically in a grid pattern of 36 sampling points that exhibited a few sites with low thresholds of ~ 4.0 eV. Hot electrons were then injected over the entire area in sequences of increasing tip voltages of up to -10 V and with $V_b = 0$ V. 36 spectra over the usual grid pattern were taken after each injection sequence in order to check threshold shifts. These followed a behavior similar to that shown in Fig. 3. Finally, the area was further scanned with $V_T = -10$ V until no more shifts in the threshold distributions were observed. For $V_{ox} = 0$ the saturated distribution corresponds to the maximum and minimum threshold energy of 7.2 eV and 6.0 eV, as indicated by up and down triangles in Fig. 5, respectively. In comparison to Fig. 4, the larger threshold shifts clearly indicate that new electron traps were generated by the hot electrons. Then the field dependent experiment was performed. Spectra over the usual 36 sampling points were then taken in a series with V_{ox} equal to 0, 1, 2, 3, 4, 5, 6, 7, 0, and -1 V. Due to instabilities of the trapped charge, data sets for $V_{ox} > 2$ V were so noisy that only a few of the 36 spectra exhibited reliable threshold characteristic. Consequently not enough data were available to determine a statistic distribution of thresholds. Therefore only the maximum and minimum threshold energies are presented in Fig. 5. The observed noise in the spectra is

attributed to charging and discharging of the new traps at high oxide fields, a process that can happen when the trapped charge is located close to the oxide/silicon interface, or to charge neutralization via hot hole injection from the Si valence band. Although the data sets are not extracted from good statistical distributions, they still show the same field dependent behavior, which leads us to conclude that their separation adequately describes the maximum and minimum densities of the trapped charge. One sees in Fig. 5 that the field dependence is in general similar to that of Fig. 4, but the magnitude of the shifts are considerably larger. In comparison, the field dependent pure image force effect is also shown by the solid circles in the Fig. 5. The observed field dependence is also divided into three regions, a nearly linear region with a slope of ~ 0.6 between $0 - 2.5$ V, a region for $V_{ox} > 2.5$ V that exhibits first a weak field dependence and then a much stronger one, and another region for V_{ox} between 0 and -1 V where the threshold energy dramatically increases by ~ 1.3 V.

From the slope of 0.6, we deduce that the potential maximum for V_{ox} between $0 - 2.5$ V is located at ~ 30 Å from the SiO_2/Si interface. A softening of the field dependence at ~ 2.5 V indicates that the maximum in the potential barrier shifts closer to the M-O interface, which implies a distributed oxide charge. At still higher oxide fields the increased rate of threshold shifts is again interpreted in terms of charge loss (neutralization or/and discharging). This high-field induced effect is also reflected in the ~ 0.5 eV lower threshold energies at $V_{ox} = 0$ V *after* high fields have been applied (open symbols). The dramatic increase for negative bias is largely attributed, as will be discussed in the next section, to changes in the screening mechanism at the SiO_2/Si interface.

D. Sheet charge model: charge density determination

Although oxide charge is expected to be distributed over some depth, it nevertheless can be reasonably approximated by one or more sheet charges so located that their resulting potential can describe the experimental observations. From previous discussions of the field dependence of the BEEM thresholds (Figs. 4 and 5) for $0 < V < 3$ V, it was concluded that a constant slope implies a specific position of the potential maximum relative to the M-O interface. In this case a single sheet charge located at the potential maximum would give a suitable potential profile. We model a single sheet charge in the oxide by considering it as a disk of radius R parallel to the

oxide interfaces, of charge density σ_j and located at a distance d_j from the M-O interface. The potential $\phi_j(d_j-x)$ along the axial direction x in an infinite dielectric medium of dielectric constant ϵ_{ox} is given by [31]:

$$\phi_j(d_j - x) = \frac{\sigma_j}{2\epsilon} \left\{ \left[(d_j - x)^2 + R^2 \right]^{1/2} - |d_j - x| \right\} \quad (1)$$

where $\epsilon = \epsilon_0 \epsilon_{ox}$. ϵ_0 represents the permittivity of free space. The real potential $\Phi_j(x, d_j)$ must be zero at both interfaces because of metallic screening. These boundary conditions are satisfied by using the method of images [31], which is accomplished by adding the potentials of the image charges, including those from higher order terms (images of images, etc.):

$$\begin{aligned} \Phi_j(x, d_j) &= \phi_j(d_j - x) - \phi_j(d_j + x) \\ &- s[\phi_j(2t_{ox} - d_j - x) - \phi_j(2t_{ox} + d_j - x) - \phi_j(2t_{ox} - d_j + x) + \phi_j(2t_{ox} + d_j + x)] + \dots \end{aligned} \quad (2)$$

Here $s = (\epsilon_s - \epsilon_{ox}) / (\epsilon_s + \epsilon_{ox})$ is the effective screening factor at the O-S interface, with ϵ_s an effective dielectric constant of the semiconductor at the interface. For accumulation (or strong inversion) ϵ_s is assumed to become very large, so that $s \rightarrow 1$ (metallic screening). For $\epsilon_s = \epsilon_{Si} = 11.8$, $s = 0.5$. The profile of the resulting potential for a single disk shaped sheet charge is triangular, with the maximum (apex) at the location d_j of the sheet charge. In general, one can approximate the potential from a charge distributed along x by summing over a series of potentials arising from j individual sheet charges: $\Phi_T = \sum \Phi_j$. The barrier potential U is obtained by adding Φ_T to the sum of the barrier, field and image force potentials for the injected electron:

$$U = \Phi_T + V_0 - V_{ox}x/t_{ox} - q/(16\pi\epsilon x) \quad (3)$$

As discussed earlier in reference to Fig. 4, the potential maximum, judged from the slope in 0-3 V bias region, is $\sim 0.3t_{ox}$ or ~ 20 Å from the M-O interface. A single sheet charge was placed at this position (d_1) and its strength adjusted so that the total barrier potential U in eq. (3) matches that of the experiment for $V_{ox} = 0$. A single sheet charge, however, overextends the region over

which the slope equals 0.3 in Fig. 4. In order to account for the observed saturation for $V_{ox} > 3$ V, the potential Φ_T must bulge in the region of $x < d_1$. This occurs only if additional negative oxide charge is located within d_1 , which will be represented here by a second sheet charge placed at $d_2/t_{ox} = 0.11$ (~ 8 Å). Its density σ_2 is adjusted to mimic the softening observed in Fig. 4 for $V_{ox} > 3$ V. For a good general fit to the data, a third sheet charge was required beyond $d_1/t_{ox}=0.3$, specifically at $d_3/t_{ox}=0.41$. The σ_j 's were varied for an optimal fit to the data of Fig. 4 (solid squares), with relatively little freedom in the choice of the parameters. The net potential arising from the three sheet charges, indicated by the vertical bars in Fig. 6, is shown as curve Φ_{fs} , where the subscript refers to the choice of full (metallic) screening at both interfaces. The field dependent representations of the full barrier potential U (eq. 3) are shown as well in Fig. 6. The changing role of each sheet charge in determining the potential maximum as V_{ox} is increased from zero is clearly evident in the figure. The right-most sheet charge dominates for 0 and negative bias; the center charge dominates to $V_{ox} \sim 3$ V, beyond which the innermost sheet charge takes over. However, the subsequent rate of threshold lowering remains relatively weak and does not account for the drop beyond 5 V observed in Fig. 4. This can only be explained by a decrease in charge density (neutralization or discharging) under the highest field conditions ($V_{ox}=6$ V), which can readily be simulated by lowering the net charge residing in the three sheets to 50% of its value. This reduction of the charge can conceptually occur either through field ionization or neutralization by hot holes injected into the oxide from the Si anode. Since prolonged high-field exposure without electron injection did not affect the thresholds measured subsequently at $V_{ox}=0$, we tend to ascribe the charge reduction to hole injection. Hole creation and injection is the result of electron-hole pair creation in the Si by impact ionization of hot electrons coming from the oxide. This process is quite efficient for electrons with kinetic energies > 5 eV in the oxide [32].

As pointed out earlier in the discussions of Figs. 4 and 5, the large threshold shifts for negative bias appear to be anomalous, as the expected shifts would lie closer to values obtained by extrapolating the positive-biased segments of the curves near zero into the negative region. A sudden inrush of negative charge into the oxide at the O-S interface is unlikely, as this would suggest an interface trap density of the order of $10^{14}/\text{cm}^2 \cdot \text{eV}$ near the Fermi level. However, the negative bias does have the tendency to move the Fermi level out of the valence band, which

drastically affects the hole density in the Si at the O-S interface (because of the oxide charge the Fermi level remains near the top of the valence band). The decrease in the interface hole density has the effect of reducing the screening, which is described by the parameter s in eq. (2). A value of $s=0.7$ was used to account for the observed threshold shifts for $V_{ox} = -1$ V. The resulting change in the oxide-charge potential is seen in the dotted profile marked Φ_{ps} in Fig. 6, as well as in the barrier potential shown by the top-most dashed curve. Φ_{ps} includes a contribution from a dipole charge of 3×10^{12} e/cm² located at $x/t_{ox}=0.8$ that is necessary to maintain band off-sets at the interface. Its effect is seen by the slight kink in the two broken curves of Fig. 6. The maxima in the oxide barrier potentials of Fig. 6 are depicted in Fig. 4 by the dashed line. A similar treatment was followed for the generated defects, which were represented by an additional three sheet charges. We show here only the results, which are represented by a dashed line in Fig. 5 for the data corresponding to the lower limit in shift distributions. The parameters used to calculate the various potentials for both figures are summarized in Table I. It should be pointed out that other profiles and distributions, such as spreading the charge over much broader regions across the oxide, gave decidedly poorer fits to the experimental data, which in most cases could only be fitted over a narrow bias range. The radius $R=16$ nm for all sheet charges was chosen to give an area equal to the scanned and stressed areas used in the experiments to generate the data for Figs. 4 and 5. This value was extracted from the transmission image of the stressed area shown in Fig. 7.

Several conclusions may be deduced from the results of the modeling. The obtained densities and location of existing traps near the M-O interface are consistent with previous observations on metal gated MOS structures [32]. Secondly, the trap densities near the M-O interface remain the same after the hot electron generation of new traps (in Table I, σ_j for existing traps remains the same in both columns). This means that hot electron stressing does not generate additional traps near the M-O interface, which supports our original interpretation that these traps pre-existed the BEEM experiment. Finally, the densities and location of the generated traps are not inconsistent with conclusions obtained with the hydrogen release model, which proposes a dangling bond origin of the traps as the hydrogen atom is stripped from the passivated Si-H bond near the SiO₂/Si interface.

E. Imaging charged traps

After completing the field dependent stress experiment, a large area of $750 \times 750 \text{ \AA}^2$ that included the stressed area of $250 \times 250 \text{ \AA}^2$ was imaged simultaneously in the topographic and BEEM transmission modes, as shown in Fig. 7. The stressed area is seen as a low transmission region of approximately $320 \times 320 \text{ \AA}^2$. The observation of a low-transmission region that is larger than the stressed area is attributed to a lateral spread of the electron beam injected into the SiO_2 conduction band during the stressing and/or the data acquisition process. It should be noted that before stressing the BEEM image of this area only exhibits a contrast resulting from the nodular character of the Pd surface, as is still evident in the periphery of the BEEM image. Stressing at one point was performed several times. An analysis of the threshold shifts in the proximity of the stressing point indicates a beam spread of $\sim 100 \text{ \AA}$, a value that can explain the large area of low BEEM transmission in Fig. 7. We would like to emphasize that at least for thick oxides, besides the influence of the metal topography on the BEEM image, such a big beam spread is another critical obstacle to the observation of individual traps, which would be a highly desirable achievement.

IV. Summary

We have used a STM tip to locally injected electrons into MOS structures consisting of a 35 \AA Pd layer on a 71 \AA oxide, with the intent of studying defects and defect generation in SiO_2 gate oxides on a microscopic scale. Electron transport processes were studied by analyzing the BEEM collector current emerging from the Si substrate. In particular the shifts in thresholds were investigated that resulted from increases in the oxide potential due to the presence of trapped charge. A model was developed for the dynamic oxide potential profile that includes contributions from the oxide charge, field effects and image force (screening) effects from the interfaces. From the observed field dependence of the thresholds and suitable modeling, charge profiles and charge densities were deduced. The “as-fabricated” MOS structures exhibited charged electron trap densities of $(0.7\text{--}2.8) \times 10^{13} \text{ e/cm}^2$ that were distributed with decreasing density within 30 \AA of the M-O interface. Stressing with hot electrons of energies exceeding 1.9 eV generated new electron traps, which manifest themselves as a trapped charge density of $(1.9\text{--}3.6) \times 10^{13} \text{ e/cm}^2$ located within 40 \AA of the SiO_2/Si interface. The value of 1.9 eV is in excellent

agreement with the minimum energy of ~2 eV required to break hydrogen-silicon bonds. The electrically stressed area was observed microscopically as a region of low transmission that results from the presence of electrons captured by the traps in the oxide.

We benefited from discussions with D.J. DiMaria, D.A. Buchanan and E. Cartier. This research was supported by the Office of Naval Research under contract N00014-95-C-0087.

- [1] E.H. Nicollian and J.R. Brews, MOS Physics and Technology (John Wiley, N.Y., 1982)
- [2] C. Hu, Proc. IEEE **81**, 682 (1993)
- [3] C.A. Mead, Analog Integrated Circuits and Signal Processing **6**, 9 (1994)
- [4] Y. Taur, Y.-J. Mii, D. J. Frank, H.-S. Wong, D.A. Buchanan, S. J. Wind, S.A. Rishton, G.A. Sai-Halasz, and E.J. Nowak, IBM J. Res. Develop. **39**, 245 (1995)
- [5] Semiconductor Technology Workshop, Working Group Reports, Semiconductor Industry Association, San Jose, 1993
- [6] P. Solomon, J. Vac. Sci. Technol. **14**, 1122 (1977)
- [7] D. J. DiMaria, T.N. Theis, J.R. Kirtley, F.L. Pesavento, D.W. Dong, and S.D. Brorson, J. Appl. Phys. **57**, 1214 (1985)
- [8] M.V. Fischetti, D.J. DiMaria, S.D. Brorson, T.N. Theis, and J.R. Kirtley, Phys. Rev. B **31**, 8124 (1985)
- [9] D. Arnold, E. Cartier and D.J. DiMaria, Phys. Rev. B **45**, 1477 (1992)
- [10] D.J. DiMaria, D. Arnold, and E. Cartier, Appl. Phys. Lett. **60**, 2118 (1992)
- [11] K.F. Schuegraf and C. Hu, IEEE Trans. Electron Devices **41**, 761 (1994)
- [12] K.F. Schuegraf, D. Park, and C. Hu, Proceedings of the IEEE International Electron Device Meeting, 1994
- [13] D. Arnold, E. Cartier and D.J. DiMaria, Phys. Rev. B **49**, 10278 (1994)
- [14] E. Harari, Appl. Phys. Lett. **30**, 601 (1977)
- [15] E. Cartier and D.J. DiMaria, Microelectron. Eng. **22**, 207 (1993); D.J. DiMaria, E. Cartier, and D. Arnold, J. Appl. Phys. **73**, 3367 (1993)

- [16] D.J. DiMaria and J.W. Stasiak, *J. Appl. Phys.* **65**, 2342 (1989)
- [17] P. Olive, T.N. Nguyen, and B. Riccó, *IEEE Trans. Electron Devices* **35**, 2259 (1988)
- [18] P. Olive, T.N. Nguyen, and B. Riccó, *IEEE Trans. Electron Devices* **38**, 527 (1991)
- [19] P.P Apte, T. Kubota, and K.C. Saraswat, *J. Electronchem. Soc.* **140**, 770 (1993)
- [20] L.K. Han, M. Bhat, D. Wristers, J. Fulford, and D.L. Kwong, *Proceedings of the IEEE International Electron Device Meeting*, 1994
- [21] S.-H. Lee, B.-J. Cho, J.-C. Kim, and S.-H. Choi, *Proceedings of the IEEE International Electron Device Meeting*, 1994
- [22] C.-H. Lin, J. Cable, and J.C.S. Woo, *IEEE Trans. Electron Devices* **42**, 1329 (1995)
- [23] D.A. Buchanan, A.D. Marwick, and D.J. DiMaria, and L. Dori, *J. Appl. Phys.* **76**, 3595 (1994)
- [24] B. Kaczer and J.P. Pelz, *J. Vac. Sci. Technol. B* **14**, 2864 (1996)
- [25] R. Ludeke, A. Bauer, and E. Cartier, *Appl. Phys. Lett.*, **66**, 730 (1995); *J. Vac. Sci. Technol., B* **13**, 1830 (1995)
- [26] M. Prietsch, A. Samsavar, and R. Ludeke, *Phys. Rev. B* **43**, 11850 (1991)
- [27] R. Ludeke, E. Cartier and H.J. Wen, *J. Electrochem. Soc.*, **96-1**, 580 (1996)
- [28] R. Ludeke, H.J. Wen and E. Cartier, *J. Vac. Sci. Technol., B* **14**, 2855 (1996)
- [29] H.J. Wen, R. Ludeke, D.M. Newns, and S.X. Lo, submitted to *J. Vac. Sci. Technol., B*
- [30] H.J. Wen, D.M. Newns, and R. Ludeke, submitted to *Phys. Rev. Lett.*
- [31] R.H. Good and T.J. Nelson, *Classical Theory of Electric and Magnetic Fields* (Academic Press, INC. N.Y., 1971)
- [32] D. J. DiMaria, E. Cartier and D. A. Buchanan, *J. Appl. Phys.*, **80**, 304 (1996).
- [33] D. J. DiMaria, private communications

Figure captions

Fig. 1. (a) Schematic representation of BEEM experiment on an MOS structure, (b) schematic energy band diagram of a charge-free MOS system at $V_{ox} = 0$. (c) energy band diagram of a MOS structure with a sheet of negative trapped charge in the oxide and under a positive oxide bias.

Fig. 2. BEEM spectra taken sequentially at the same sampling point of a Pd/SiO₂/p-Si structure. V_T ranged from -3 V – -6 V and $I_T = 2$ nA. It should be noted that only the range of -3.9 V – -5.5V of V_T is shown here. Threshold energies of the spectra are marked by vertical dotted bars.

Fig. 3. Charge induced threshold shifts as a function of electron kinetic energy $E_k = V_T - \Phi_{th}$. Both curves corresponding to sample 1 (circles) and sample 2 (squares) show a “soft” threshold at ~1.9 eV beyond which the BEEM thresholds again increase.

Fig. 4. Threshold shift as a function of applied oxide bias obtained from an area of 250×250 Å² where existing traps were filled up with electrons at $V_T = -6$ V. The area was sampled in a grid pattern of 36 spectra. The observed threshold shifts exhibited Gaussian distributions. The symbols correspond to the maximum (▲) and minimum (▼) threshold shifts, as well as to the distribution maximum (■) within a 36 spectral data set. The threshold shifts due to pure image force effects are also shown (●). The dotted curve was obtained with the sheet charge model presented in section III D. Two dotted vertical lines indicate three different regions of the field dependence.

Fig. 5. Threshold shift as a function of applied oxide bias obtained from an area of $250 \times 250 \text{ \AA}^2$ that was stressed by hot electrons with V_T up to -10 V. The area was sampled in a grid pattern of 36 spectra. The threshold shifts exhibited Gaussian distributions. Up and down triangles and circles correspond to the maximum and minimum threshold shifts and threshold shifts due to pure image force effects, respectively. The dotted curve was obtained with the sheet charge model presented in section III. D. Two dotted vertical lines indicate three different regions of the field dependence.

Fig. 6. Field-dependent barrier potentials calculated with the sheet charge model (eq. 3) for the saturated existing traps in a MOS structure with a 71 \AA oxide. The heavy vertical bars show the sheet charge placements necessary to explain the experimental field-induced threshold shifts of Fig. 4. Their resulting potentials are shown at the bottom as Φ_{fs} and Φ_{ps} that represent, respectively, full and partial screening at the O-S interface. Partial (dielectric) screening applies only for the dashed curve for $V_{ox} = -1 \text{ V}$; the solid curve assumes full screening.

Fig. 7. $750 \times 750 \text{ \AA}^2$ STM topography (a) and BEEM image (b) of a 40 \AA Pd/ 71 \AA $\text{SiO}_2/p\text{-Si}$ structure stressed by hot electrons with V_T of up to -10 V. Black-white range over the image is 32 \AA in topography, and 20 pA in BEEM. $V_T = -7 \text{ V}$, $I_T = 2 \text{ nA}$, $V_b = 0 \text{ V}$. The stressed area is seen as a lower transmission region of $\sim 320 \text{ \AA}$ diameter.

TABLE 1. Results from the sheet charge model for charge in an as-fabricated MOS structure, column 1, and charge generated by stressing, column 2. The dash line separates the model parameters of the pre-existing defects (top) from those of the generated defects. 3 sheets of charge are used to represent the distributions of each type of defects. σ (range) is the range of total charge density necessary to represent the maxima and minima distributions for pre-existing (Fig. 4) and generated defects (Fig. 5).

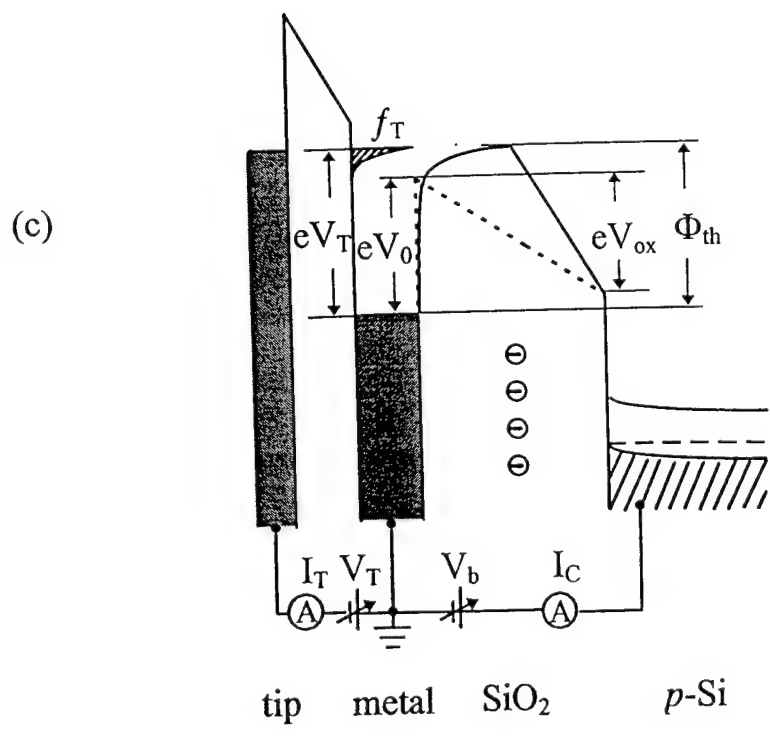
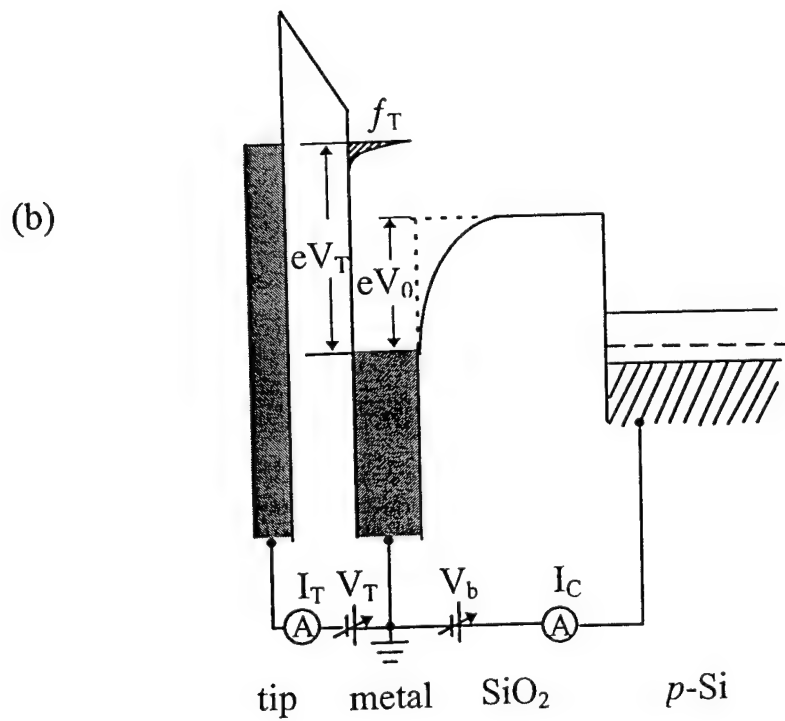
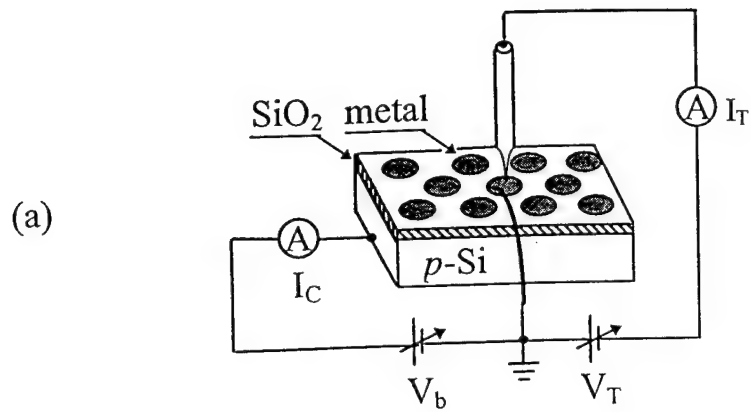


Fig. 1

Threshold shifts with scans of V_T from -3V to -6V

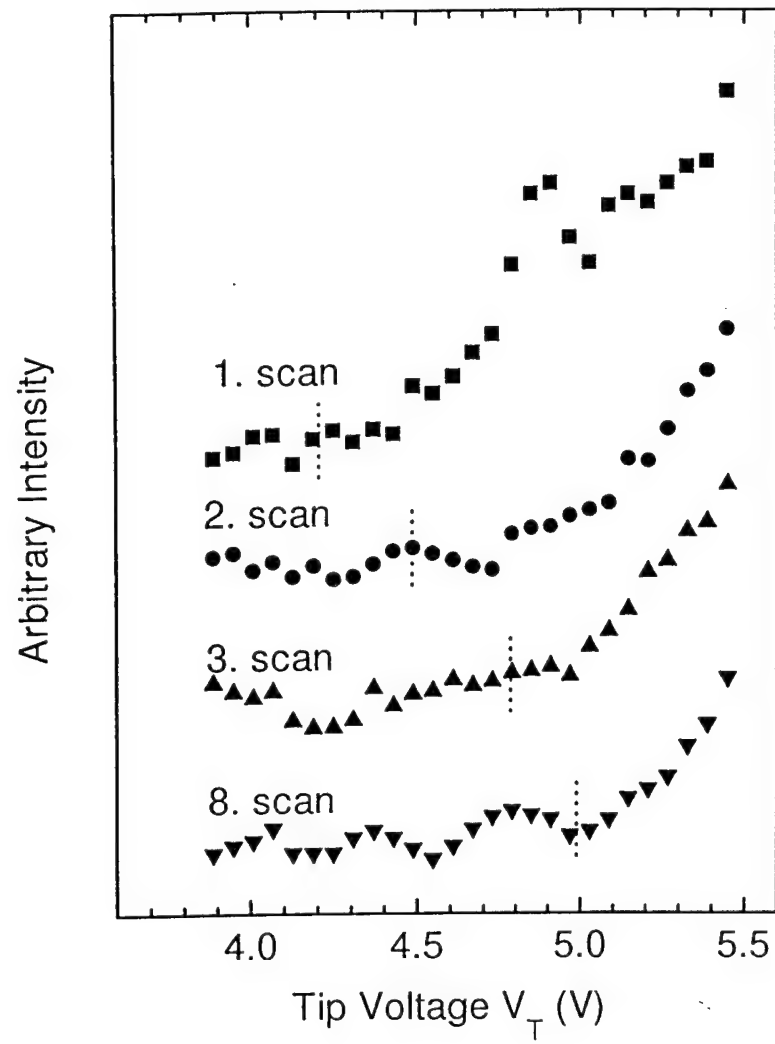


Fig. 2

Fig. 2

Charge induced threshold shifts for 71 Å SiO₂

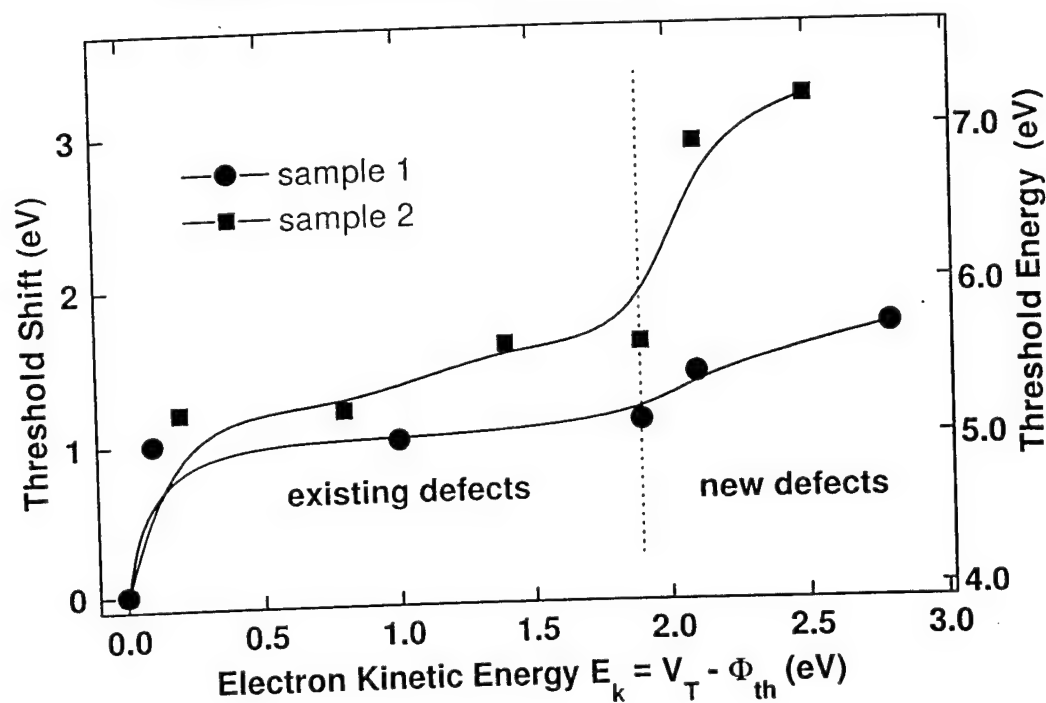


Fig. 3

Fig.

Field Dependent Threshold Shifts

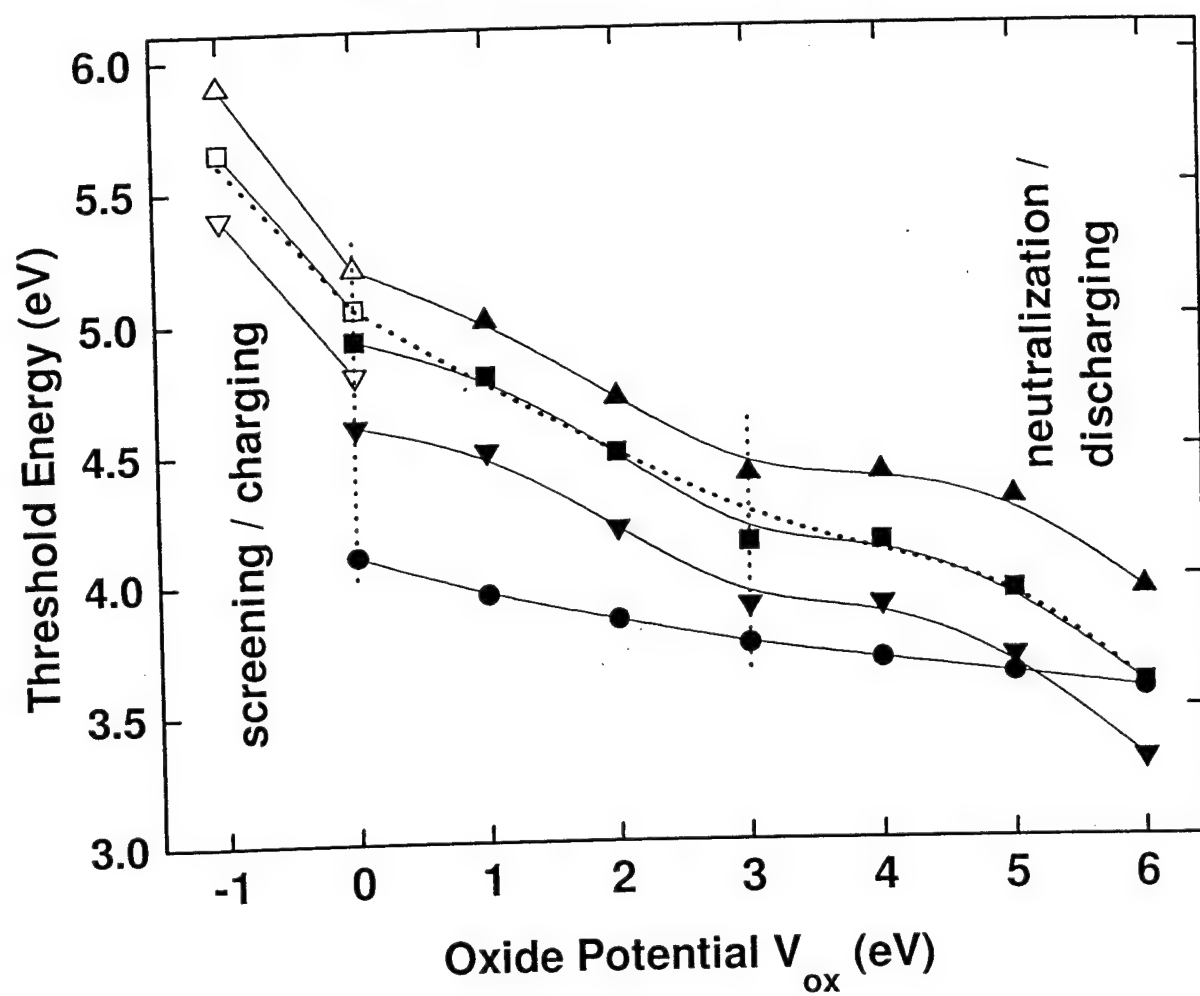


Fig. 4

Field Dependent Threshold Shifts

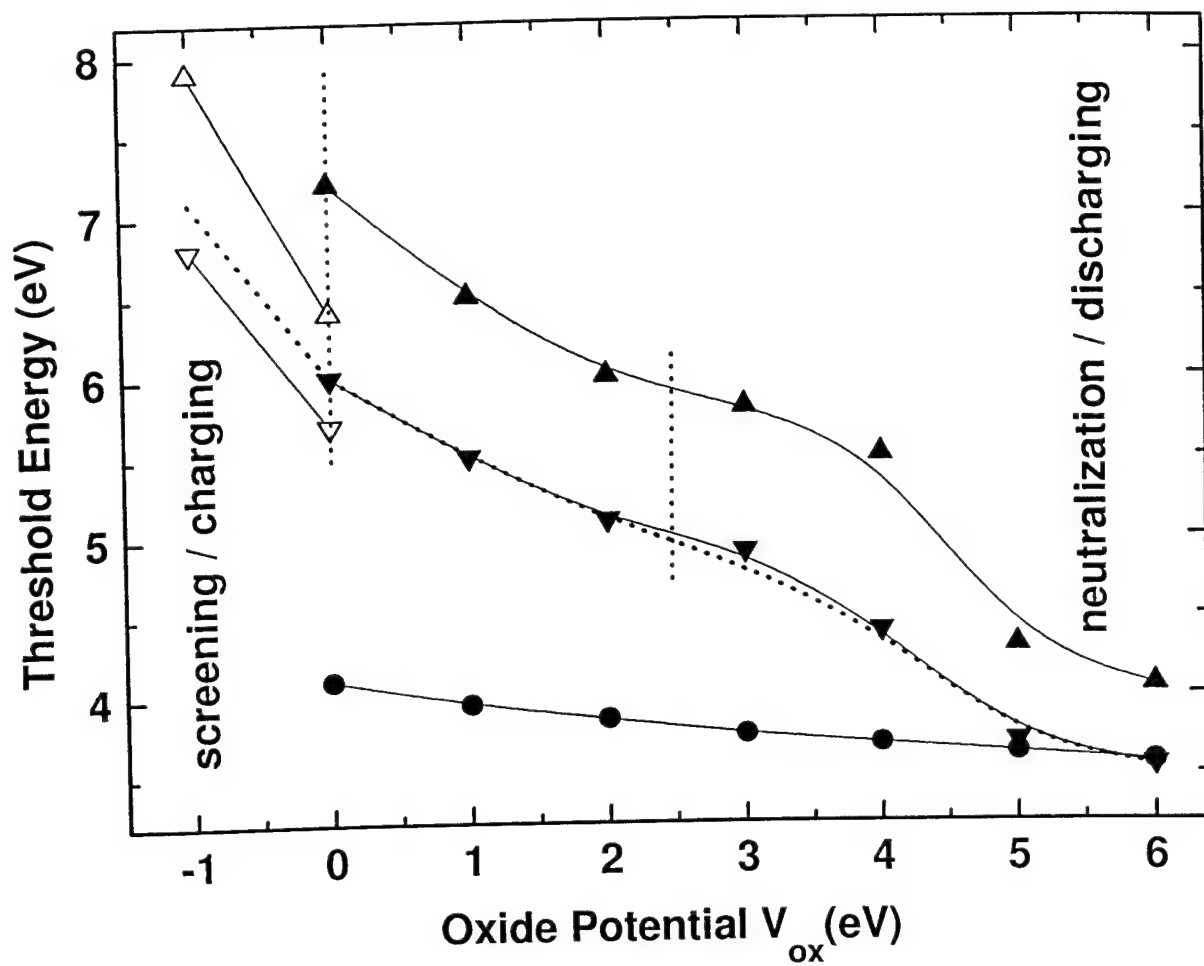


Fig. 5

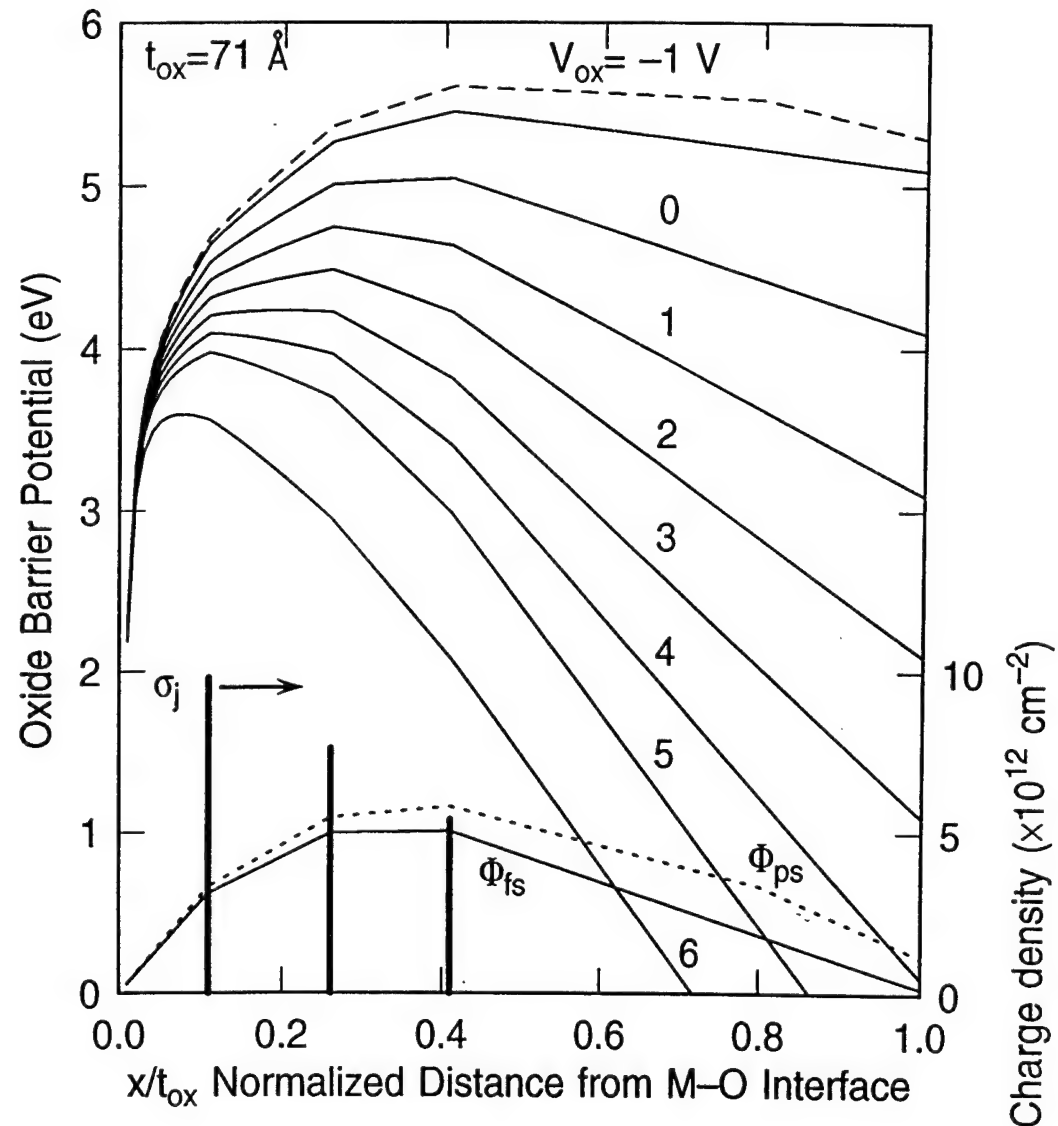


Fig. 6

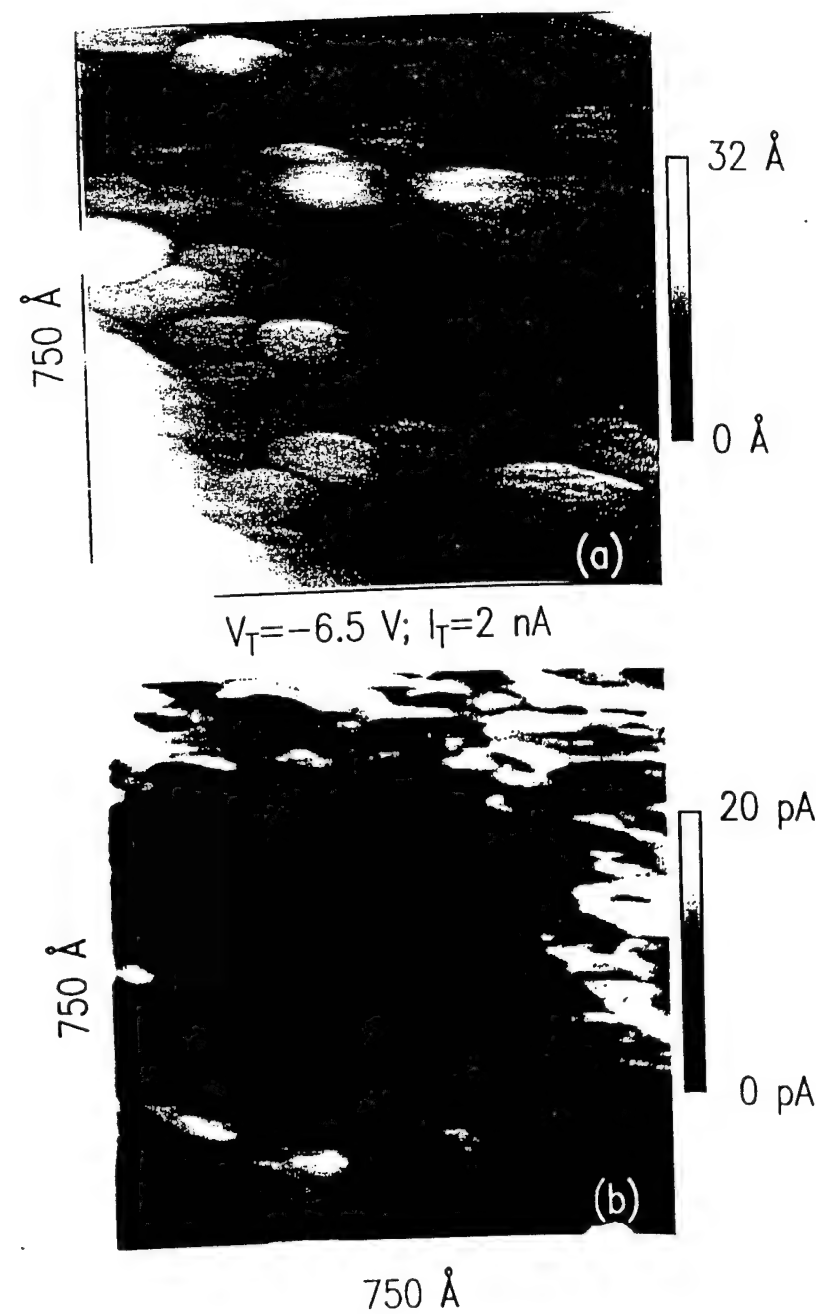


TABLE I.

	as-fabricated sample	stressed sample
σ_j (e/cm ²) $\times 10^{12}$	9.8, 7.6, 5.4	9.8, 7.6, 5.4
d_j/t_{ox}	0.11, 0.26, 0.41	0.11, 0.26, 0.41
σ (e/cm ²) (range)	(7-28) $\times 10^{12}$	(7-28) $\times 10^{12}$
<hr/>		
σ_j (e/cm ²) $\times 10^{12}$	----	6.6, 6.9, 5.8
d_j/t_{ox}	----	0.55, 0.70, 0.85
σ (e/cm ²) (range)	----	(19-36) $\times 10^{12}$

Localized electron trapping and trap distributions in SiO₂ gate oxides

R. Ludeke and H.J. Wen

IBM T.J. Watson Research Center, P.O. Box 218 Yorktown Heights NY, 10598, USA

(Received xx April 1997; accepted for publication dd mm 1997)

Localized trap filling and trap creation in SiO₂ were investigated by injecting electrons into metal-oxide-semiconductor structures with a scanning tunneling microscope. The resulting charging causes changes in the oxide potential that were studied as a function of an applied oxide field. The charge densities and charge distributions were obtained by modeling the field dependence of the potential arising from multiple sets of sheet charges in the oxide.

The distribution of trapped charge in the oxide layer of a metal-oxide-semiconductor (MOS) structure has been virtually impossible to determine with conventional transport methods on relatively thick oxides and only its centroid could be established.¹⁻³ We report here trapping in SiO₂ during electron injection with a scanning tunneling microscope (STM) and the determination of the trapped charge density and its distribution. Both pre-existing (process induced) and stress-generated traps were observed. The trapped charge strongly affects the local potential seen by the injected electrons, which is further modified by the combination of an applied oxide field and image force effects arising from the nearby interfaces (Schottky effect). We use Ballistic Electron Emission Microscopy (BEEM) in conjunction with the Schottky effect to probe the oxide potential. From model calculations of the potential and fits to experiment we then deduce the charge densities and distributions in the oxide.

In BEEM electrons are injected with a STM tip into the metal gate of a MOS structure. The tip bias V_T is referenced to the gate so that eV_T represents the kinetic energy of the electrons. A finite collector current I_C emerges from the Si substrate when $eV_T \geq eV_{th}$. eV_{th} is the threshold energy for electron transmission and corresponds to the potential maximum in the oxide relative to the Fermi level of the gate metal. An energy diagram of BEEM applied to a MOS structure in the presence of both a negative oxide charge and an applied positive bias V_b is shown in the inset of Fig. 1. For V_b 's used here, the boundary conditions at the oxide-semiconductor (O-S) interface require that the p-type Si substrate is in accumulation. For p-type Si and a Pd gate metal the intrinsic oxide potential $V_{ox} \approx V_b$ for the bias ranges used here.⁴ Details of the BEEM experiment are given elsewhere.³⁻⁵ Here we are only concerned with measuring V_{th} , which is obtained within an accuracy of ± 0.03 V from computer fits to the I_C vs V_T curves or BEEM spectra.⁶

The 71 Å SiO₂ layers used in this work were thermally grown near 800 °C in dry oxygen on 125 mm Si(100) wafers (boron doped to $\sim 10^{17}$ cm⁻³). No additional treatments were performed after the oxidation. $\sim 8 \times 15$ mm² pieces were cleaved from the wafer and covered with ~ 35 Å thick Pd dots, 0.2 mm in diameter, that were thermally evaporated through a shadow mask in ultra-high vacuum. The finished sample was then transferred under vacuum into the

STM chamber. Data were acquired in sets consisting of 6×6 spectra evenly spread over a $25 \times 25 \text{ nm}^2$ area.

Depending on prior electron beam exposure of the sampled area, thresholds varied spatially on a nanometer scale and by as much as 2 eV over a spectral set. These variations are attributed to electrons accumulated in traps of locally varying densities.^{4,7} The first spectrum on a virgin area of the sample always resulted in the lowest threshold (~4 eV), a value achieved subsequently only by moving to another spot ~10 nm away. Sampling a closer spot already revealed shifts that are attributed to partial filling of pre-existing traps by electrons scattered there from the prior injection. This assignment is based on the observation that for electron kinetic energies in the oxide $E_{\text{kin}} < 2 \text{ eV}$ (i.e. $V_T \leq 6 \text{ V}$) the shifts in a spectral set ceased to increase (saturate) after a few repeated scans over the $25 \times 25 \text{ nm}^2$ area. The observed saturation implies that the low energy electrons do not create any new traps, and that the newly filled traps must have pre-existed the measurement.

The approximate location of the charge can be deduced from the dependence of the thresholds on the applied oxide potential $V_{\text{ox}} \approx V_b$. It is easily ascertained from the inset of Fig. 1 that a change of δV_{ox} will result in a threshold change of $\delta V_{\text{th}} = x \delta V_{\text{ox}} / t$, where t is the oxide thickness and x the distance of the barrier maximum from the metal-SiO₂ interface.³ A set of 36 spectra was acquired over the charge-saturated area for each integral value of $0 \leq V_b \leq 6 \text{ V}$. Within such a set, the thresholds for the pre-existing traps varied over a 0.6 eV range that exhibited a bell-shaped distribution.⁷ This range reflects the local fluctuations in the charge density over the sampled area, with an estimated resolution of 2-3 nm.⁵ We show in Fig. 1, curve (b), only the thresholds for the pre-existing defects at the peak of their distribution. The extrema in the range of observed shifts exhibit nearly identical behavior, but are displaced by $\pm 0.3 \text{ eV}$.⁷ The spread in thresholds was reproducible at other charge-saturated areas of the sample, and thus corresponds to a range in charge densities that is characteristic of this oxide sample. As V_{ox} increases, the thresholds of curve (b) shift to lower energies. However, the shift is non-linear and shows a tendency to saturate prior to an additional drop for $V_{\text{ox}} > 5 \text{ V}$. For $V_{\text{ox}} = 6 \text{ V}$, V_{th} nearly corresponds to the value of an uncharged sample that is subject only to image force lowering (curve a).⁸ This indicates that the charge-saturated region has been temporarily neutralized at

the high bias condition, since upon returning to $V_{ox}=0$ (open symbol) V_{th} nearly assumes its original value. We attribute the neutralization to anode hole injection, a process that becomes very efficient when the electron energy in the SiO_2 exceeds 5 eV.⁹ For $V_b < 0$ (open symbols), the threshold increases at a rate larger than the rate one would expect by extrapolating the slope into the negative region. As will be discussed later, the added shift is assigned to a change in electron screening.

Threshold shifts of 1-2 eV were observed in addition to those attributed to charging of pre-existing traps for tip biases exceeding 6 V (i.e. $E_{kin} > 2$ eV),⁷ which indicates that new traps are being generated and filled by the hot electrons. The $E_{kin}=2$ eV value coincides with the formation threshold for trap generation attributed to the release of hydrogen near the SiO_2 -Si interface.¹⁰⁻¹³ To ascertain that trap generation was limited, we repeatedly scanned the 25×25 nm² area at tip biases as large as -10 V, $I_T=2$ na and $V_{ox}=0$, and measured the thresholds between scans. These stopped shifting after a few scans, indicating that electron trapping at the generated traps had reached saturation as well. The oxide field dependence was then measured. Due to additional scattering at the trap sites, the net collector current was rather weak and the mean value in the distribution became difficult to determine accurately. Hence we plot in Fig. 1, curve (c), only the minimum of the range of threshold shifts - the maximum lies ~1 eV higher.⁷ Curve (c) is shifted higher in energy by ~1 eV compared to curve (b) for the pre-existing defects, a clear manifestation of additional trapped charge in the oxide. The overall shapes of the two curves are similar, with a noticeably higher slope for curve (c), which indicates that the newly generated defects lie closer to the Si interface. The decrease in V_{th} for $V_{ox} > 3$ V, which ultimately coincides with that of curve (b) at 6 V, is due to increasing charge neutralization that we attribute again to anode hole injection. On returning to $V_b=0$ the traps refill within the first spectral scan (open symbols), but do not quite reach the value for the fully saturated traps. Changing V_{ox} to -1 V has an even more pronounced effect on the threshold shifts than observed for curve (b). A large fraction of this shift can be ascribed to changes in screening at the O-S interface.

We now proceed to model the trapped charge in the oxide by a series of equally spaced sheet charges, calculate their potentials subject to proper boundary conditions, sum up the potentials

and add the resulting defect potential to that of the oxide barrier. We then calculate the net barrier potential of the oxide and fit, by varying the charge density and location, the resulting field dependent potential maxima to the observed threshold shifts.

The charge injected into the oxide during the areal scans covers a roughly circular area of radius $R \sim 15$ nm that was deduced from the BEEM images (not shown). Due to the effective electron-phonon scattering in the SiO_2 , this area is larger than the scanned area.⁵ This charge is then modeled by j sheet charges of density σ_j that lie parallel both to each other and to the interfaces and are located at a distance d_j from the metal-oxide (M-O) interface. The potential $\phi_j(d_j - x)$ due to each sheet charge along the axial direction in a medium with dielectric constant ϵ_{ox} is given by:¹⁴

$$\phi_j(d_j - x) = \frac{\sigma_j \epsilon_{ox}}{2} \left\{ [(d_j - x)^2 + R^2]^{1/2} - |d_j - x| \right\} \quad (1)$$

The two interfaces restrain the potential to boundary conditions $\phi_j(d_j) = 0$ at the M-O interface, and $\phi_j(d_j - t) \approx 0$ at the O-S interface, which reflects that the Si is in accumulation there. We treat these boundary conditions by the method of images.¹⁵ Because of the two interfaces, the boundary conditions require multi-image charges, that is, image charges of image charges. The net potential per sheet charge is given by:

$$\Phi_j(x) = \phi_j(d_j - x) - \phi_j(d_j + x)$$

$$- \sum_{i=1}^k \rho^i [\phi_j(2it - d_j - x) - \phi_j(2it + d_j - x) - \phi_j(2it - d_j + x) + \phi_j(2it + d_j + x)], \quad (2)$$

Here $\rho = (\epsilon_s - \epsilon_{ox})/(\epsilon_s + \epsilon_{ox})$, with ϵ_s the effective dielectric constant at the Si interface. Under accumulation, with free carriers at the interface, $\epsilon_s \gg 11.8$, its bulk value, so that $\rho \approx 1$. In the absence of free carriers $\rho = 0.49$. The first two terms in eq. 2 are the sheet charge potential and its image across the M-O interface, the remainder are due to the presence of the O-S interface. The sum in eq. (2) was limited to $k=5$. The net potential of n sheet charges is: $\Phi_q(x) = \Phi_1(x) + \Phi_2(x) + \dots + \Phi_n(x)$. Potentials resulting from the combined two sets of sheet charges representing pre-existing defects (σ_d) and generated traps (σ_t), depicted respectively by solid and

outlined vertical bars, are shown in Fig. 2. The solid line labeled Φ_{fs} is for $\rho=1$ (fully screened at the O-S interface). The dashed line marked Φ_{ps} corresponds to $\rho=0.75$, that is, a screening intermediate between pure metallic and dielectric. Its drastic effect on the potential near the O-S interface is evident as the free carrier concentration is reduced at the interface, which nevertheless remains in accumulation (depletion was not studied due to a drastic increase in the noise as transmission becomes very weak for the higher barriers).

The total dynamic potential $U(x)$ seen by an electron injected from the gate is the sum of the "bare" oxide barrier eV_0 , the field effect $eV_{ox}x/t$, the dynamic image force lowering at the M-O and O-S interfaces, $e/16\pi\epsilon x$ and $ep/16\pi\epsilon(t-x)$ respectively, and Φ_q :

$$U(x) = eV_0 - \frac{eV_{ox}x}{t} - \frac{e}{16\pi\epsilon x} - \frac{ep}{16\pi\epsilon(t-x)} + \Phi_q(x). \quad (3)$$

Curves of $U(x)$ that incorporate both types of pre-existing (σ_d) and generated (σ_i) traps are shown in Fig. 2 for $-1 \leq V_{ox} \leq 6$ V. Their height is proportional to the charge density, with the scale shown on the right ordinate. The strength σ_j of each sheet charge and its position d_j were chosen to give a reasonable fit of the maximum of $U(x)$ to the experimental data of Fig. 1: First, σ_j and d_j were optimized to fit the data for the pre-existing defects, curve (b) in Fig. 1, using only the 5 sheet charges labeled by σ_d in Fig. 2 (their potential U is not shown). The increasing σ_j 's close to the M-O interface are necessary to duplicate the observed "softening" of the slope in the experimental curve (b) as V_{ox} increases. As discussed earlier, the lowering of the thresholds for $V_{ox}>4$ V is assigned to charge neutralization, which was simulated by reducing the σ_j 's to 35% of their saturated values for $V_{ox}>5$ V. The result of this modeling is shown by the dashed line overlying curve (b) in Fig. 1. Changes of order 10% in the net charge density resulted in inferior fits to the experimental data. Fits to experiment for the generated traps, Fig. 1(c), were made by keeping the identical distribution and charge density of the pre-existing traps and adding a second set of 7 sheet charges, labeled σ_i in Fig. 2, at positions and with densities indicated by the outlined bars. For the fits it was again necessary to simulate charge neutralization by reducing the σ_j 's for $V_{ox}>4$ V: the generated traps were empty for $V_{ox}\geq 5$ V with the pre-existing traps remaining partially filled (50% and 35% for 5 and 6 V, respectively). For $V_{ox}=-1$ V incomplete screening with $\rho=0.75$ (dotted curves in Fig. 2) gave a good fit to

experiment. Somewhat inferior fits were obtained with a reduced set of three sheet charges per trap type, which nevertheless required the same total charge density and distribution as for the larger set.

The following conclusions are derived from the model fits: i) The pre-existing defects are close to the M-O interface and exhibit a decreasing density away from the interface. From the spread in threshold fluctuations, their total density lies in the range of $(0.77 - 2.8) \times 10^{13} \text{ cm}^{-2}$. ii) The generated traps are located closer to the O-S interface, with a total density spread of $(1.9 - 3.6) \times 10^{13} \text{ cm}^{-2}$. iii) The unexpected threshold increases for negative V_{ox} are readily explained in terms of a decrease in free carrier screening at the O-S interface. iv) The threshold reductions under high bias are consistent with charge neutralization through anode hole injection

Further conclusions relate to the electron traps and their role in oxide breakdown.¹⁰⁻¹³ The observed charge saturation of the generated traps implies both that the number of trap sites is limited within a range of locally varying densities, and that their origin is extrinsic, that is, associated with defects/impurities that are activated by released hydrogen or other energetic particles. However, their observed densities still appear to be insufficient for local oxide failure, as attempts to cause breakdown in the stressed areas failed even after injecting $\approx 10^4$ Coul./cm² at $E_{kin} \approx 6$ V (this corresponds to a Fowler-Nordheim equivalent field of 13 MV/cm). Alternatively, their presence may be necessary with breakdowns occurring at other defect sites of much lower density. Of similar interest is the apparent unimportance of the process induced defects to the breakdown process, at least for the 7 nm oxides studied here, as breakdowns are seldom observed in BEEM stressing.⁵

We acknowledge fruitful discussions with D. DiMaria, D. Buchanan and E. Cartier. This research was partly supported by the Office of Naval Research, under Contract NO. N00014-95-C-0087.

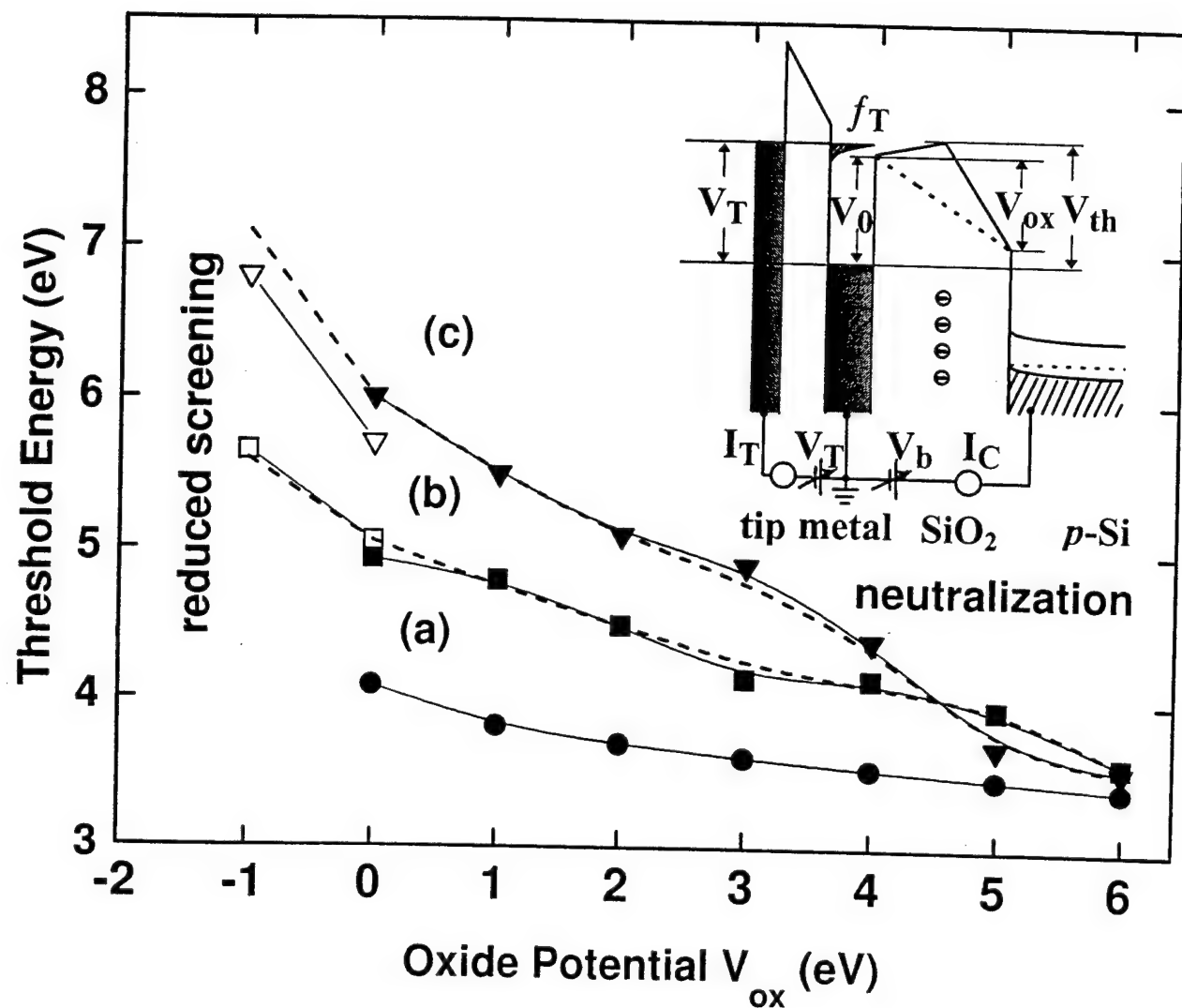
References

1. D. J. DiMaria, *J. Appl. Phys.* **47**, 4073 (1976).
2. E. H. Nicollian and J. R. Brews, *MOS Physics and Technology*, John Wiley, NY, 1982.
3. B. Kaczer and J. P. Pelz, *J. Vac. Sci. Technol.* **B 14**, 2864 (1996).
4. R. Ludeke, A. Bauer and E. Cartier, *Appl. Phys. Lett.* **66**, 730 (1995), *J. Vac. Sci. Technol.*, **B 13**, 1830 (1995).
5. R. Ludeke, H.J. Wen and E. Cartier, *J. Vac. Sci. Technol.* **B 14**, 2855 (1996).
6. R. Ludeke and A. Bauer, *Phys. Rev. Lett.* **71**, 1760 (1993).
7. H.J. Wen and R. Ludeke, *J. Vac. Sci. Technol.* **B 15**, July/Aug. 1997, in press.
8. H.J. Wen, R. Ludeke, D. M. Newns and S.H. Low, *J. Vac. Sci. Technol.* **A 15**, 784 (1997).
9. D. J. DiMaria, E. Cartier and D. A. Buchanan, *J. Appl. Phys.* **80**, 304 (1996).
10. E. Harari, *Appl. Phys. Lett.* **30**, 601 (1977).
11. D. J. DiMaria and J. W. Stasiak, *J. Appl. Phys.* **65** 2342 (1989).
12. D. J. DiMaria, E. Cartier and D. Arnold, *J. Appl. Phys.* **73**, 3367 (1993).
13. D. A. Buchanan, A. D. Marwick, D. J. DiMaria and L. Dori, *J. Appl. Phys.* **76**, 3595 (1994).
14. R. H. Good and T. J. Nelson, *Classical Theory of Electric and Magnetic Fields*, Academic Press, NY, 1971.
15. J. D. Jackson, *Classical Electrodynamics*, John Wiley, NY, 1962.

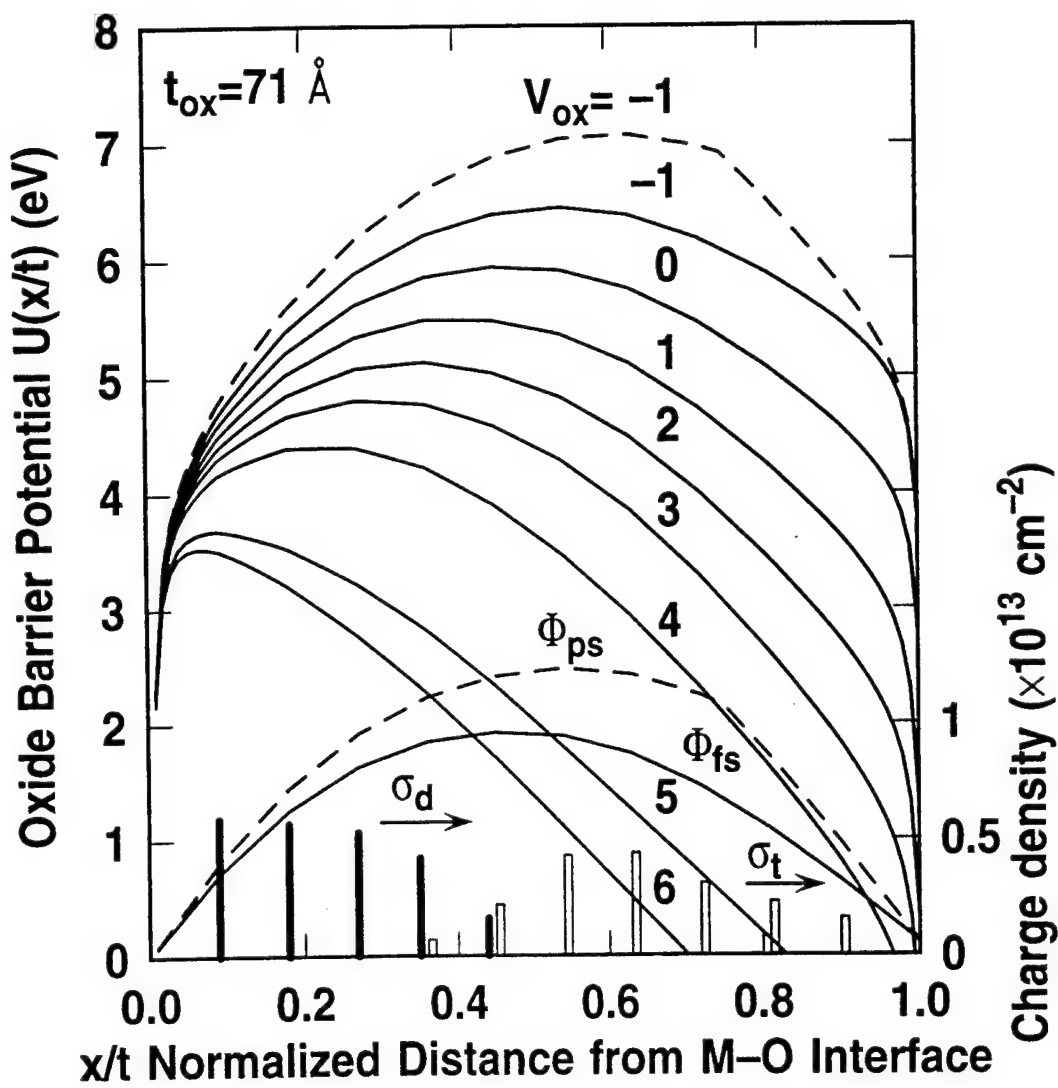
Figure Captions

FIG. 1. Field dependent threshold shifts for a Pd/ 71 Å SiO₂/p-Si(100) sample: (a) for a charge free sample (only image force lowering); (b) for charge-saturated pre-existing traps; (c) for charge-saturated pre-existing traps and stress induced traps. Inset shows an energy diagram of the BEEM experiment. Curve (a) was obtained from field dependent measurements on virgin areas of MOS structures.⁸

FIG. 2. Barrier potential U(x) as a function of applied oxide bias V_{ox}. The curves labeled Φ_{fs} and Φ_{ps} are the potentials for the oxide charge assuming full and partial screening, respectively. The topmost broken curve for V_{ox}=-1 V includes Φ_{ps} , the solid one beneath it includes Φ_{fs} . Sheet charge locations and densities reflected in the potentials Φ are marked by vertical bars. The density scale is on the right.



Ludtke & Wen New Fig. 1



Atomic-scale studies of electron transport through MOS Structures

H.J. Wen, R. Ludeke, D.M. Newns, S.H. Lo and E. Cartier

IBM T. J. Watson Research Center, P.O. Box 218, Yorktown Heights, New York 10598

The STM-based Ballistic Electron Emission Microscopy/ Spectroscopy (BEEM/BEES) in conjunction with theoretical modeling and Monte Carlo simulations are used to clarify intrinsic transport issues in Metal-Oxide-Semiconductor (MOS) structures. Compared to conventional MOS transport studies, BEEM/BEES offers unique advantages that include, besides its unsurpassed spatial resolution, independent control over the energy of the electrons, which thereby can be injected directly into the SiO_2 conduction band, as well as complete control over the electric field across the oxide. The MOS samples consist of thin Pd "gate" dots deposited on 7-15 nm device-grade oxides thermally grown on Si(100). BEES measures the threshold energy for electron transmission over the potential barrier determined by the gate metal and oxide. This potential is strongly affected by the combination of screening effects due to the metal gate and an applied oxide field. Field dependent decreases of the injection thresholds follow classical image force theory, through which we have determined a dielectric response of $\epsilon_{\text{ox}} = 2.74$ for electrons in SiO_2 . Possible contributions to the threshold shifts from field induced tunneling through the oxide barrier were assessed with a WKB calculation and deemed unimportant. Justification for the measured $\epsilon_{\text{ox}} = 2.74$, as opposed to the "established" value close to the optical dielectric constant of 2.15, is obtained from a novel theoretical model. The model, based on a classical particle subject to a time-dependent potential in a polarizable medium, predicts a dynamic dielectric response in the oxide to a moving charge near the metal interface of $\epsilon_{\text{ox}} = 2.69$. The image force induced distortion of the potential near the metal gate has a pronounced effect on the dynamics of the electrons reaching the oxide. Monte Carlo simulations show that this distortion strongly affects the phonon scattering rates in the immediate interface region. Energy and oxide-field dependent electron transmission probabilities were obtained from the simulations and were found to agree remarkably well with experimentally determined probabilities.

I. INTRODUCTION

Field assisted barrier lowering due to image force effects has a controversial history in its application to transport physics in MOS structures, although this concept is well established in condensed matter physics [1]. In modeling of electron transport across a dielectric, image force effects are generally ignored, in particular when tunneling, either direct or Fowler-Nordheim, is part of the process [2-3]. A further contribution to a lower effective barrier may result from electrons tunneling through the barrier [1]. However, the tunneling induced barrier lowering is usually small in nondegenerate semiconductors, as well as in relatively thick insulator layers. The image force induced barrier lowering (image force lowering) was traditionally determined by internal photoemission measurements [4-6]. From the observed barrier lowering as a function of the applied electric field an effective dielectric constant can be derived, often called the image-force dielectric constant. With this technique, barrier heights between metal/SiO₂ and Si/SiO₂ interfaces and their field dependencies have been studied [5-6]. In these studies, an image-force dielectric constant of $\epsilon_{ox} = 2.15$, equal to the optical dielectric constant in SiO₂, was determined, a value that has been accepted ever since [7-8]. Arguments supporting that value were based on the transit time (τ) that an electron needs to move from the MO interface ($z = 0$) to the potential maximum ($z = z_m$). In the case of Si the transit time was deduced to be between 1×10^{-14} s and 5×10^{-15} s and it was argued that the image-force dielectric constant should be comparable to the dielectric constant for electromagnetic radiation of these periods. A corresponding value equal to the static dielectric constant of 12 was determined, which agreed with the value obtained by internal photoemission measurements [1]. This somewhat fortuitous agreement results from the nonpolar nature of Si, whose dielectric constant is essentially constant for electromagnetic

radiation from dc to $\lambda = 1 \mu\text{m}$ [9]. In contrast, SiO_2 is a polar material, whose optical phonon modes result in strong variations of the dielectric constant in the range of $\lambda = 40$ to $4 \mu\text{m}$ [9]. In this case a transit time of $5 \times 10^{-15}\text{s}$, which corresponds to $\lambda = 1 \mu\text{m}$, should correspond to a dielectric constant at optical frequencies, i.e. 2.15. It should be noted that a response characterized by the optical dielectric constant means that the lattice polarization of the medium (optical phonons) can not follow the moving electron; in other words, the particle moves so fast that the electron-phonon interaction does not occur. Consequently, the moving electron senses a stronger image force than at rest. In the authors' opinion, the traditional transit time argument that the image-force dielectric constant should be comparable to the dielectric constant for electromagnetic radiation of the period equal to the transit time lacks physical justification. In the following it will be concluded that the transit time is not a measure for predicting a dielectric response. In order to know how the dielectric medium responds to a moving electron, one needs to consider contributions of optical phonons in SiO_2 .

In this work, we use Ballistic Electron Emission Microscopy (BEEM) as a new technique to study the field dependent barrier lowering at the Pd/ SiO_2 interface of MOS structures. We readdress these issues and demonstrate that i) image force effects are important in MOS transport and cannot be explained by alternative processes such as tunneling; ii) the effective dielectric response to a moving charge lies in between the optical $\epsilon_{\text{opt}} = 2.15$ and the static $\epsilon_{\text{st}} = 3.9$; iii) a theory based on classical concepts gives a dielectric response close to experiment, and provides new insights to its origin, which is determined by the mean velocity rather than the transit time of the moving electron. A further consequence of image force effects is a decrease in the electron transmission probabilities at the MO interface.

II. EXPERIMENTAL DETAILS

A. Ballistic Electron Emission Microscopy (BEEM)

BEEM is an STM-based microscopy/spectroscopy that differs from the conventional STM mode by the presence of a thin metal electrode overlying the semiconductor structure to be measured, as shown in Fig. 1(a). The sole purpose of this electrode is to supply a conductive ground plane relative to which the STM tip is biased. In our studies hot electrons were injected from the tip into Pd/SiO₂/Si MOS structures. An energy band diagram for the present BEEM experiment is shown in the Fig. 1 (b). The tip bias V_T is referenced to the thin grounded metal film (the metal Fermi level is defined to be the zero potential). Therefore eV_T is a direct measure of the kinetic energy of the electrons injected into the metal. Provided that the metal film thickness is of the order of the electron scattering length in the metal, most of the electrons will traverse the metal ballistically to reach the far interface. It should be noted here that no features in the BEEM spectra have been attributed to the metal layer, except for causing a featureless attenuation of the injected electrons. Therefore transmission across the metal is assumed to be independent on the electron energy, a justifiable assumption over an energy range for which the mean free paths are larger than the metal thickness. Electrons with sufficient energy to overcome the potential barrier at the Pd/SiO₂ interface may ultimately reach the semiconductor conduction band, and emerge from the semiconductor as a collector current I_C . For an increasing magnitude of the tip bias V_T , I_C is zero until V_T reaches a threshold (V_0), a value equal to the interface barrier height. The value of V_0 is usually extracted from the spectra by means of a model fit. A separate gate bias (V_b) between the metal and semiconductor can also be readily applied within the BEEM configuration. This allows complete control over the field in the oxide and facilitates

field-dependent transport studies. As V_b affects both the potential drop across the oxide (V_{ox}) and the band bending of the Si at the $\text{SiO}_2\text{-Si}$ interface, their relationship is nonlinear and is obtained by solving the appropriate Poisson equation with the assumption of a negligible density of interface states [7,10]. In addition, V_{ox} also includes a part of the built-in potential of 0.50 V due to the work function difference between the metal and the semiconductor. In the present case, the work function of Pd is larger than that of n-type Si, therefore the flat band ($V_{ox} = 0$) condition requires a negative gate bias proportional to the work function difference.

B. Sample preparation

Device quality oxide layers were thermally grown near 800 °C in dry oxygen on 125 mm diameter Si(100) wafers doped in the low 10^{17} cm^{-3} range. No additional treatments were made after oxidation. Here we report studies on oxides with thicknesses of 75 Å and 150 Å; the thicknesses were determined with an ellipsometer. Approximately $2 \times 12 \text{ mm}^2$ pieces were cleaved from the wafers and introduced into an UHV sample preparation chamber, where Pd dots, 0.2 mm in diameter, were thermally evaporated through a shadow mask. The Pd deposition was made with the Si substrate held at a temperature of about 30 K, which was necessary to produce smooth continuous surfaces by inhibiting surface diffusion. The resulting roughness was about 10 Å for a Pd film of thickness of 35 Å. After evaporation the sample was allowed to warm up to room temperature and was subsequently transferred under UHV into the STM chamber, where the BEEM grounding contact was gently positioned onto a selected Pd dot by means of three orthogonally mounted Inchworms. MOS structures with leakage resistance $\geq 10^{12} \Omega$ were generally suitable for our studies. All data were taken in the conventional, feedback-controlled

constant tunnel current (I_T) mode. For each V_b a set of typically 16-25 spectra were taken in a grid pattern covering an area of $250 \times 250 \text{ \AA}^2$. The BEEM data reported here are generally averages over approximately 10 similar spectra. Additional information about the STM and data acquisition can be found elsewhere [11]. Within a given set of spectra variations in the threshold of up to several tenth of a volt were observed, which are assigned to negative charge at the SiO_2 -Si interface region [12-13]. The spectra presented here were averaged over those that exhibited a common, lowest threshold in a given set of spectra.

III DATA INTERPRETATION

A. Classical image force theory

When an electron crosses the MO interface and enters the oxide, it experiences an attractive force of its own positively charged mirror-image with respect to the interface plane at $z = 0$, and therefore has an additional negative potential energy term. The application of a voltage V_{ox} across the metal and silicon further modifies the potential between the metal and the SiO_2 conduction band minimum, as shown in Fig. 1 (b). Within classical image force theory, the

combined potential is given by $\Phi_{im}(z) = eV_o - eV_{ox} \frac{z}{t_{ox}} - \frac{e^2}{16\pi\epsilon_0\epsilon_{ox}z}$; the barrier lowering δeV_o

with increasing V_{ox} and the barrier position z_m are given by:

$$\delta eV_o = \left[\frac{eV_{ox}}{4\pi\epsilon_0\epsilon_{ox}t_{ox}} \right]^{1/2} eV; \quad z_m = \left[\frac{et_{ox}}{16\pi\epsilon_0\epsilon_{ox}V_{ox}} \right]^{1/2} \quad (1a,b)$$

where ϵ_0 is the permittivity of free space, ϵ_{ox} is the effective dielectric constant of SiO_2 , and t_{ox} is the oxide thickness. In the absence of an oxide charge, the effective barrier height is given by

$eV_{th} = eV_o - \delta eV_o$; V_o represents the interface barrier height at flat band conditions, as indicated in Fig. 1(b). Eq. (1a) represents a straight line provided that the effective dielectric constant ϵ_{ox} has a single value over the considered field range. In turn, ϵ_{ox} and the linear relationship (a validity test of the classical image force) can be defined from the experimentally determined barrier lowering δeV_o as a function of the applied oxide potential, as presented in the following.

B. Experimental observation of image force lowering in barrier heights: $\epsilon_{ox} = 2.74$

Representative spectra for a 75 Å oxide MOS structures are shown in Fig. 2 for various positive oxide biases. Both the applied bias V_b and the resulting potential drop V_{ox} across the oxide are indicated on the figure. The spectra are characterized by a rapid increase in I_T beyond the threshold near 4 V, followed by a saturation, then a decrease, which in turn is followed by a second increase for $V_T > 8$ V. The decrease in I_T at ~ 2 V above threshold is evidence for the onset of acoustic phonon scattering in the oxide and is a clear manifestation of the importance of this scattering mechanism in oxide transport [10,14]. At these energies, the strong momentum randomizing phonon collisions cause the electrons to scatter back into the metal. The momentum relaxation rates level off at higher energies and the collector current again increases because the density of states, i.e. the available phase space, is increasing. Optical phonon scattering is important only near threshold. With increasing oxide bias V_b , the spectra clearly show a shift to low energy as well as an increase in absolute intensity. The increase in intensity is attributed both to an increase in the transmission probability in the oxide due to the positive bias [10], and to increases in available phase space due to the image force induced barrier lowering. In this section

we will only concentrate on the threshold shifts (barrier lowering). The observed barrier lowerings derived from the spectra of Fig. 2 are plotted as a function of $V_{ox}^{1/2}$ and are shown by solid circles in Fig. 3. We clearly see that the experimental data are distributed along a straight line, a strong manifestation of the validity of the classical image force theory. These threshold values were obtained by fitting the BEEM data with a simulated spectrum of the current in the vicinity of the threshold region ($V_0 \pm 0.5$ eV) [10]. The simulation is based on the assumption that the transmission probability in the oxide is constant and field independent over the considered threshold region. The latter assumption implies that quantum mechanic contributions to the transmission probability, which are included in our theoretical BEEM spectrum, are also relatively field independent, an assertion supported by the excellent agreement between experiment and Monte Carlo simulated oxide transmission probabilities for positive oxide fields [10]. In order to determine the threshold energy, the experimental data were visually fitted by varying only the threshold energy and the intensity prefactor over the energy window, with emphasis on an excellent fit on the steeply rising part of the spectrum just above the threshold. Since this portion of the spectrum is devoid of any contributions from electrons tunneling through the barrier, we speculate that the determined threshold energy is not influenced by tunneling contributions, a conclusion supported by the excellent agreement of the threshold energies with classical image force theory, as well as by calculations based on the WKB approximation that is demonstrated in detail in the next section. The fit to the data can be made to within ± 0.02 eV, as marked in the figure. It should be noted that the right axis scale for the threshold is only in reference to the experimental data (solid circle), while the left axis (image force lowering relative to the flat band condition in the oxide) is valid for all curves.

Since the barrier lowering exhibits a linear behavior, a least-square linear fit with a chi value of only 0.0022 was made to the data, as shown in Fig. 3. From eq. (1a), the slope of the fitted line is equal to $\left[\frac{e}{4\pi\epsilon_0\epsilon_{ox}t_{ox}} \right]^{1/2}$, with ϵ_{ox} as the only adjustable parameter, whose value is determined to be 2.74 ± 0.11 . This uncertainty was estimated from the error range in the data. This value is considerably larger than the optical dielectric constant (2.15) and lies in between it and the static value (3.9). In the following, we demonstrate through a model calculation that $\epsilon_{ox} = 2.74$ is more accurate in describing the dielectric response than the optical one, though, that value is supported by internal photoemission results [5,6,15]. It should be noted that the fitted curve originally missed the origin, which indicates that our initial estimate of $V_{ox} = 0.45$ V for zero bias was off by 53 mV. Accordingly, the V_{ox} values for the data were uniformly shifted by this amount. The fitted curve must go through the origin, since at zero field ($V_{ox} = 0$) the barrier height is the same in the presence or absence of the image force potential. By extrapolating to $V_{ox} = 0$ V, a threshold value of 4.08 ± 0.02 eV is deduced for the Pd-SiO₂ potential barrier V_o under flat band conditions.

C. Assessment of tunneling contributions

Before we present the theoretical model describing the dynamic dielectric response, we need to clarify the issue whether or not the observed barrier lowering include contributions from electrons tunneling through the barrier. It is in principle possible that electron tunneling contributes to the observed barrier lowering, even though the described determination of the threshold does not include a tunneling current. We state two facts to conclude that a tunneling

contribution to the determined barrier lowering is negligible: (a) the barrier lowering clearly show a linear dependence on the square root of the oxide bias $V_{ox}^{1/2}$, a result valid only within the classical image force theory, since a tunneling contribution would give a nonlinear behavior; and (b) theoretical results based on the WKB approximation exclude any substantial contributions for tunneling electrons in the determination of the BEEM thresholds. It should be kept in mind that the latter correspond to electrons going over the barrier at nearly unit transmission probability, whereas that for tunneling electrons diminishes exponentially rather rapidly for energies below the barrier maximum. These concepts were quantified and the results are presented by dotted lines in Fig.3. The approach taken here is to assess the field dependence of tunneling electrons at a given transmission probability. Unlike standard tunnel current calculations for MOS capacitor structures, the tunnel current for BEEM experiments cannot be calculated analytically due to the complexity of hot electron scattering processes in the metal and at the interfaces. Calculations were carried out with and without the inclusion of image force lowering, as well as for the various $\epsilon_{ox} = 2.15, 2.74$ and 3.90 values. An electron effective mass at the bottom of the conduction band of $0.5 m_0$ (m_0 is the electron rest mass) was used [8]. No strong dependence on the mass, although varied from $0.3 m_0$ to $0.5 m_0$, was observed. The singularity of the image force potential at the interface ($z = 0$) was removed by assuming $\Phi_{im}(z) = 0$ for $\Phi_{im}(z) \leq 0$. Tunneling probabilities were calculated as a function of tip voltage for various oxide biases. A virtual threshold energy can be set at a certain tunneling probability, then barrier lowering relative to the zero field case can be plotted as a function of $V_{ox}^{1/2}$. The tip voltages at the tunneling probability of 50 % are plotted by dotted lines in Fig. 3. The three upmost lines were calculated with $\epsilon_{ox} = 2.15, 2.74$ and 3.90 ; the bottom curve was obtained by excluding the

image force potential altogether. First of all, it is clearly seen that the bottom curve deviates considerably from the experimental data, which allows us to conclude that the image force potential plays the main role in the observed barrier lowering. Second, the theoretical curves are nonlinear, a behavior that increases with increasing bias and becomes even more dominant for lower tunneling probabilities. We argue that the absence of such deviations from linearity in our data precludes substantial contributions of tunneling in our methodology of determining thresholds. This statement does not mean that tunneling is absent, but rather that its contributions below threshold are inconsequential to the determination of the threshold. This is attributed to the rapid increase of phase space for transmission above threshold that determines entirely the collector current behavior on which the threshold were fitted. For a tunneling probability of 100% the calculated results exhibit the expected linear behavior that exactly matches solutions of the classical image force theory for all three values of ϵ_{ox} . Therefore we conclude that the observed barrier lowering are solely attributed to the image force potential, with an effective dielectric constant of 2.74. It should be noted that Monte Carlo calculation by Fischetti et al [16] lead to similar conclusions.

D. Classical calculation of the retarded phonon field: $\epsilon_{ox} = 2.69$

In order to understand the origin of the experimentally determined $\epsilon_{ox} = 2.74$, we present a theory based on classical concepts to calculate the effective dielectric constant for an electron in a model BEEM experiment.

In the model, the electron moving in SiO_2 as a classical particle with trajectory $\vec{r}_e(t)$ and charge q produces a potential $V(\vec{r}, t)$. We calculate $V(\vec{r}, t)$ and then obtain the force acting back

on the particle at $\bar{r} = \bar{r}_e$. The dielectric medium is assumed uniform with a local dielectric response. The presence of the metal/dielectric interface is taken into account by introducing the image of the particle. Then all potentials in the left-hand half space ($z < 0$) are automatically zero when we define the potential on the plane ($z = 0$) to be zero. We start from the formula [17]

$$V(\bar{r}, t) = V^0(\bar{r}, t) + \frac{1}{4\pi\epsilon_0} \int d^3 r' \bar{P}(\bar{r}', t) \bullet \nabla_{r'} \frac{1}{|\bar{r} - \bar{r}'|} \quad (2)$$

where $V(\bar{r}, t)$ is the total potential, $V^0(\bar{r}, t)$ the external potential caused by the particle and its image in vacuum, switched on at $t = 0$; and $\bar{P}(\bar{r}, t)$ is the induced polarization in the dielectric medium defined through the local polarizability $\alpha(t - t')$:

$$\bar{P}(\bar{r}, t) = -\epsilon_0 \int_0^t \alpha(t - t') \nabla V(\bar{r}, t') dt' \quad (3)$$

MKS units are used throughout. Using Green's theorem, eq. (2) becomes

$$V(z, t) + \frac{1}{\epsilon_0} \int_0^t dt' \alpha(t - t') V(z, t') = V^0(z, t) \quad (4)$$

where \bar{r} is replaced by z , since the particle in our case is traveling along the z -axis. Eq. 4 is solved by taking its Laplace transform, giving $\bar{V}(z, p) = \bar{V}^0/[1 + \bar{\alpha}(p)]$. $\bar{\alpha} = \alpha_{opt} + \alpha_{ph}$ is the sum of the optical response, independent of p , and phonon response $\alpha_{ph} = g\omega_{ph}^2/(p^2 + \omega_{ph}^2)$, where g is the phonon coupling strength. Through the frequency dependent dielectric function $\epsilon(p) = \epsilon_{st} + \epsilon_{opt} \equiv 1 + \alpha_{opt} + \alpha_{ph}$, it can readily be shown that $g = \epsilon_{st} - \epsilon_{opt}$. After suitable substitutions and inverse Laplace transformations, one finally obtains:

$$V(z, t) = -\frac{1}{\epsilon_0 \epsilon_{opt}} \left[\frac{q}{z + z_e(t)} \right] + \left(\frac{\epsilon_{st} - \epsilon_{opt}}{\epsilon_0 \epsilon_{st} \epsilon_{opt}} \right) \int_0^t \omega^2(t-t') e^{-\omega(t-t')} \left[\frac{q}{z + z_e(t')} \right] dt' \quad (5)$$

where the phonon response is described by $\alpha(t) = \omega^2 t e^{-\omega t}$. The latter is obtained from the Fourier transform of the probability distribution $w(x) = 4\omega^3 x / \pi(x^2 + \omega^2)^2$, and represents a Debye-like power law behavior at low frequencies with a high frequency cutoff, the simplest form of a broadened phonon spectrum short of the actual multi-mode distribution. For SiO₂ the higher lying optical mode ($\omega_{ph} = 0.153$ eV [9]) was assumed to represent the oxide, $\epsilon_{st} = 3.9$ and $\epsilon_{opt} = 2.15$. Since acoustic phonons are not polarizable, they do not contribute to the image force field. It must be noted that the first term in eq. 5 represents only the image term of the external potential and a self energy term representing the quantum mechanical polaron cloud surrounding the particle is not included in eq. 5, since the particle is treated classically. The integral term represents the effect of electron-phonon interaction over a time period t. Since the phonons are described by harmonic oscillators without damping, the electron-phonon interaction does not transfer any energy from the electron to the dielectric. The total energy of the electron is thus conserved. The equation of motion is obtained by differentiating V(z,t) w.r.t. z and setting z to z_e:

$$-m \frac{d^2 z_e}{dt^2} = -\frac{V_{ox} q}{t_{ox}} + \frac{1}{16\pi\epsilon_0 \epsilon_{opt}} \left[\frac{q^2}{r_0^2 + z_e^2(t)} \right] - \left(\frac{\epsilon_{st} - \epsilon_{opt}}{4\pi\epsilon_0 \epsilon_{st} \epsilon_{opt}} \right) \int_0^t \omega^2(t-t') e^{-\omega(t-t')} \left[\frac{q^2}{[z_e(t) + z_e(t')]^2 + 4r_0^2} \right] dt' \quad (6)$$

We have included here a softening factor r₀ in the image force term to avoid the singularity at z_e = 0. Its value r₀ = 1.33 a.u. was chosen so that the peak in V(z,t) relative to the Fermi level in the

metal equals V_0 ($\approx 4V$). It should be noted that the integral term explicitly represents the electron-phonon interaction force. The differential equation is run until the critical velocity v_c , and hence critical kinetic energy ($E_c = \frac{1}{2}mv_c^2$) is determined for the particle to just cross the barrier. The results are demonstrated in Fig. 4. Two masses, $m = m_0$ and $0.5m_0$, were used in order to assess the sensitivity of the mass on the results. The numerical results, again plotted against $V^{1/2}$, exhibit a nearly linear behavior, in good agreement with the classical image force theory. From the slope in the case $m = m_0$, which is close to the SiO_2 conduction band mass [18], an effective dielectric constant $\epsilon_{ox} = 2.69$ was obtained. This value is in very good agreement with the experimental value 2.74.

The measured and calculated value for $\epsilon_{ox} \approx 2.7$ is incompatible, as mentioned earlier, with the transit time argument. Based on the above considerations we know that the integral term (phonon contributions) is the underlying cause for the increase of ϵ_{ox} from 2.15 to 2.69. Another critical issue in this matter is that ϵ_{ox} is essentially constant over the field range of ~ 0 to 9 MV/cm. In order to gain more insights into these issues, we further simplify the integral term in eq. (6) to an average force exerted by the phonons on the electron over the transit time, that is $\propto \omega_{ph}^2 / \bar{v}_{el}^2$, with \bar{v}_{el} defined as the electron mean velocity. This simplified term tells us that the strength of phonon contributions is dependent on the electron mean velocity rather than the transit time. Over the applied range of V_{ox} the variations in V_{th} are relatively small (3.5-4 V), whereas x_m varies from ~ 0.4 -2.2 nm. Consequently, \bar{v}_{el} can be treated as nearly constant, which adequately explains a constant value of ϵ_{ox} . For a value $\bar{v}_{el} \sim 8 \times 10^7$ cm/sec, based on half of the injection energy, the range of the transit time τ corresponds to an equivalent impulse of $10\omega_{ph}$.

$50\omega_{ph}$, a range that is clearly in the optical response range of SiO₂ ($\epsilon_{ox} \sim 2$). Therefore we conclude that the transit time is not a proper measure for predicting an image force dielectric constant. The fact that the average force ($\propto \omega_{ph}^2 / \bar{v}_{el}^2$) is nearly field independent is further demonstrated in Fig. 5, which depicts the total work and retarded work in the phonon field calculated until the electron approaches its potential maximum z_m . The results reveal i) the average force, given by the retarded work divided by the total distance x_m is nearly the same for both fields; ii) the retarded work is mostly done as the electron is approaching its potential maximum (zero kinetic energy). The latter is understood from the optical phonon scattering rates [10, 14, 19] that are only substantial when the electron energy is comparable with that of the phonon modes (≤ 200 mV) [9]. The latter point is a consequence of the Coulombic nature of electron-optical phonon interaction.

Based on the above discussions, we conclude that the dielectric response depends on the nearly field independent mean velocity of the electron, rather than the transit time. The reason for the different values of ϵ_{ox} obtained from different experimental methods is largely due to the improved sensitivity of BEES to detect the low energy electrons that barely surmount the barrier. For fields beyond the range of the experiment we expect deviations from the observed linearity, a tendency already suggested by the numerical data in Fig. 4.

E. Image force effects on BEEM transmission probabilities

The inclusion of image force effects drastically changes the potential shape at the MO interface region and therefore has pronounced influence on the transmission probabilities. In the presence of the image force potential, the conduction band near the MO interface is strongly bent

down, compared to a triangular barrier (dashed line) in the absence of the image force, as indicated in Fig. 1 (b). Thus the kinetic energy of the injected electrons are quite large. As a point of reference, for $t_{ox} = 75 \text{ \AA}$ and $V_{ox} = 4.4$ and 0.1 V , eq. (1) gives $z_m = 4, 26 \text{ \AA}$, respectively, values that are comparable to the electron mean free paths in SiO_2 [14]. The large kinetic energy within z_m causes a drastic increase in the scattering rates that dramatically lowers the transmission probabilities.

Fig. 6 shows transmission probabilities T_{ox} calculated by Monte Carlo methods and deduced from experimental data for cases with and without image force effects. Details of the Monte Carlo simulation used to calculate T_{ox} have been described in Ref. 10. Here a summary and some added details on the treatment of image force effects are given. The electron transport model used is based on a Monte Carlo integration of the Boltzmann transport equation, which requires a description of the electron motion in the conduction band structure of SiO_2 in the presence of the electric field E_{ox} , as well as a detailed account of the electron scattering processes in the oxide. A single valley conduction band was assumed for the oxide, with an energy dependent effective electron mass $m = 0.5m_0$ at the bottom of the band. At high energies, the electron mass is assumed to revert to the free-electron value m_0 . Electron-phonon scattering was based on semi-empirical scattering rates for both longitudinal-optical (LO) phonon scattering and acoustic phonon scattering [10,19]. Electrons were isotropically injected into the oxide. The transmission probability was determined by tracking energy, momentum and position of the injected electrons until they leave the oxide either at the metal contact or at the silicon substrate. Only the latter contribute to the transmitted current. Back-scattering into the SiO_2 from either contact was neglected. The transmission probability T_{ox} is calculated as $T_{ox} = n_{\text{Si}}/N$, where N is

the number of injected electrons (typically 1000) and n_{Si} is the number of electrons reaching the silicon substrate. The results for a 150 Å oxide and for $V_{ox} = 4.4$ V (triangles and open circles) and 0.1 V (solid circles) are shown in Fig. 6. The inclusion of image force effects in the simulations for 4.4 V drops T_{ox} from near unity to 0.6. Comparing with the experimentally determined T_{ox} for $V_{ox} = 0.1$ V and 4.4 V (solid line and dashed line), we clearly see the necessity of inclusion of image force effects in Monte Carlo simulations. Experimentally T_{ox} is determined by first calculating I_C with equation $I_C = K\tau_{mo}T_{ox}\tau_{os}I_T$ assuming $T_{ox} = 1$, where τ_{mo} and τ_{os} are the kinematic transmission probabilities across the metal-oxide and oxide-silicon interfaces and K is an energy independent constant of order unity. K is used as a fitting parameter and includes the attenuation of the injected current in the metal layer. τ_{mo} can be expressed analytically in a free electron model that is based on the overlap of available conduction band states on either side of the interface, and includes the energy distribution of the electrons injected by the tip, the Fermi function and quantum mechanical transmission probabilities. It varies slowly with energy and exhibit little structure [20]. $\tau_{os} = 1$ for $V_b \geq 0$ V. The curve I_C versus V_T , determined by $I_C = K\tau_{mo}T_{ox}\tau_{os}I_T$, is fitted at the threshold over a narrow (~ 0.2 eV) energy range. The energy dependence of T_{ox} , which is readily determined by dividing the BEEM spectrum (experimental I_C versus V_T) by the calculated one [10], corresponds to the deviation of the calculated curve from the BEEM spectrum.

The cause for the drop in the simulated T_{ox} is acoustic phonon scattering that dominates in the region of $z < z_m$ because of large kinetic energy E_{kin} of electrons. A large fraction of electrons are scattered back into the metal before they reach z_m , drastically decreasing the transmission probability. The agreement between simulation and experimentally determined T_{ox}

is quite good for low V_{ox} , but includes a substantial region of discrepancy within 1 eV of threshold for $V_{ox} = 4.4$ V. The reason for this appears to be related to a field dependency of the quantum mechanical transmission probability [21], which was not included in the simulations thus far.

IV. Conclusions

In conclusions, the paper presents field induced barrier lowering observed with the BEEM technique. Combining experimental observations and theoretical considerations, we demonstrate that inclusion of image force effects has significant influence on barrier heights and electron transport processes. In the following, a further discussion is added about the response of a polarizable medium to a moving charge. The classical model presented in this paper was set up to describe a system governed by quantum effects. Nevertheless the results of an effective image force dielectric constant lying in between the static and the optical are intuitively physical and in agreement with our experimental results. However it should be noted that a quantum mechanical treatment may be required for conditions outside the present experimental range. Provided the velocity of the particle exceeds a certain limit, electrons on the metal surface are not able to follow the time varying field of the moving particle; in effect, the metal/dielectric interface can no longer be treated just by introducing the image of the particle [22-23]. The concept of "transit time" is not valid either. Since the time scale of the moving particle is so short (10^{-15} s), the uncertainty principle no longer allows us to describe the particle with a certain velocity at a certain time. Therefore the classical treatment using trajectories to describe a particle's motion needs to be replaced by quantum mechanic solutions. In addition, the quantum mechanic polaron

cloud surrounding the propagating particle, which modifies the particle's selfenergy, may need to be considered as well. The latter issue appears to be an important consideration for low electric fields, for which the barrier maximum lies deep within the oxide.

We benefited from the technical assistance by M. Prikas. This research was supported by the Office of Naval Research under contract N00014-95-C-0087.

- [1] S.M. Sze, Physics of semiconductor Devices, 2nd ed. (John Wiley & Sons, Inc., New York, 1981)
- [2] Z. A. Weinberg, J. Appl. Phys. **53**, 5052 (1982)
- [3] Z. A. Weinberg and A. Hartstein, Solid State Commun. **20**, 179 (1976)
- [4] S.M. Sze, C.R. Crowell, and D. Kahng, J. Appl. Phys., **35**, 2534 (1964)
- [5] R.J. Powell, J. Appl. Phys. **41**, 2424 (1970)
- [6] P.M. Solomon and D.J. DiMaria, J. Appl. Phys. **52**, (1981)
- [7] E.H. Nicollian and J.R. Brews, MOS Physics and Technology (John Wiley, N.Y., 1982)
- [8] M.V. Fischetti and S.E. Laux, J. Appl. Phys. **78**, 1058 (1995)
- [9] Handbook of Optical Const. of Solids, E.D. Palik, Ed. (Academic Press, Orlando, 1985) p. 753.
- [10] R. Ludeke, A. Bauer, and E. Cartier, Appl. Phys. Lett., **66**, 730 (1995); J. Vac. Sci. Technol., **B 13**, 1830 (1995)
- [11] M. Prietsch, A. Samsavar, and R. Ludeke, Phys. Rev. B **43**, 11850 (1991)
- [12] R. Ludeke, E. Cartier and H.J. Wen, J. Electrochem. Soc., **96-1**, 580 (1996)
- [13] R. Ludeke, H.J. Wen and E. Cartier, J. Vac. Sci. Technol., **B 14**, 2855 (1996)
- [14] E. Cartier, D. Arnold, D.J. DiMaria, M.V. Fischetti, P. Braunlich, S.C. Jones, X.A. Shen, R.T. Casper and P.J. Kelly, Reviews of Solid State Science **5**, 531 (1991)
- [15] C. A. Mead, E.H. Snow and B.E. Deal, Appl. Phys. Lett. **9**, 53 (1966)
- [16] M.V. Fischetti, S.E. Laux and E. Crabbi, J. Appl. Phys. **78**, 1058 (1995)
- [17] Jackson, Classical Electrodynamics, (John Wiley & Sons, Inc., New York, 1962)

- [18] S. Zefar, K. A. Konrad, Q. Liu, E.A. Irene, G. Hames, R. Kuehn and J.J. Wartman, *Appl. Phys. Lett.* **67**, 1031 (1995)
- [19] D. Arnold, E. Cartier and D.J. DiMaria, *Phys. Rev. B* **49**, 10278 (1994)
- [20] R. Ludeke and A. Bauer, *Phys. Rev. Lett.* **71**, 1760 (1993)
- [21] C.P. Crowell and S.M. Sze, *J. Appl. Phys.* **37**, 2683 (1966)
- [22] J. Heinrichs, *Phys. Rev. B* **8**, 1346 (1973)
- [23] G.D. Mahan, in *Collective Properties of Physical Systems*, Nobel Symposium XXIV (B.I. Lundqvist and S. Lundqvist, Editors), Academic Press, New York 1974

Figure Captions:

Fig. 1. (a) Schematic representation of a BEEM experiment on an MOS system, (b) schematic energy band diagram of a charge-free MOS structure under positive oxide bias V_{ox} .

Fig. 2. BEEM spectra (I_C vs V_T) for a 75 Å SiO₂ layer for indicated positive oxide biases taken at $I_T = 2$ nA.

Fig. 3. Observed threshold shifts (solid circles) resulting from fits to the BEEM data of Fig. 2, as well as shifts deduced from classical image force theory (solid lines, corresponding to $\epsilon_{ox} = 2.15, 2.74, 3.90$ respectively). Dotted lines are theoretical results calculated by WKB approximation; the three upmost lines correspond to $\epsilon_{ox} = 2.15, 2.74$, and 3.90; the bottom line was obtained without considering image force effects.

Fig. 4. Field induced barrier lowering obtained by the dielectric response model (eq. 6). The slope of the fit through the numerical results (●) for the case $m = m_0$, corresponds to an effective dielectric constant $\epsilon_{ox} = 2.69$. The two dotted lines represent the optic (2.15) and the static (3.9) limits respectively.

Fig. 5. The total work and retarded work (electron-phonon interaction) obtained by solving eq. 6 for an electron in a model BEEM experiment. Results for a high field (12.7 MV/cm, solid line) and a low field (1.27 MV/cm, dashed line) are presented. Note the retarded work is multiplied by factor -200.

Fig. 6. Transmission probabilities T_{ox} calculated by Monte Carlo methods for $V_{ox} = 4.4$ V/0.1 V with (triangles/solid circles) and without (open circles) image force effects. Solid lines represent transmission probabilities deduced from experimental data.

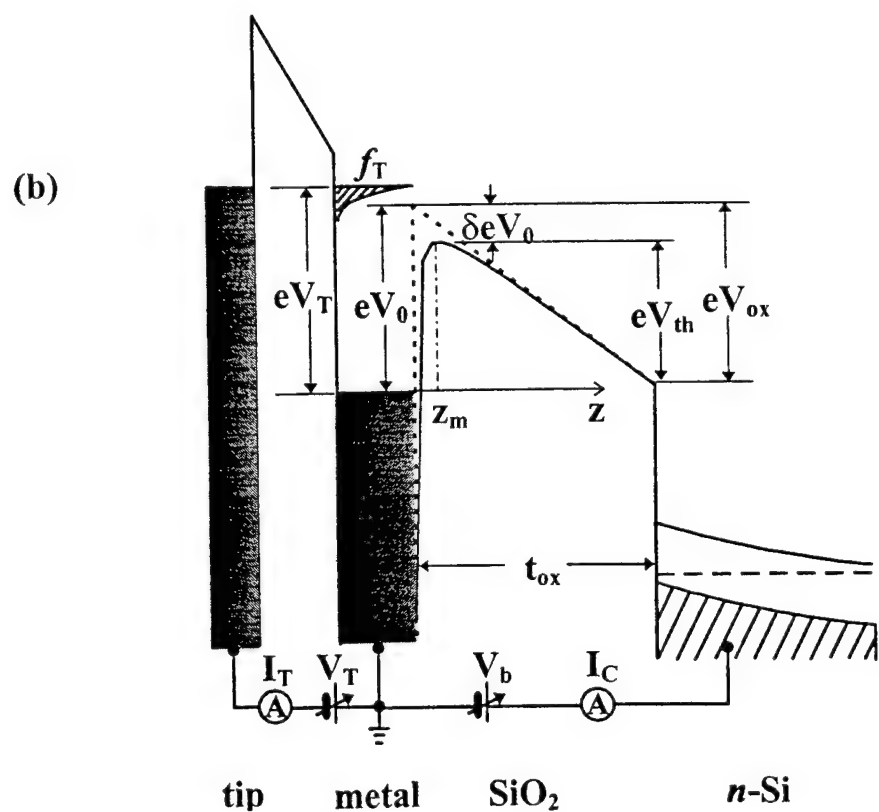
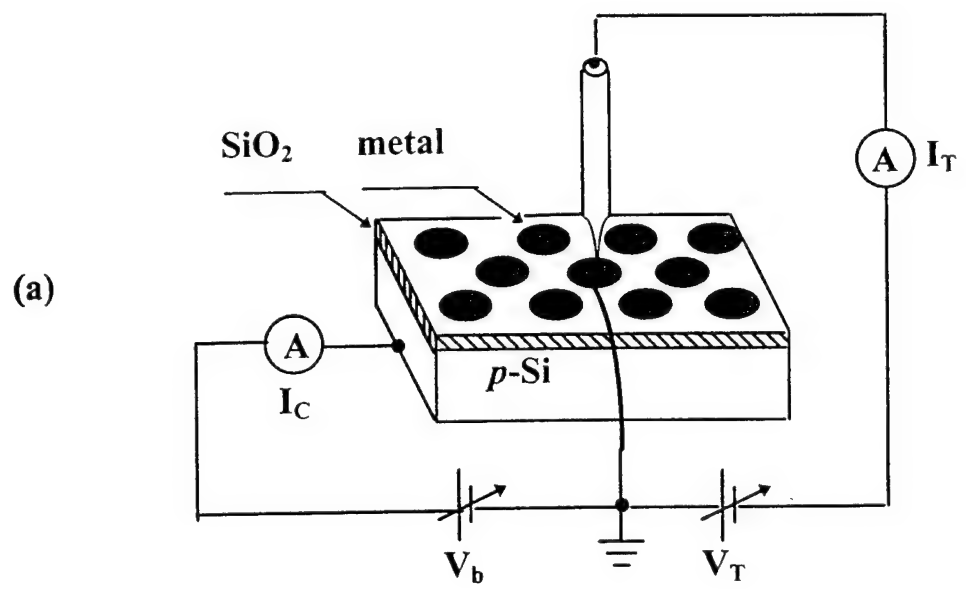


Fig. 1

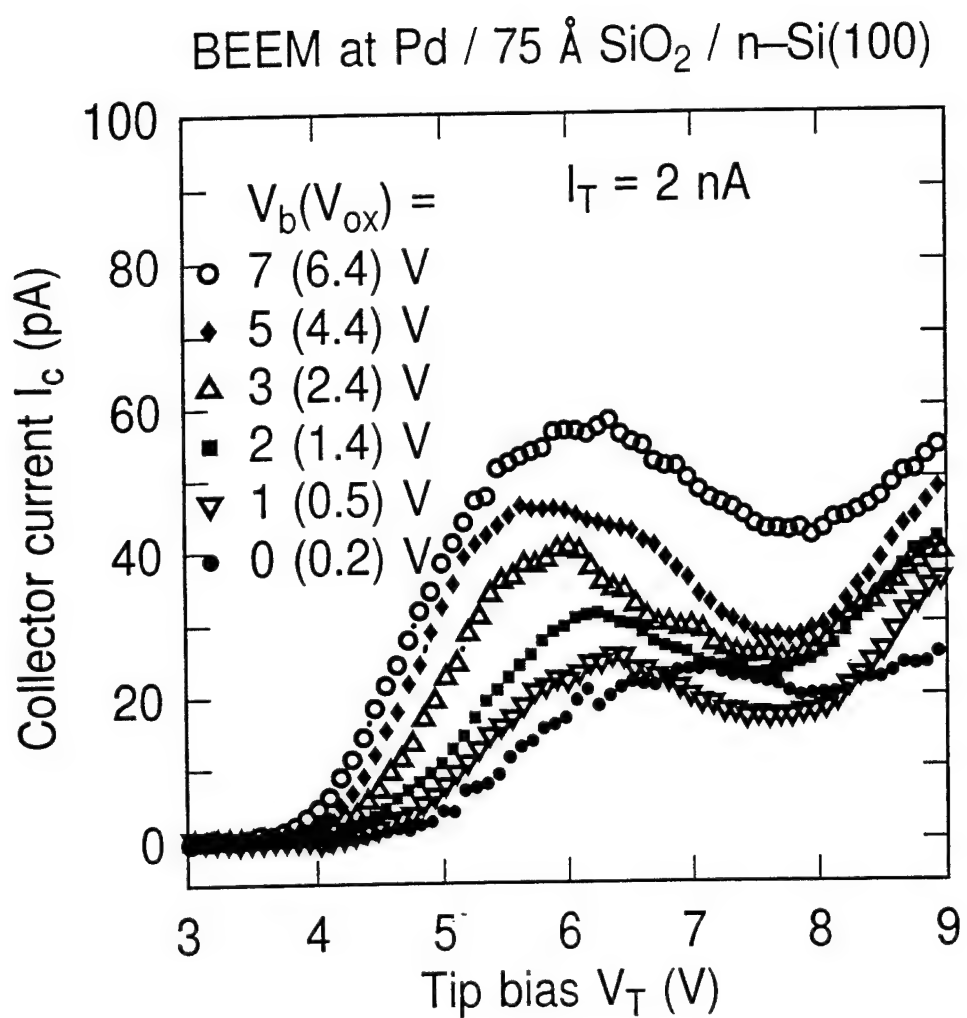


Fig. 2

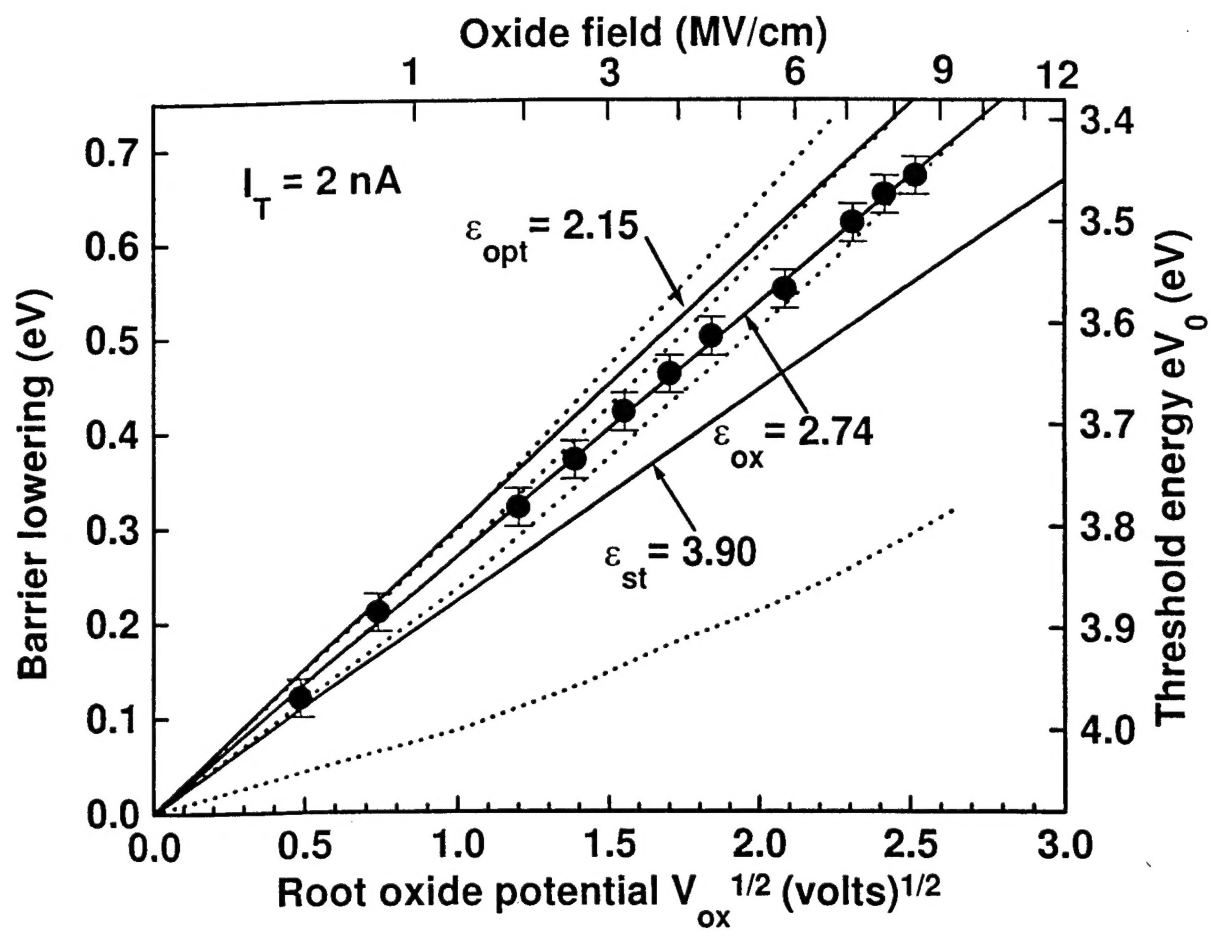


Fig. 3

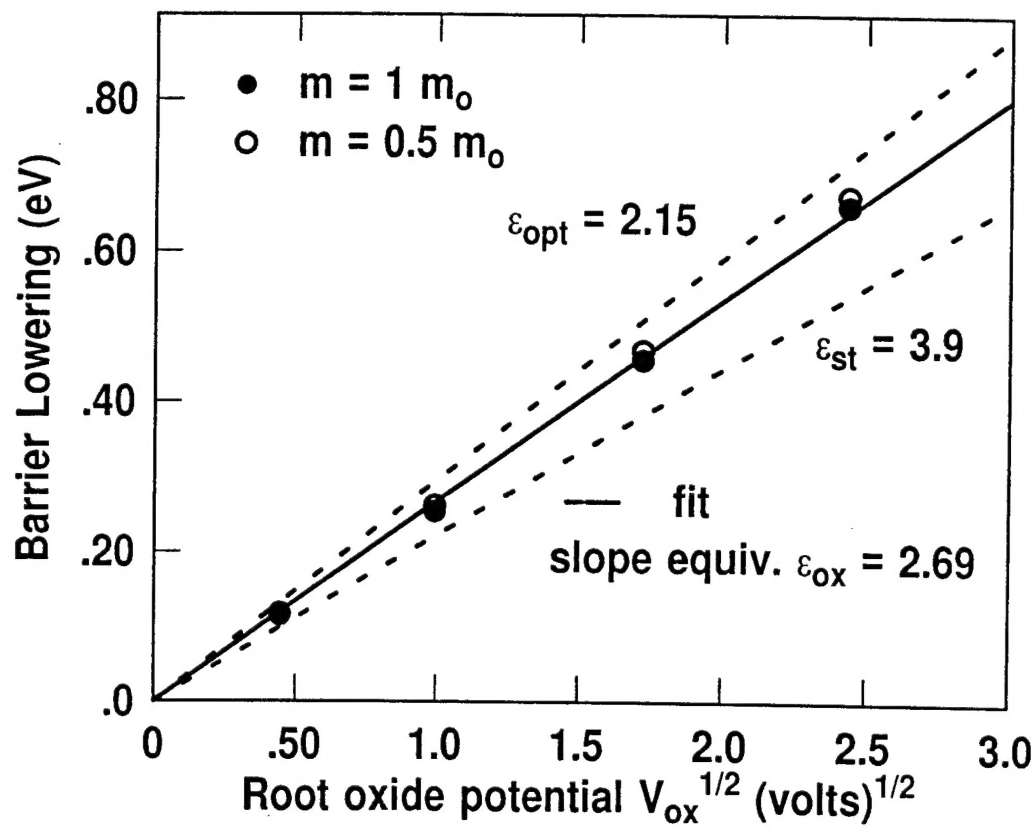


Fig. 4

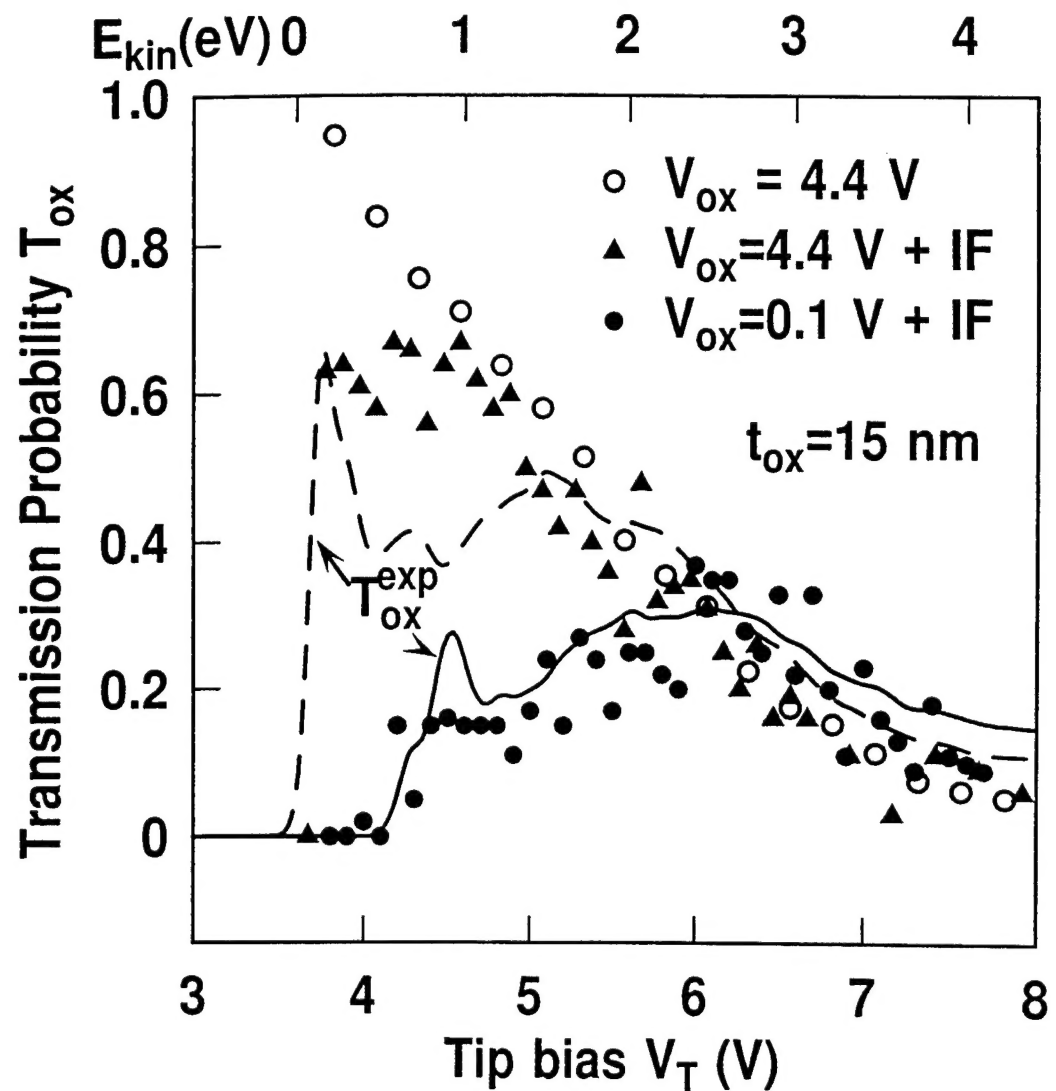


Fig. 6

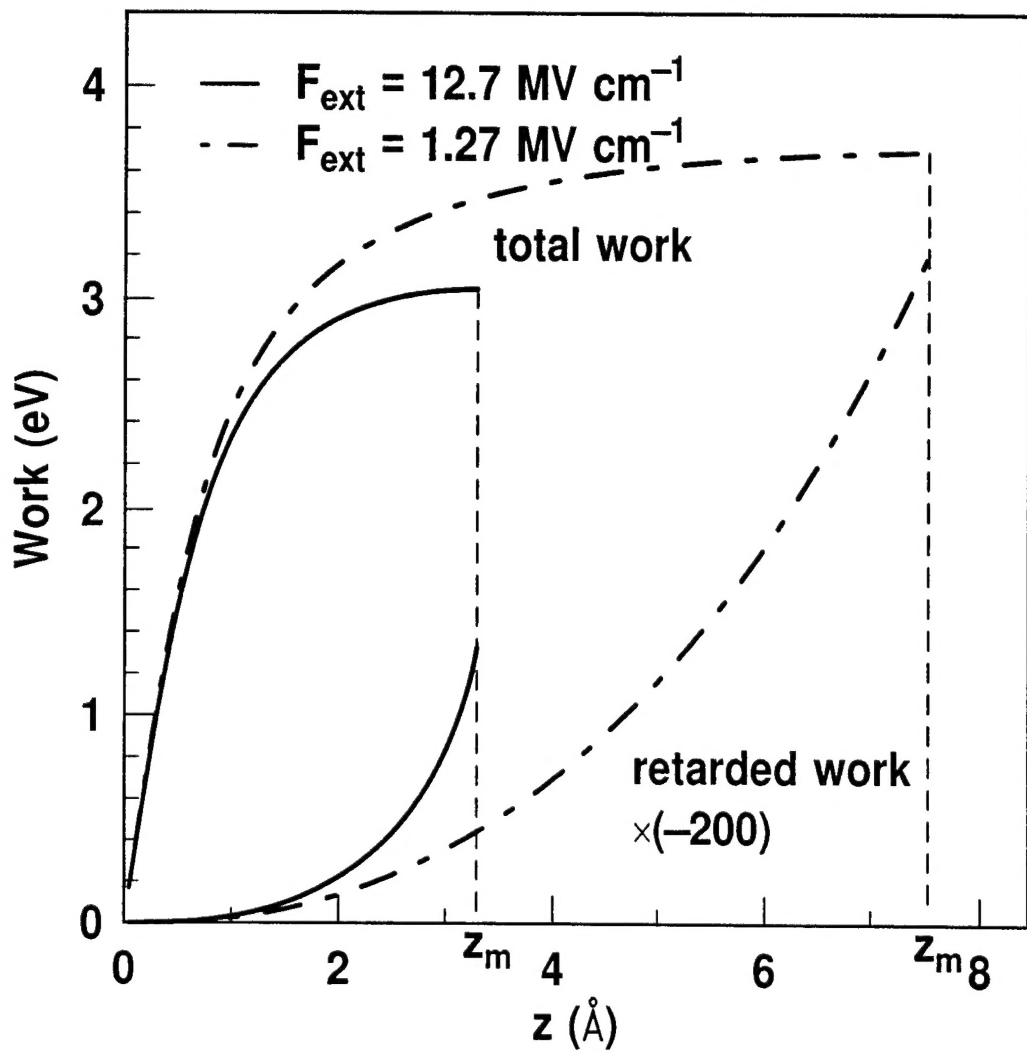


Fig. 7